Journal of Advanced Ceramics
先进陶瓷
ISSN 2226-4108
CN 10-1154/TQ
清华大学出版社 Tsinghua University Press
SciOpen

J Adv Ceram 2026, **15**: 9221358

https://doi.org/10.26599/JAC.2026.9221358

Review

Multiscale synergistic design for enhanced energy storage performance in $Bi_{0.5}Na_{0.5}TiO_3$-based lead-free dielectrics under various electric fields

Pu Mao[1,*], Xinyang Zhao[1], Ruirui Kang[2], Zhilun Lu[3,*], Lixue Zhang[4], Xiaojie Lou[2,*]

[1] *School of Materials Science and Engineering, Jiangxi Key Laboratory of Extreme Manufacturing Technology for High-end Equipment, Nanchang Hangkong University, Nanchang 330603, China*

[2] *Frontier Institute of Science and Technology, and State Key Laboratory for Mechanical Behavior of Materials, Xi'an Jiaotong University, Xi'an 710049, China*

[3] *School of Chemical and Process Engineering, University of Leeds, Leeds LS2 9JT, UK*

[4] *Key Laboratory for Mechanical Behavior of Materials, School of Materials Science and Engineering, Xi'an Jiaotong University, Xi'an 710049, China*

∗Corresponding authors.

E-mail addresses: P. Mao, pumao@nchu.edu.cn, mp_mao_pu@163.com;

Z. Lu, z.lu@leeds.ac.uk;

X. Lou, xlou03@mail.xjtu.edu.cn

Received: April 10, 2026; Revised: August 7, 2026; Accepted: August 10, 2026

Abstract

Dielectric capacitors have been recognized as promising devices for advanced pulse power systems due to their high-power density and fast charge-discharge rates. The dielectrics must simultaneously achieve large energy storage density and high efficiency to support the rapid development of dielectric capacitors. Among the various dielectric ceramics investigated so far, the $Bi_{0.5}Na_{0.5}TiO_3$ (BNT)-based lead-free relaxor ferroelectric has recently become increasingly attractive for dielectric energy storage owing to its high spontaneous polarization and temperature corresponding to the peak of maximum permittivity (T_m) in dielectric constant spectroscopy. Extensive efforts have been devoted to developing high-performance BNT-based ceramics in extreme conditions, and significant progress has been made. To meet the application demands

of energy storage devices across diverse electric fields, it is imperative to understand the fundamental principles of energy storage and devise targeted optimization strategies for BNT-based ceramics. This review provides an overview of energy storage theory and essential determinants governing capacitive performance of dielectric materials, encompassing polarization response, breakdown characteristics, relaxation behavior, and dielectric properties. Furthermore, we elucidate tailored multiscale design strategies to optimize the energy storage capability of BNT-based ceramics across various electric field (*E*-field) regions: low *E*-field (< 300 kV/cm), moderate *E*-field (300 - 500 kV/cm), and high *E*-field (> 500 kV/cm). We further present the developmental progress and future outlook of BNT-based ceramics for advanced electrostatic capacitor applications.

Keywords: Relaxor ferroelectric; Lead-free; Bulk $Bi_{0.5}Na_{0.5}TiO_3$-based ceramics; Energy storage performance; Various electric fields

1 Introduction

Worldwide energy consumption is rapidly increasing, driven by the growing global population and expanding economy. This trend exacerbates the depletion of fossil fuel energy and contributes to environmental pollution. To address escalating global energy demands while safeguarding the planetary ecosystem, accelerating the deployment of sustainable, renewable, and clean energy sources such as wind, geothermal, and hydropower is imperative [1-4]. However, inconvenient storage and low conversion efficiency of renewable energy sources restrict their direct utilization. Under such circumstances, developing advanced energy storage technologies and

electrical energy transition devices becomes increasingly important. Currently, the mainstream of electrical energy storage technologies includes batteries, fuel cells, electrochemical capacitors, and dielectric capacitors [5-8]. A comparison of energy density (W) and power density (P_D) for various energy storage devices is given in **Fig. 1** Distinctly, the battery and fuel cell demonstrate a far higher energy density (~10-10^3 Wh/kg) than electrostatic or dielectric capacitors, but a much smaller power density (~500 W/kg). By comparison, the dielectric capacitor possesses ultrahigh power density (~10^8 W/kg) and ultrafast charge/discharge capability (~100 ns) enabled by dielectric polarization, coupled with superior cycling stability. Consequently, they have garnered significant attention for applications in modern high-power/pulsed-power electronics and advanced energy storage systems.

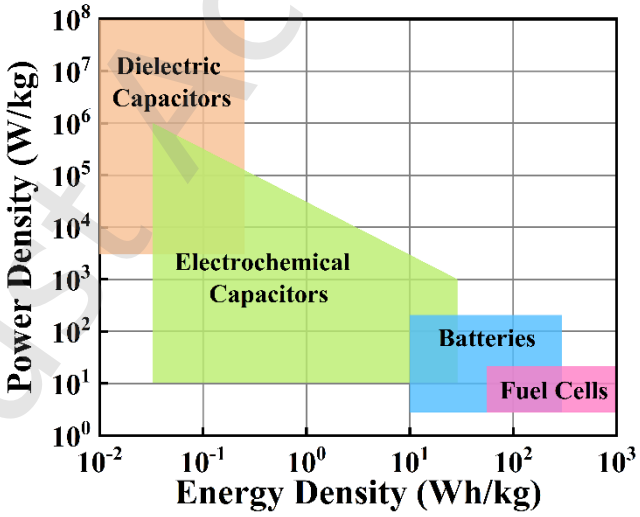

Fig. 1 Comparison of power density and energy density for various energy storage technologies.

As an essential component of advanced pulse power electronic systems, dielectric capacitors manifest brilliant perspectives in diversified application domains under various electric fields (E-fields), as illustrated in **Fig. 2** Specifically, the dielectric

capacitors can be employed in wearable and portable electronic devices that run in the low *E*-field region (< 300 kV/cm), as well as in the avionic and medical industries operating in moderate *E*-field region (300 ~ 500 kV/cm). Furthermore, dielectric capacitors are suitable for high-voltage power transmission systems, ion accelerators, radar systems, and fusion reactors that operate in extremely high-voltage (high *E*-field region) environments (> 500 kV/cm) [9]. As is well known, the applications of dielectric capacitors are not restricted to the abovementioned aspects. However, the broad spectrum of potential applications for dielectric capacitors is significantly constrained by their relatively low energy storage density (10^{-2} ~ 10^{-1} Wh/kg), particularly impeding their practical implementation in miniaturized, lightweight, and integrated devices. Therefore, improving the energy storage density of dielectric capacitor materials is imperative for broadening their application scopes [10-12].

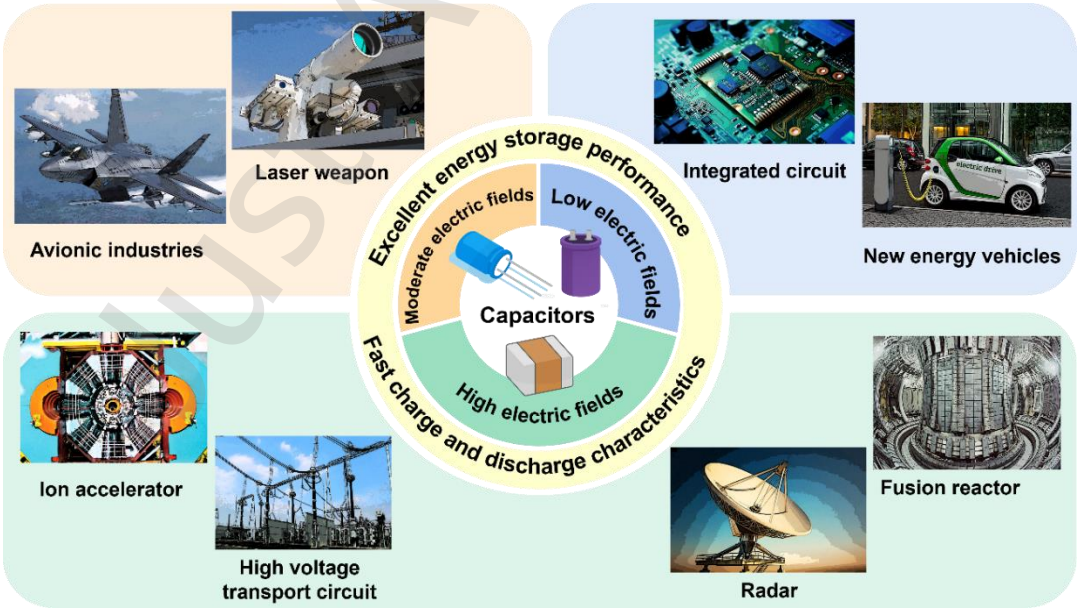

Fig. 2 Schematic diagram of dielectric capacitors with excellent energy storage performance and their diversified applications under various electric fields.

Conventionally, dielectric materials employed in capacitive energy storage

systems have encompassed glasses, polymers, ceramics, and polymer-ceramic composites [13-20]. Among these materials, the pure dielectric polymer exhibits a high dielectric breakdown strength but a low dielectric constant, resulting in a relatively low recoverable energy storage density, and the performance of polymer capacitors deteriorates significantly under high working temperatures (> 120 °C), which hinders their applications in extremely high-temperature conditions [21-23]. In contrast, the dielectric ceramic possesses a high permittivity, a moderate E_b, and good thermal stability. Additionally, the preparation process of dielectric ceramics is relatively simple. These features render dielectric ceramic materials particularly advantageous for high-pulse-power capacitor applications, owing to their exceptional electrical properties [24, 25]. In the field of dielectric capacitors for energy storage, lead (Pb)-based dielectric ceramics such as La-doped Pb(Zr, Ti)O_3 have long been employed in pulsed capacitor applications for their extraordinary power density and efficiency [26]. Nevertheless, related legislation has been established to curtail the use of lead-containing electronic devices, given the pronounced toxicity of Pb, which poses substantial risks to both public health and ecological systems. Consequently, many researchers have made great efforts to develop lead-free dielectric ceramics for environmentally friendly capacitors.

Generally, the lead-free dielectric ceramic materials for energy storage applications can be classified as linear materials (LE), paraelectric materials (PE), normal ferroelectric ceramics (FE), relaxor ferroelectric ceramics (RFE), and anti-ferroelectric ceramics (AFE) according to the relationship between polarizations and applied electric fields, as illustrated in **Fig. 3**(a) LE (such as TiO_2, Al_2O_3, *etc*.) with no

domains [27-29] or no dipoles and PE (such as $SrTiO_3$, $CaTiO_3$, *etc*.) with only dipoles possess a high dielectric breakdown strength (E_b), but their relatively lower dielectric constants result in weak energy storage density, which restricts their further development and applications [30-33]. FE ($BaTiO_3$, $BiFeO_3$) exhibits a high polarization value but a large coercive field (E_c) and a large dielectric loss, deriving from a large amount of energy consumption associated with ferroelectric domain rotation. Consequently, this can directly hinder the improvement of the energy storage performance of FE [34-36]. RFE ($Bi_{0.5}Na_{0.5}TiO_3$-based, $Na_{0.5}K_{0.5}NbO_3$-based, *etc*) possesses typical polar nano regions (PNRs) [6, 8, 37]. PNRs are the nanoscale regions with parallel-oriented polarization dipoles that swiftly respond to the applied electric fields. AFE ($NaNbO_3$, $AgNbO_3$, *etc*.) consists of ordered dipole arrays in which the adjacent dipoles are oriented in antiparallel directions [38]. Among these five types of dielectrics, both RFE and AFE are widely acknowledged as the premier candidates for achieving superior energy storage performance in electrostatic capacitors, primarily due to their near-zero remnant polarization and slender hysteresis profiles. However, the ferroelectric-antiferroelectric phase transition in the AFE can cause high dielectric loss and electric-field-induced strain, resulting in poor energy storage efficiency [39, 40]. On the other hand, RFE exhibits not only a high saturation polarization (P_s) but also a low remnant polarization (P_r), coupled with a favorable breakdown field strength, underscoring its distinct merits in delivering superior energy storage performance [41].

Over the past decades, increasing research efforts have focused on advancing the fundamental understanding and optimizing the energy storage performance of RFE and

AFE for capacitor applications [42-44]. The energy storage performances (recoverable energy storage density and efficiency) under various electric fields for the state-of-the-art lead-free dielectric ceramics are summarized and depicted in **Fig. 3**(b-c). Compared with the $BaTiO_3$ (BT) [45-62], $SrTiO_3$ (ST) [56, 63-75], $CaTiO_3$ (CT) [76-79], $NaNbO_3$(NN) [80-96], $AgNbO_3$(AN) [97-107], $BiFeO_3$ (BF) [108-120], $K_{0.5}Na_{0.5}NbO_3$(KNN) [121-139] based ceramics, the $Bi_{0.5}Na_{0.5}TiO_3$ (BNT)-based relaxor ferroelectric ceramics exhibit extremely significant status regarding the high energy storage density and high efficiency under various electric fields [9, 140-144]. This indicates that the BNT relaxor ferroelectric is a superior and promising candidate for lead-free ceramic capacitors in energy storage applications. Given this, the BNT-based relaxor ferroelectric ceramics have recently garnered numerous research interests for their energy storage application fields in dielectric capacitors.

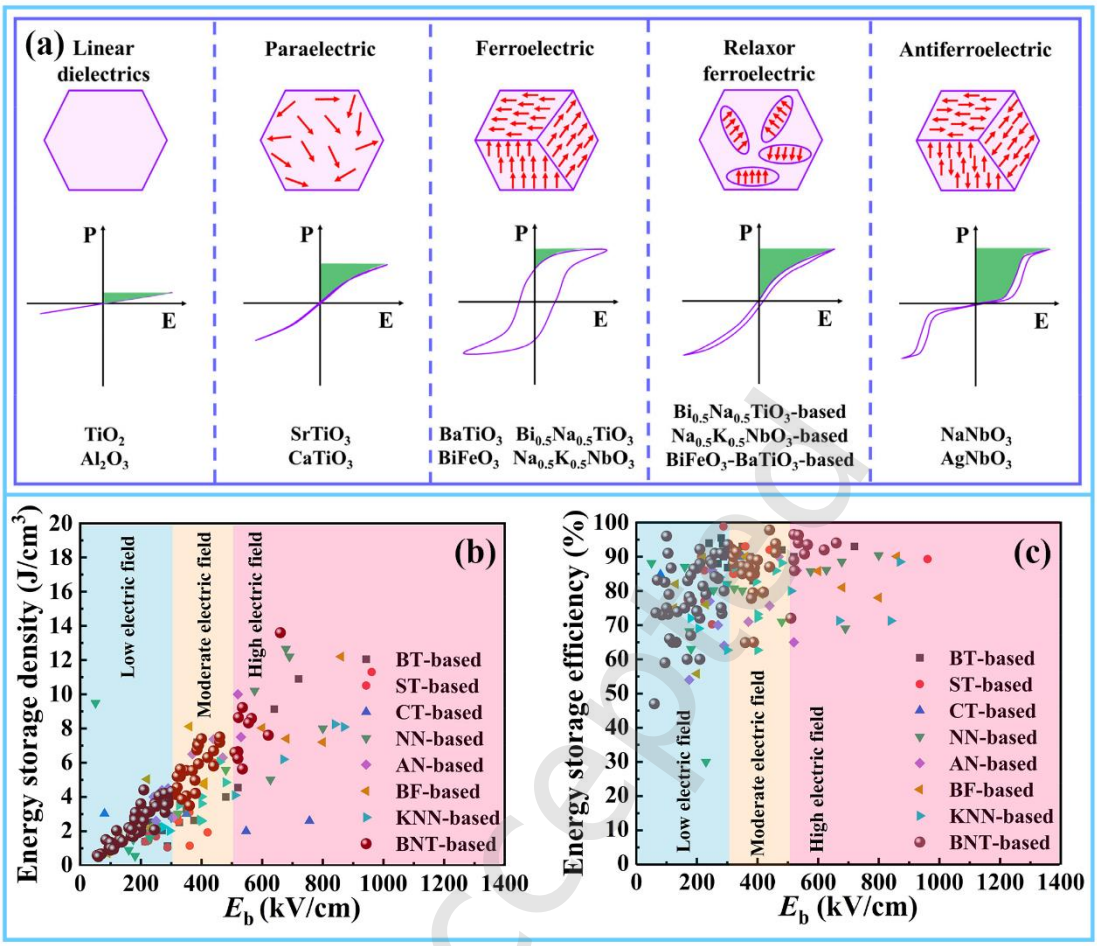

Fig. 3 (a) Schematic illustration of the domain structure and their *P*-*E* hysteresis loops for various typical dielectric ceramic materials. Comparison of energy storage density (b) and energy storage efficiency (c) as a function of electric field for several typical lead-free ferroelectric systems, including BT, ST, CT, NN, AN, BF, KNN, and BNT-based ceramics.

Based on the historical development of lead-free BNT-based relaxor ferroelectric ceramics (**Fig. 4**(a)), the BNT relaxor ferroelectric was first discovered and investigated by Smolenskii *et al.* in 1960 [145]. Subsequently, the BNT-based ceramic was found to be one of the typical relaxor ferroelectric materials with a perovskite structure. It possesses a large P_{max} (~40 μC/cm^2) at room temperature due to the 6s^2 lone pair electron configuration of Bi^{3+}. Furthermore, the BNT-based ceramic shows excellent

temperature stability due to its diffused phase transition behavior and high T_m [146]. Most importantly, the formation of PNRs in BNT-based ceramics assists in getting a small P_r value at high electric fields [147, 148]. Benefiting from these advantages, the BNT-based relaxor ferroelectric ceramics are expected to have an outstanding comprehensive energy storage performance. To illustrate the current research state of the BNT-based lead-free relaxor ferroelectric ceramics in energy storage fields, **Fig. 4** (b) presents a detailed analysis of publication trends and citation metrics from 2012 to 2026 in the Web of Science database. The data were searched and obtained using the keyword combinations "Energy storage", "Dielectric capacitors", "Lead-free ceramics", and "$Bi_{0.5}Na_{0.5}TiO_3$". It is found that the number of publications and citations has substantially increased from 2014 (1, 2) to 2025 (53, 2770). This can fully validate the significant research interest in BNT-based relaxor ferroelectric ceramics for energy storage applications. From these publications, great efforts have been made to improve the energy storage density of BNT-based ceramics. Initially, the energy storage density of BNT-based ceramics typically remains below 3 J/cm^3 in the low E-field region, consistently limiting their practical applications as capacitors [149].

With the rapid development of capacitor devices and the expansion of application demands, dielectric capacitors must cope with diverse conditions across varying electric fields. Accordingly, researchers focus on exploring numerous effective approaches to enhance the energy storage density of BNT-based ceramics under various electric fields. **Fig. 4**(c) illustrates the evolution of energy storage density of BNT-based ceramics at various applied electric fields. As can be seen, the BNT-based ceramics

exhibit a significant improvement in energy storage density at each electric- field stage. In particular, the energy storage density breaks through from about 6 J/cm^3 at a moderate electric field (400 kV/cm) to 24 J/cm^3 at a high electric field (990 kV/cm) [149-153]. Therefore, the BNT-based relaxor ferroelectric ceramics are recognized as among the most promising and competitive environmentally friendly dielectric materials for energy storage applications, garnering significant attention as viable alternatives to lead-based energy storage materials [154-160].

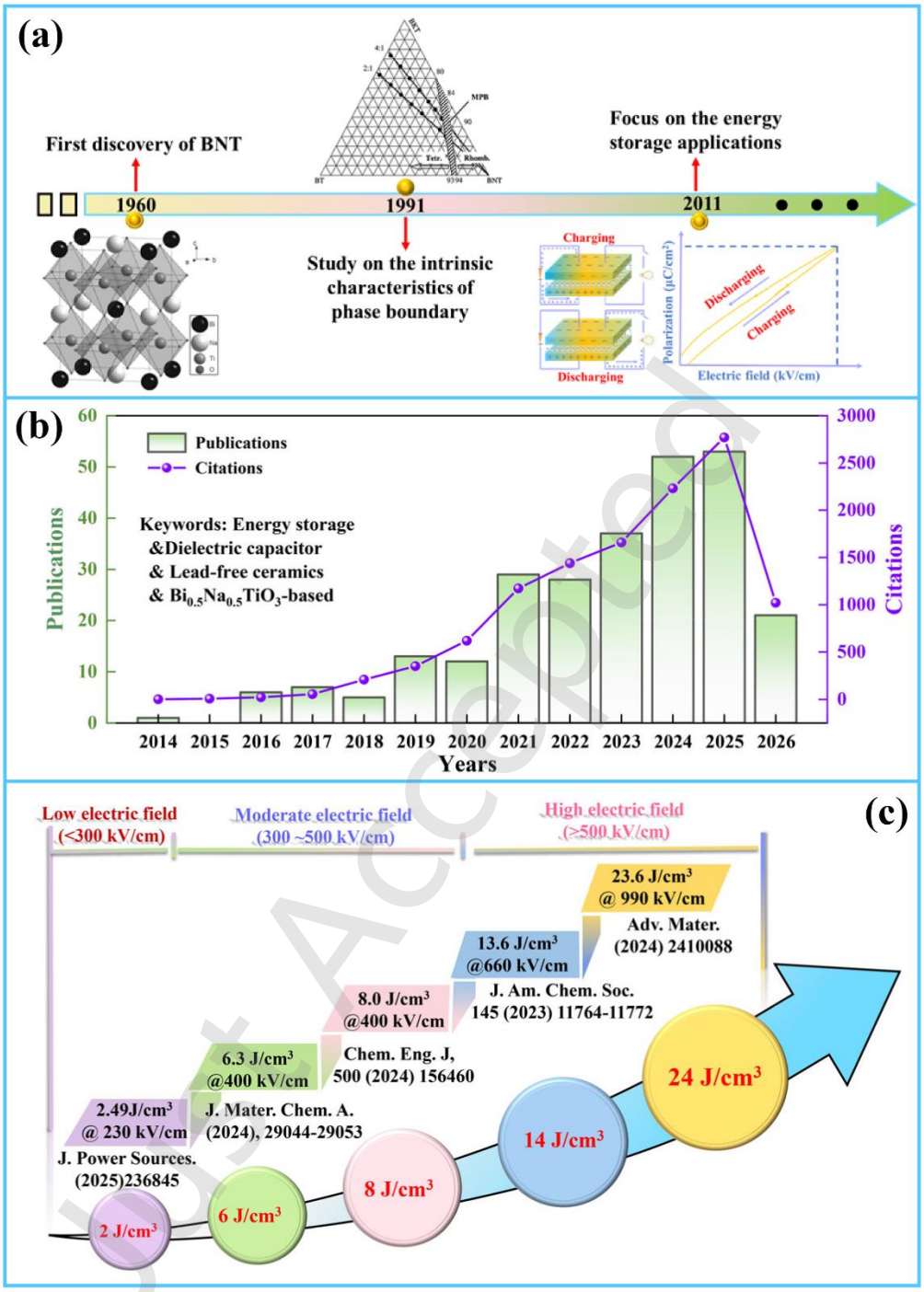

Fig. 4 (a) The development history of BNT-based relaxor ferroelectric ceramics and (b) the number of publications and citations from 2014 to June 2026. (c) The development of energy storage density in BNT-based relaxor ferroelectric ceramics under different electric field conditions [149-153].

In this review, we focus on the summary of the energy storage performance of bulk

BNT-based ceramics under three ranges of electric fields (low electric field, moderate electric field, and high electric field), as well as the modification strategies used to improve the energy storage performance of bulk BNT-based ceramics for various electric field ranges. In view of this, this review is organized into four key sections, as depicted in **Fig. 5**. Initially, we introduce the application backgrounds of dielectric capacitors and present a concise summary of the current development status of BNT-based lead-free ceramics in energy storage devices. Secondly, the fundamental principles of energy storage, including polarization responses, breakdown characteristics, relaxation behaviors, and dielectric properties, are generalized, and the physical nature of the phase structure and domain structure is described. Subsequently, we outline the optimized energy storage performance of BNT-based ceramics subjected to various electric fields and the corresponding optimization strategies governed by the multiscale synergetic effect. Specifically, the regulation of BNT-based ceramic compositions will be achieved through atomic-level lattice distortion induction, nano-level diffuse domain construction, and micro-level grain/grain-boundary characteristic regulation, thereby demonstrating a significant improvement in macroscopic energy storage capabilities. The review concludes by evaluating the challenges and future strategic orientation of BNT-based dielectric ceramics for energy storage applications. We hope this review can provide an in-depth understanding of the correlation among material composition, structures, physical nature, and key parameters of dielectric ceramics, as well as a guideline for designing high-performance dielectric ceramic materials in various electric fields, which further broadens the application fields of

dielectric capacitors and stimulates the exploration of these emerging fields.

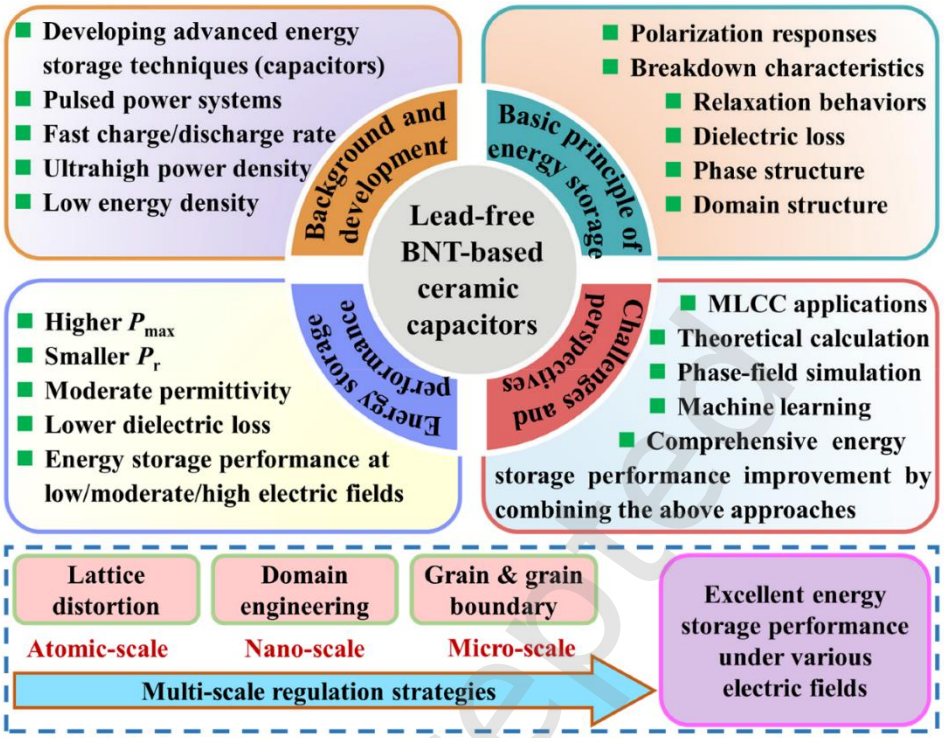

Fig. 5 Outline the frame diagram of this review.

2 Fundamental Principles of Energy Storage and Physical Parameters

A dielectric capacitor consists of two parallel electrode plates separated by a dielectric material, where both dielectric surfaces are coated with conductive electrodes. The energy storage mechanism in such capacitors is fundamentally governed by the polarization phenomena occurring within the dielectric material. This polarization arises primarily from the reorientation of intrinsic electric dipoles in alignment with the applied electric field, as shown in **Fig. 6**(a). Additionally, the stored charge capacity (C) of capacitors can be calculated using the following equation [161]:

$$C = \frac{Q}{V} = \frac{\varepsilon_0 \varepsilon_r A}{d} \tag{1}$$

where Q and V are the stored charge and applied voltage, respectively, ε_0, ε_r represent the vacuum permittivity and dielectric constant of dielectric materials, respectively.

Moreover, a corresponds to the electrode surface area, while *d* indicates the separation distance between the parallel plates. In scientific investigations, the energy density (energy per unit volume) is commonly employed as a key metric for evaluating the energy storage performance of dielectric materials. **Fig. 6**(b) illustrates the Sawyer-Tower circuit, a standard configuration for characterizing polarization-electric field hysteresis loops. The corresponding measured hysteresis loop is presented in **Fig. 6**(c). In the hysteresis loop representation, the yellow shaded region corresponds to the discharge energy storage density (recoverable energy storage density, W_{rec}), whereas the blue region indicates the dielectric energy loss density (W_{loss}). The energy storage characteristics of dielectric ceramic capacitors, including the total energy storage density (W_{total}), W_{rec}, and energy storage efficiency (η), can be quantitatively evaluated using the following Equations [126]:

$$W_{total} = \int_0^{P_{max}} EdP \tag{2}$$

$$W_{rec} = \int_{P_r}^{P_{max}} EdP \tag{3}$$

$$\eta = \frac{W_{rec}}{W_{total}} \times 100\% = \frac{W_{rec}}{W_{rec} + W_{loss}} \times 100\% \tag{4}$$

where P_{max}, $P_{r,}$ and E denote the maximum polarization, remanent polarization, and applied electric field, respectively. According to Equations (2)-(4), it is evident that high P_{max}, low P_r, and substantial E values are crucial parameters for optimizing the energy storage performance of dielectric materials.

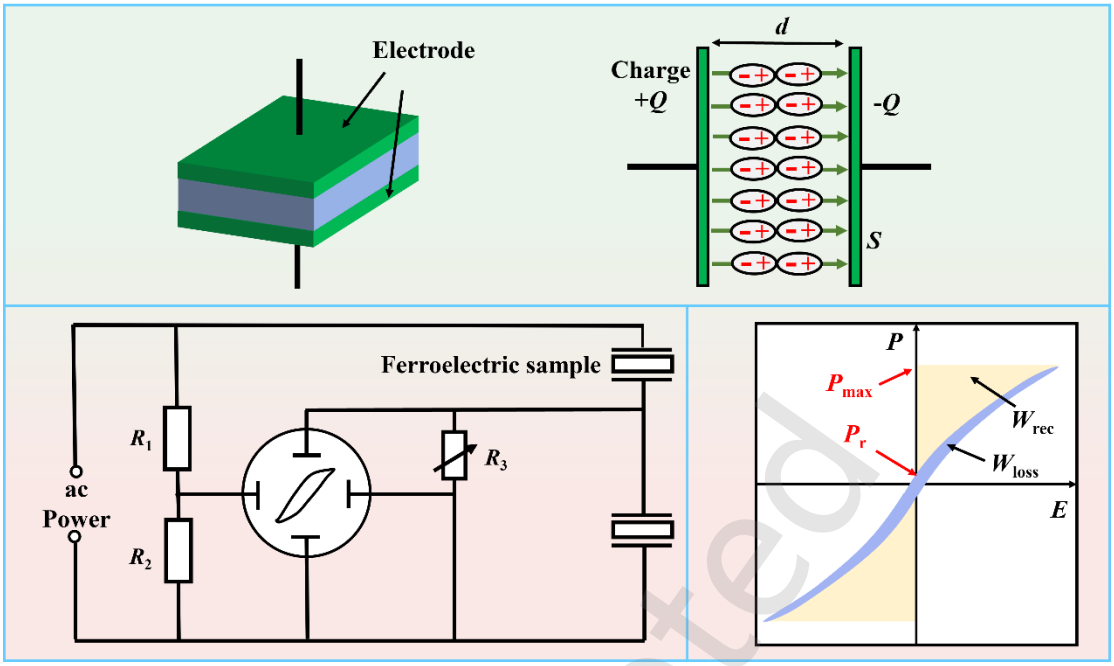

Fig. 6 (a) The capacitor model and the corresponding schematic diagram of the working principle. Reproduced with permission from Ref [24]. Copyright © 2018 WILEY-VCH Verlag. (b) The schematic diagram of the measurement circuit. Reproduced with permission from Ref [162]. Copyright © 2014 The American Ceramic Society. (c) And the *P*-*E* loops of the dielectric capacitors.

2.1 Polarization Response

As for dielectric materials, polarization serves as the fundamental basis for energy storage performance and other electrical properties. Consequently, investigating the polarization response of dielectric materials facilitates the establishment of a clear correlation between microstructure and energy storage performance. Generally, polarization (*P*) is defined as the electric dipole moment per unit volume of dielectric materials. Based on the dielectric polarization mechanism, polarization behavior can be categorized into four distinct types: electronic polarization, ionic polarization, dipole orientation polarization, and interfacial polarization, as depicted in **Fig. 7** [141]. On the

one hand, both electronic and ionic polarization are classified as subcategories of displacement polarization. This type of polarization arises from the slight displacement of electrons, atomic nuclei, and ions when subjected to an external electric field. Furthermore, these polarization mechanisms can rapidly respond to changes in the external electric field. Importantly, they do not contribute to dielectric loss at power and radio frequencies, as their associated dielectric losses primarily occur in the infrared and optical frequency ranges.

In contrast to electron and ion displacement polarization, dipole polarization is classified as relaxation polarization, being significantly influenced by the thermal motion of atoms. Notably, the dipole-oriented polarizability substantially exceeds that of both electronic and ionic polarizability. Consequently, the presence of dipole polarization contributes to the enhanced polarization strength in dielectric materials. As a predominant polarization mechanism, dipolar polarization plays a crucial role in determining the P_{max} and P_r values of dielectric materials. The enhancement of P_{max} can be achieved through two primary approaches: (1) increasing the polarity of A-site ions, which is associated with the hybridization between Bi 6p and O 2p orbitals, and (2) implementing aliovalent substitution with higher polarizability to induce the formation of polarization clusters exhibiting high P_{max} [163-165]. Regarding interfacial polarization, this phenomenon predominantly occurs in heterogeneous dielectric systems and is recognized as a fundamental polarization mechanism in composite dielectric materials under electric fields. The presence of structural imperfections such as grain boundaries, porosity, and secondary phases in practical dielectric materials

facilitates the generation of space charges, with the accumulation of these charges directly correlating with the intensification of interfacial polarization [88, 166-167]. This mechanism significantly impacts the E_b of materials. However, it is important to recognize that the charge carriers accumulated at material interfaces typically require extended periods, ranging from hours to years, to fully dissipate, thereby diminishing the dielectric relaxation properties of the materials. Despite this drawback, interfacial polarization can be strategically employed to enhance the E_b by precisely modulating the activation energy difference between the grain and grain boundary phases [134].

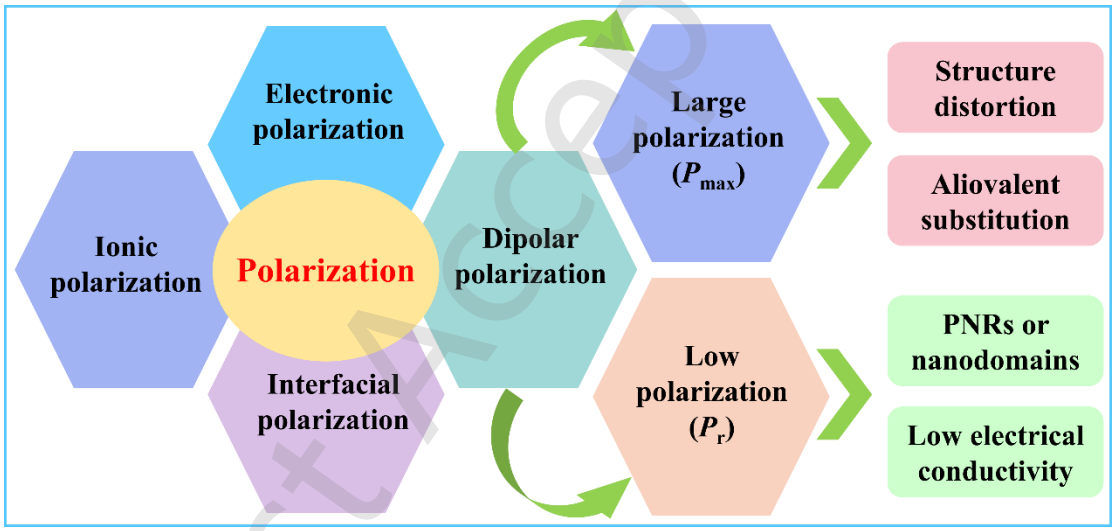

Fig. 7 The polarization type and corresponding influence factors of the dielectric materials.

2.2 Breakdown Characteristics

Based on the above Equations (2)-(4) presented above, it is apparent that the E_b serves as a crucial parameter determining the energy storage performance of capacitors. A comprehensive analysis of the factors influencing breakdown strength provides valuable insights for optimizing the energy storage capabilities of dielectric capacitors. Typically, the dielectric materials may undergo a transition from insulating to

conducting behavior when subjected to a threshold voltage, signifying breakdown at the maximum electric field. This critical parameter, defined as the dielectric breakdown electric field strength, is illustrated in **Fig. 8**.

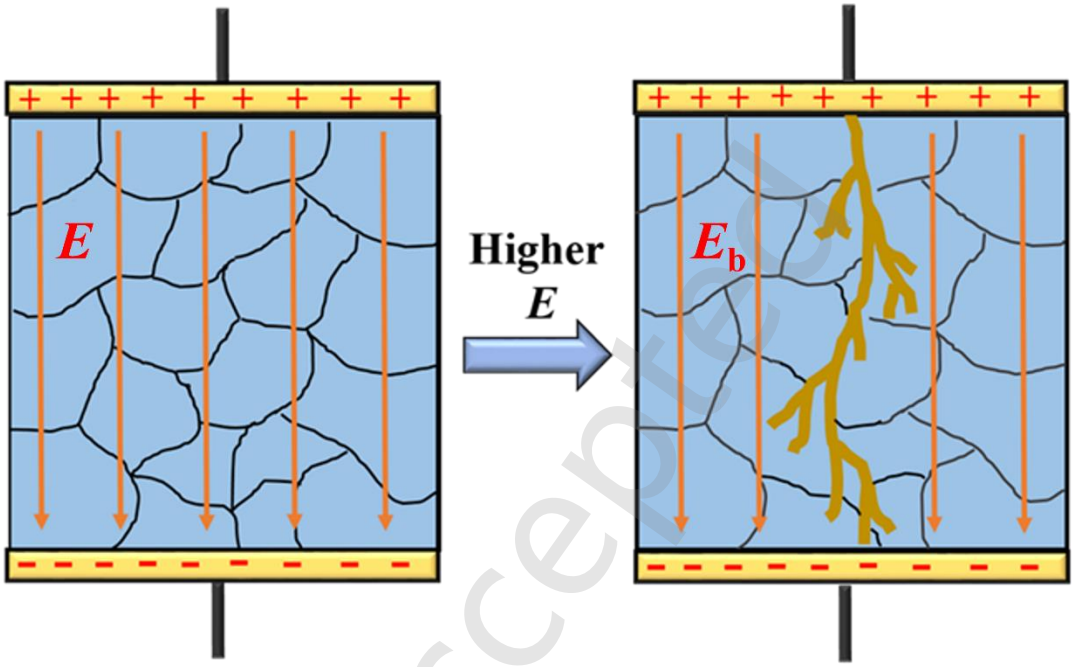

Fig. 8 Schematic diagram of the dielectric breakdown process for dielectric materials.

The Weibull distribution is commonly utilized to characterize the E_b of dielectric materials, as described by the following Equations [168]:

$$X_i = ln(E_i) \tag{5}$$

$$Y_i = ln\left\{-ln\left[-i/(1+n)\right]\right\} \tag{6}$$

where E_i, i, and n represent the accurate value of E_b for each sample, the sequence of the sample, and the total quantity of the sample, respectively. The average E_b value is determined by the intercept of the fitted curve with the X-axis. Furthermore, **Fig. 9** illustrates the fundamental dielectric breakdown mechanisms observed in dielectric materials. The analysis reveals that dielectric breakdown phenomena can be primarily categorized into three distinct types: intrinsic breakdown, thermal breakdown, and

discharge breakdown [169]. In general, the intrinsic breakdown requires extremely high electric fields, making it difficult to activate in practical dielectric materials. Consequently, the breakdown phenomena in dielectric materials are primarily attributed to discharge breakdown and thermal breakdown mechanisms. Thermal breakdown occurs when the local temperature of the dielectric medium rises to a level where its insulating properties are lost, leading to thermal damage. This phenomenon is closely associated with the presence of both conductive and displacement currents in alternating fields, coupled with insufficient heat dissipation. On the other hand, the discharge breakdown results from applying high electric fields to regions with relatively low withstand voltage. Both thermal and discharge breakdown mechanisms are influenced by multiple factors, which can be categorized into two main groups: (1) material characteristics, including grain size, dielectric loss, and grain boundary characteristics, *etc*, and (2) experimental conditions, such as temperature, humidity, and voltage type (DC, AC, or pulse) [170-173]. As mentioned above, extensive research has demonstrated that achieving simultaneously high dielectric constants and high E_b still presents a significant scientific and technological challenge [90, 163-165, 174].

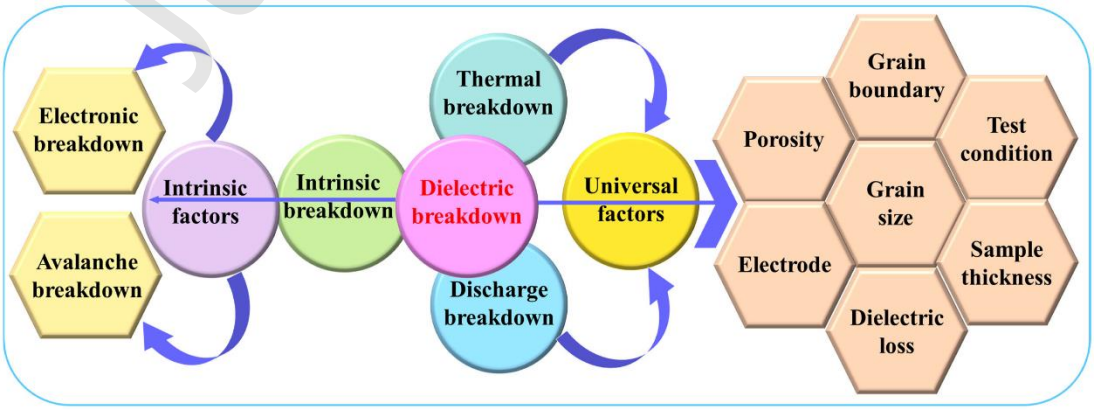

Fig. 9 The dielectric breakdown type and corresponding influence factors of the

dielectric materials.

2.3 Relaxation Behaviors

Upon application of an electric field, the dipoles and electric domains within dielectric materials undergo realignment along the field direction. While a portion of these reoriented dipoles and domains can revert to their initial state upon electric field removal, others remain irreversibly altered. This reversible behavior is quantitatively characterized through relaxation analysis, which serves as a crucial indicator of the material's ability to recover its original state, as demonstrated in **Fig. 10**. The relaxation behavior exhibits a direct correlation with the responsiveness of dipoles and electric domains to external electric fields, where stronger relaxation characteristics correspond to faster response times. Consequently, the enhanced relaxation behavior contributes to the reduction of both E_c and P_r in dielectric materials [108, 175-177]. Furthermore, the relaxation characteristics are intrinsically linked to the specific type and dimensional scale of electric domains, suggesting that the strategic modification of domain structure represents an effective approach for optimizing relaxation behavior in dielectric materials [47, 178-180]. It is well established that an intrinsic correlation exists between relaxation behavior and domain evolution in relaxor ferroelectrics, which critically governs their energy storage efficiency. Notably, grain refinement serves as a critical determinant of domain dimensions within dielectric ceramic systems. [181, 182]. Reducing grain size to submicron or nanoscale dimensions induces a concurrent decline in both maximum and remanent polarization, thereby suppressing long-range macrodomain formation and driving a spontaneous transition to nanodomains. Whereas

macrodomain switching in conventional ferroelectrics incurs severe wall clamping and heavy viscous losses at high frequencies, nanoscale domains minimize domain-wall friction, enabling agile dipole responses with minimal hysteresis. Additionally, the abundant grain boundaries create space-charge depletion layers with high resistivity, which can effectively intercept carrier migration, effectively reducing leakage currents and thermal breakdown risks under high electric fields. Therefore, employing the domain structure engineering simultaneously achieves a slim hysteresis loop and superior E_b of dielectric ceramics [183, 184].

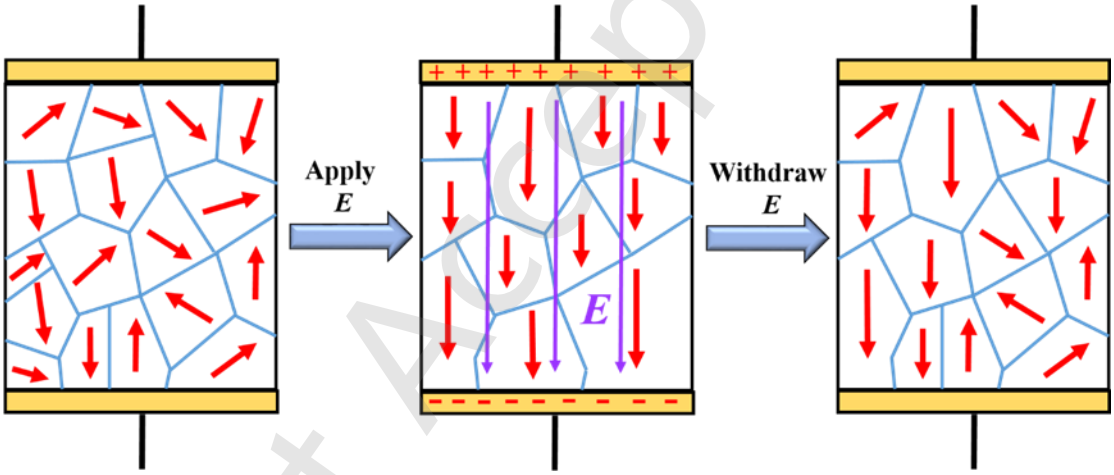

Fig. 10 Schematic diagram of the relaxation process of dielectric materials.

2.4 Dielectric loss

Dielectric materials experience thermal effects resulting from energy dissipation under applied electric fields. This energy dissipation, quantified as power loss per unit time, is characterized by the dielectric loss tangent (tanδ), where the δ represents the phase difference between the applied voltage and resulting current. A higher tanδ value corresponds to greater energy dissipation, consequently inducing temperature elevation in the dielectric material. The origin of dielectric losses can primarily be categorized

into four distinct mechanisms: interfacial polarization, dipolar polarization, defect-induced polarization, and conductive loss [185]. Notably, among these loss mechanisms, polarization loss significantly impacts the energy storage efficiency of dielectric materials [186]. This phenomenon predominantly arises from the substantial phase lag in dipole orientation relative to the applied electric field, as illustrated in **Fig. 11**.

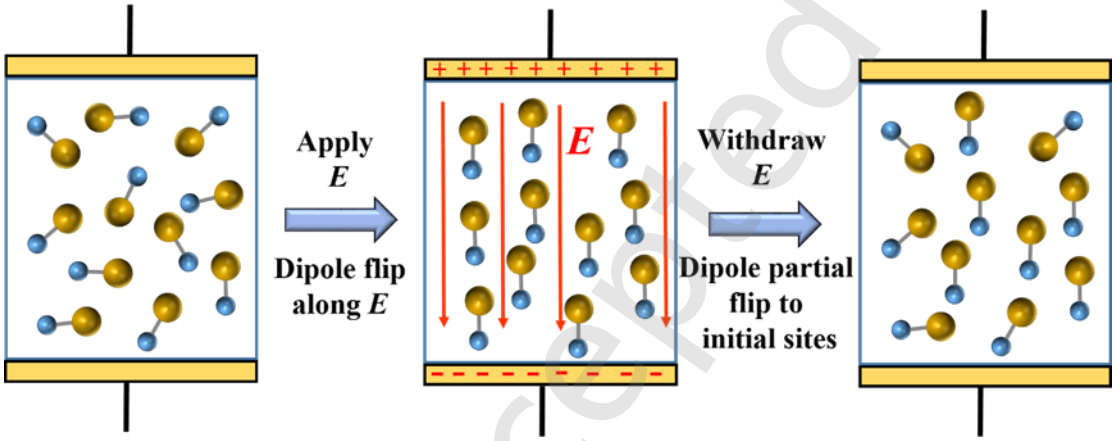

Fig. 11. Schematic diagram of the polarization loss mechanism for dielectric materials.

3 Micro-Structure and Relaxation Behavior of BNT Ceramic

3.1 Phase Structure of BNT Ceramic

In ABO_3-type perovskite structures, A-site cations (characterized by larger ionic radii) preferentially occupy the cube vertices, coordinated with six oxygen anions positioned at the face centers to form an octahedral configuration. In contrast, the relatively smaller B-site cations reside at the center of these oxygen octahedra [187-191], as illustrated in **Fig. 12**(a). From a crystallographic perspective, ABO_3-type compounds exhibit a highly symmetric cubic structure (Pm-3m space group) at elevated temperatures. However, this symmetric configuration undergoes structural transitions to lower-symmetry phases upon cooling, primarily driven by several cooperative phenomena: cation displacements, oxygen octahedral tilting, and distortions, including

off-center shifts of B-site cations within their octahedral coordination environments.

The $Bi_{0.5}Na_{0.5}TiO_3$ (BNT) ceramic crystallizes in the ABO_3-type perovskite structure, where the A-site is co-occupied by Bi^{3+} and Na^{+} cations in an equimolar ratio, and the B-site is exclusively occupied by Ti^{4+} cations, which are centrally coordinated within TiO_6 octahedra [192]. The phase transition behavior of BNT ceramics manifests notable complexity, as illustrated in **Fig. 12**(b-c). Experimental evidence indicates that the BNT adopts a rhombohedral phase below 200 ℃ and transforms into a tetragonal phase above 320 ℃. However, the structural evolution within the intermediate temperature range of 200-320 ℃ remains controversial, with two predominant hypotheses emerging from current research [193]. The first hypothesis proposes the existence of an antiferroelectric phase in this temperature range. Supporting evidence includes the observation of antiferroelectric-like double hysteresis loops by Sakata *et al.*, which is characteristic of antiferroelectric behavior [194,195]. Furthermore, Dorcet *et al.* identified an intermediate antiferroelectric orthorhombic phase using the selected area electron diffraction (SAED) technique, providing structural confirmation for this hypothesis [196, 197]. Conversely, the second hypothesis proposes the coexistence of relaxor rhombohedral and relaxor tetragonal phases within the temperature range of 200 ℃ to 320 ℃ [198, 199]. The aforementioned observation was further corroborated by transmission electron microscopy (TEM) coupled with SAED analyses performed by L.A. Schmitt *et al.*, wherein characteristic superlattice diffraction spots were distinctly resolved at the 1/2(*ooe*) and 1/2(*ooo*) reciprocal lattice positions [200]. These findings have been consistently corroborated by several independent studies [196, 201-

204]. Additionally, the BNT ceramics exhibit a pronounced phase transition from a ferroelectric tetragonal to a paraelectric cubic phase at approximately 520 °C, which corresponds to the Curie temperature (T_c) of the material. Notwithstanding ongoing crystallographic debates concerning the structural assignment of the intermediate temperature regime (200–320 °C) in the BNT system, these phenomena remain physically equivalent within the context of energy storage applications. The disintegration of conventional long-range polar order transitions into short-range polar clusters within the intermediate region [205]. This phenomenon signifies a microstructural fragmentation, thereby leading to the optimized capacitive properties [206]. Unlike conventional ferroelectrics, which exhibit pronounced polarization hysteresis and substantial energy dissipation arising from macrodomain switching, the relaxor state is governed by highly dynamic, PNRs [2]. Confining the domain structures to the nanoscale minimizes the cooperative switching volume and diminishes the energy barrier for domain-wall motion, thereby driving the remanent polarization toward zero upon field removal. Concurrently, the strong hybridization between the Bi^{3+} $6s^2$ lone-pair electrons and O $2p$ orbitals in the BNT matrix sustains a robust maximum polarization under high electric fields. These microscopic attributes yield a slim hysteresis loop with high P_{max} and negligible P_r, establishing an optimal configuration to maximize both recoverable energy density and efficiency [207, 208].

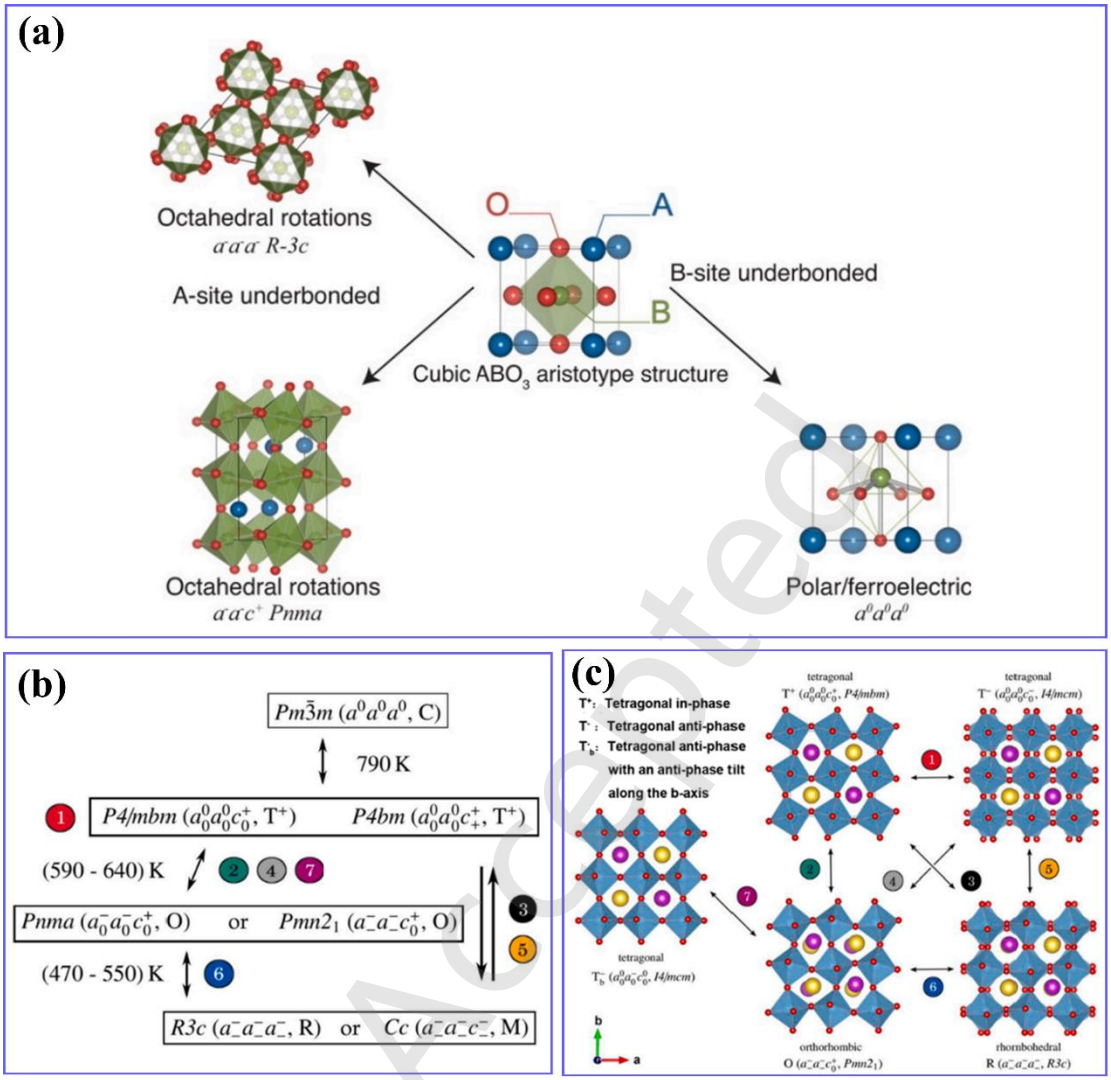

Fig. 12 (a) Cubic perovskite structure and common types of structural distortions. Reproduced with permission from Ref [209]. Copyright © 2013 American Chemical Society. (b) Possible phase transition in BNT and (c) investigated BNT structures with the ordering of A-cations viewed along the direction. Reproduced with permission from Ref [210]. Copyright © 2018 The American Ceramic Society.

3.2 Domain Structure of BNT

The domain structure of dielectric materials presents a fundamental determinant in their electrical properties. Therefore, thoroughly understanding the domain structure helps adopt effective strategies for developing high-performance dielectric materials.

Fig. 13(a) gives schematic illustrations regarding the structured nature of dielectric ceramics at various length scales. As illustrated, these ceramics consist of anisotropic grains whose growth patterns significantly influence material densification processes. From a crystallographic perspective, ferroelectric domains are defined as spatial regions containing uniformly aligned spontaneous polarization (P_s) vectors, separated by transitional interfaces known as domain walls [211]. Moreover, the formation of the ferroelectric domain is a consequence of the lattice arrangement and acts as a bridge connecting the lattice alignment with macro grains. Ferroelectric domains are classified into three types according to their scales: micron-domains (200 nm ~ 5 μm), nano-domains (1 nm ~ 200 nm), and PNRs (1 ~ 10 nm), as shown in **Fig. 13**(b). Particularly, nano-domains and PNRs have been extensively documented to play a crucial role in enhancing the performance of energy storage materials, owing to their rapid switching characteristics compared to micron-domains. On the one hand, the domain structure strongly depends on the phase structure, and the BNT ceramic goes through the Cubic (*C*)→Tetragonal (*T*)→Rhombohedral (*R*) phase transition from high temperature to low temperature [179, 187, 212-215]. Therefore, the phase structure of BNT ceramic will affect its situation in the electric domain. For example, the paraelectric *C* phase of BNT ceramic does not exist in the electric domain. In contrast, the *T* and *R* phases of BNT ceramic possess P_s vectors of 6 and 8, respectively. Moreover, the *R* phase of BNT ceramic typically exhibits 71°, 109°, and 180° domain walls, whereas the *T* phase of BNT ceramic predominantly possesses 90° and 180° domain walls [216]. Although the domain structure of a pure phase is relatively simple, the real domain structure in BNT-

based ceramics is much more complicated due to the interplay of these domains. Therefore, conducting a comprehensive analysis of domain structures is imperative to establish the relationship between structure and electric properties for dielectric ceramics.

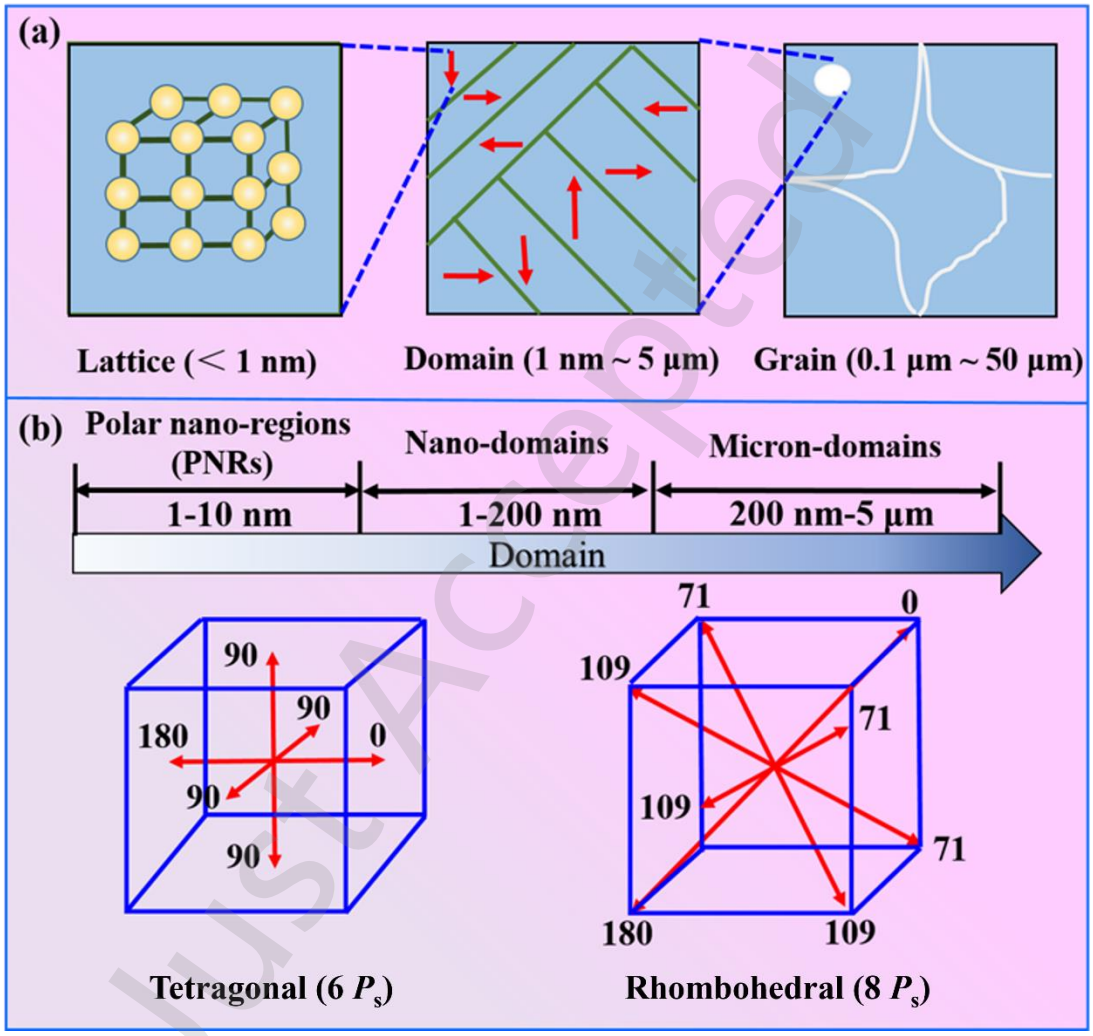

Fig. 13 (a) A schematic diagram illustrating the structural characteristics of dielectric ceramics at different length scales. (b) The domain structure size in BNT ceramics, the corresponding domain walls, and the orientation of polarization vectors.

3.3 Relaxation Behavior of BNT

The relaxation characteristics of the relaxor ferroelectric can be described by the temperature-dependent dielectric spectrum with different frequencies, as illustrated in

Fig. 14(a). The dielectric temperature spectrum can be categorized into three distinct regions based on thermal behavior. Below the dipole freezing temperature (T_f), the material enters the non-ergodic relaxor phase characterized by frozen dipole configurations. Notably, both the long-range ferroelectric domain structure and nano-domains in this phase exhibit distinct responses to external electric fields [147]. These polarized structures undergo reversible reorientation under an applied electric field, while manifesting contrasting relaxation behaviors upon electric field removal. Specifically, while the numerous nano-domains display complete reversibility to their initial configuration, the long-range ferroelectric ordering maintains remarkable stability without detectable structural reorganization. This results in a larger P_r and a square hysteresis loop in relaxor ferroelectrics. Moreover, the region between the freezing temperature (T_f) and the Burns temperature (T_B) is known as the ergodic relaxor state. In this state, the dipole moment between PNRs of the ergodic relaxor state is weakly correlated, and the PNRs are reoriented and rearranged along the applied electric field [217]. Upon removal of the applied electric field, the PNRs spontaneously return to their original state corresponding to the minimum free energy configuration. Additionally, the ergodic relaxor state exhibits a typical frequency-diffuse phenomenon, mainly originating from the coexistence of multiple PNRs. Furthermore, when the temperature exceeds T_B, the relaxor ferroelectrics are in the paraelectric state, and the domain structure disappears. As shown in **Fig. 14**(b), the dielectric spectrum of unpoled BNT presents two anomalous peaks corresponding to the T_{hump} peak and T_m peak, and frequency dispersion can be observed below T_{hump}, but is weak between T_{hump} and T_m

[212, 218]. Meanwhile, the maximum dielectric constant (ε_m) in the vicinity of T_m expresses frequency-independent behavior, analogous to that observed in normal ferroelectrics.

However, the poled BNT is dissimilar to normal ferroelectrics in that its polarization cannot be maintained up to T_m, but only up to T_d, as given in **Fig. 14**(c). The depolarization temperature seems to start at 150 °C and end at 200 °C, and therefore, 200 °C is generally regarded as the depolarization temperature T_d of BNT. The polarization structures of ferroelectric materials exhibit asymmetric evolution pathways under dynamic electric fields due to distinct potential energy barriers across different polarity states [219]. In conventional ferroelectric phases, electrostatic coupling and lattice constraints stabilize the ionic configuration after switching, maintaining high remanent polarization and a square hysteresis loop upon field removal. Conversely, the long-range order fragments into PNRs when the BNT ceramics are chemically tailored into an ergodic relaxor state at room temperature. This transition induces a two-stage polarization mechanism. Under an applied field, the dynamic PNRs overcome local energy barriers to align and merge into the long-range ordered clusters, yielding a high maximum polarization. Upon electric field removal, due to the absence of macrodomain constraints and viscous domain-wall resistance, the aligned dipoles rapidly thermalize and collapse into a macroscopically disordered state under local random fields. Overall, this asymmetric behavior involves forced ordering under an applied electric field and rapid spontaneous relaxation upon electric field withdrawal, suppressing premature polarization saturation and eliminating P_r, explaining the sharp polarization drop at the

depolarization temperature and the resultant narrow hysteresis loop [220].

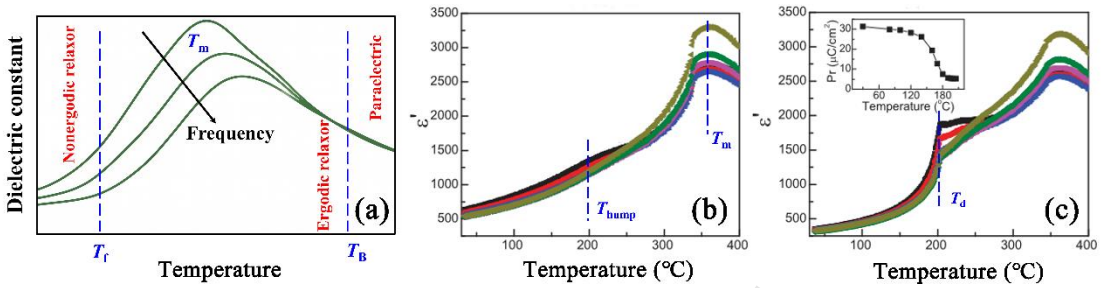

Fig. 14 (a) Temperature-dependent dielectric spectra with the different frequencies of normal relaxor ferroelectrics, (b) unpoled BNT, and (c) poled BNT. Reproduced with permission from Ref [212]. Copyright ©2013 American Physical Society.

4 BNT-based energy storage ceramics applied at various electric fields

As mentioned above, the BNT-based ceramics possess a high P_s originating from the lone pair electrons of Bi^{3+}, which is akin to that of Pb^{2+}, and display a high P_{max} (~38 μC/cm^2) in the *P-E* loops. The high temperature at the dielectric constant peak in dielectric constant spectroscopy (T_m=320 ℃) of BNT-based ceramics ensures high-temperature resistance. These advantages are considered crucial for achieving superior energy storage performance. However, challenges such as high E_c and significant leakage current limit their energy storage capabilities. These issues may be related to the volatilization of Bi and Na during the high-temperature sintering of BNT-based ceramics.

To effectively enhance the energy storage performance of BNT ceramic by taking advantage of its high P_{max} characteristic, in recent years, various strategies such as element doping, multi-phase composition, defect engineering, domain structure, *etc* have been adopted to obtain higher P_{max}, reducing P_r, and then enhancing E_b [222-226].

More importantly, these efforts have been devoted to meeting the application demand of dielectric energy storage capacitors for modern electric devices under various electric fields, including low *E*-field region (<300 kV/cm), moderate *E*-field region (300 ~ 500 kV/cm), and high *E*-field region (>500 kV/cm). The proposed classification of the electric field is strictly established based on the electro-physical boundaries of BNT-based bulk ceramics. In the low *E*-field region (<300 kV/cm), the material exhibits a linear-like dielectric response, where domain switching is largely suppressed. Conversely, the high *E*-field region represents a critical stage where severe leakage current and thermal breakdown typically occur due to the onset of non-Ohmic conduction mechanisms. Operating under high electric fields exceeding 500 kV/cm not only necessitates integrating the transformer system with the dielectric energy storage ceramic but also degrades the overall insulation performance of this system. Therefore, the range of 300~500 kV/cm naturally serves as a critical region for energy storage applications transitioning from low to high electric fields [9].

4.1 Improving Energy Storage Performance under Low *E*-Fields

Integrated electronic circuits and portable devices require operation in the low *E*-field region to protect the dielectric capacitors from damage owing to excessively high voltages. In this case, to facilitate the practical deployment of BNT-based ceramics as dielectric capacitors under low *E*-field conditions, optimizing their polarization response is an essential approach for enhancing the overall energy storage performance [227]. Previous investigations have demonstrated that the polarization characteristics of BNT-based ceramics can be effectively tailored via phase, domain, and defect

engineering [228-230]. This targeted modulation facilitates the attainment of exceptional energy storage capabilities at low electric fields, as summarized in **Fig. 15**.

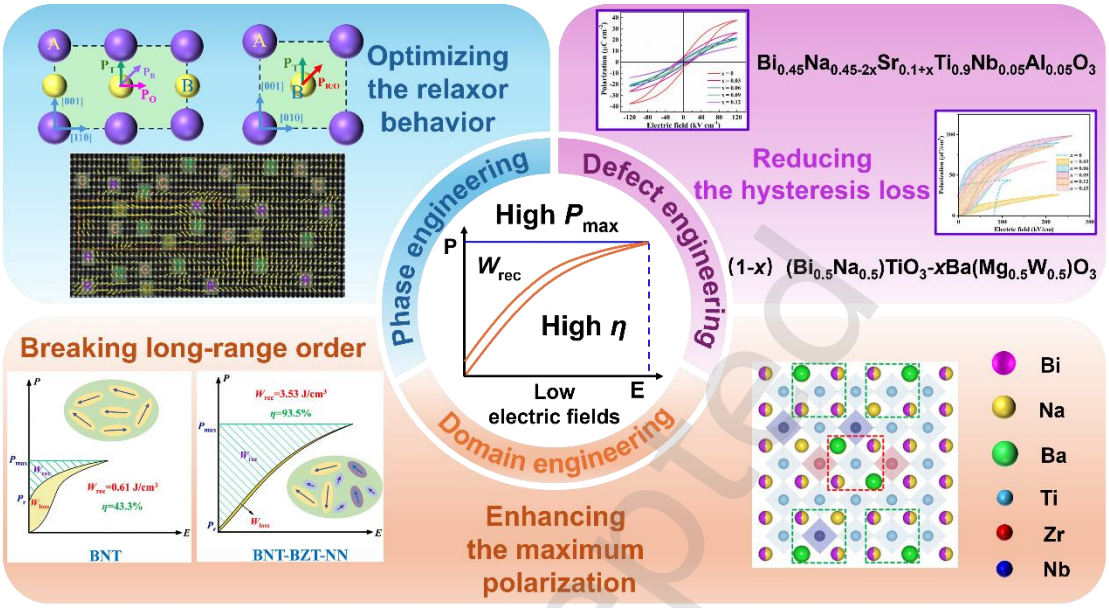

Fig.15 Schematic illustration of the strategies for improving the energy storage performance in BNT-based ceramics under low electric fields [231-234].

Based on these findings, Chen *et al.* introduced the $(Sr_{0.7}Bi_{0.2})(Ti_{0.8}Zr_{0.2})O_3$ (SBTZ) into the BNT matrix, inducing a transition from the rhombohedral phase to the pseudo-cubic phase. Notably, an excellent W_{rec} of 3.05 J/cm^3 was achieved in the 0.7NBT-0.3SBTZ system under 197 kV/cm, as shown in **Fig. 16** [235]. Moreover, the incorporation of $Ca(Nb_{0.5}Al_{0.5})O_3$ (CAN) into the BNT ceramic matrix altered the R/T ratio, resulting in the T phase dominating within the 0.85BNT-0.15CAN ceramic. Consequently, the 0.85BNT-0.15CAN ceramic achieved a relatively high P_{max} of 45 μC/cm^2 and obtained an excellent W_{rec} of 4.41 J/cm^3. The above typical studies strongly confirm that modifying the phase structure is an effective method for adjusting the energy storage performance of BNT-based ceramics. Notably, the adjustment of the high-temperature ergodic relaxor state of BNT-based ceramics to room temperature has

further broadened the temperature range between T_m and T_f. This expansion is primarily attributed to the enhancement of relaxor behavior, which has concurrently improved the stability of the energy storage performance of BNT-based ceramics [148, 236-246]. Furthermore, from the perspective of the morphotropic phase boundary (MPB) to enhance polarization, the energy storage performance of BNT-based ceramics can be substantially improved through the strategic construction of an MPB [202, 247-257]. Ma *et al.* [255] found that the 0.76BNT-0.24ST material not only exhibits a high P_{max} but also maintains a high P_r. However, after introducing the antiferroelectric material $AgNbO_3$, the P_{max} increases to 40.12 μC/cm^2, while the P_r decreases to 3.42 μC/cm^2. Ultimately, a high W_{rec} of 2.26 J/cm^3 is achieved in 0.76BNT-0.24ST-0.05AN ceramic at a breakdown field of 150 kV/mm. This performance improvement can be attributed to significant changes in the crystal structure induced by the addition of $AgNbO_3$, resulting in the formation of an MPB. The distinct splitting of the (002)/(200) diffraction peaks in the samples indicates the coexistence of a rhombohedral ferroelectric phase and a pseudo-cubic paraelectric phase in the BNT-ST-*x*AN relaxor ferroelectric system.

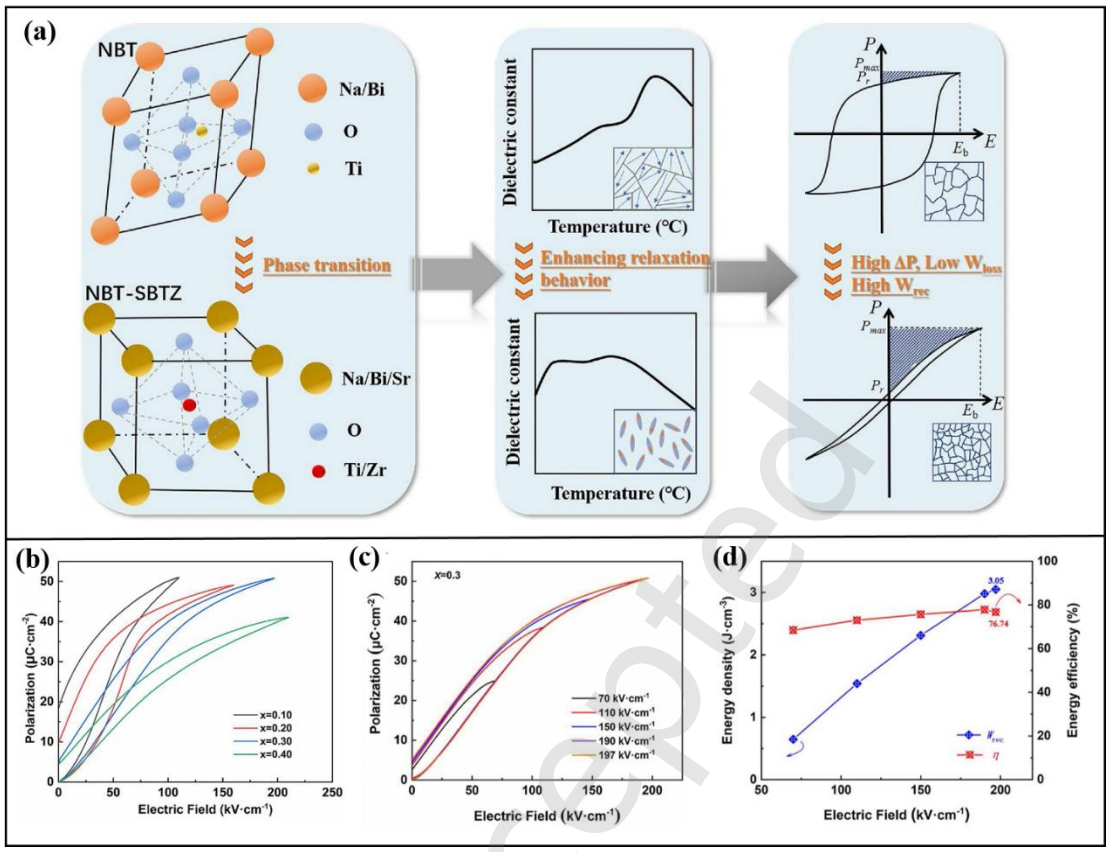

Fig. 16 (a) Path diagram of improving energy storage performance of NBT-based ceramics by introducing SBTZ. (b) The *P*-*E* loops of (1-*x*)NBT-*x*SBTZ (*x*=0.10, 020, 0.30, 0.40) ceramics under critical electric fields. (c) unipolar *P*-*E* loops of 0.70NBT-0.30SBTZ ceramic at different applied electric fields. (d) the energy density and energy efficiency of 0.70NBT-0.30SBTZ ceramic under different electric fields. Reproduced with permission from Ref [235]. Copyright © 2022 Elsevier Ltd.

Additionally, the domain structure can also prominently influence the energy storage performance of dielectric materials because of the strong dependence of the external electric field response on the size of the domain structure [258-260]. Considering this case, Kang *et al.* reasonably employed $Bi(Zn_{2/3}Nb_{1/3})O_3$ as a dopant to develop $(Bi_{0.5}Na_{0.5})_{0.65}(Ba_{0.3}Sr_{0.7})_{0.35}TiO_3$ by domain engineering, contributing to a remarkably enhanced W_{rec} of 2.86 J/cm^3 and an ultra-high η of 90.3% under a low

electric field of 180 kV/cm [228]. Motivated by these findings, Kang *et al*. achieved substantial breakthroughs in energy storage performance through advanced domain engineering in subsequent investigations [167]. Furthermore, Wang *et al.* designed a Sr^{2+}-Sr^{2+} ion pair to replace the Bi^{3+}-Na^{+} ion pair at the A-site of the BNT matrix [261]. This substitution resulted in a break of local symmetry at the A-site due to the increased atomic spacing, which could generate local random fields that prompted the formation of PNRs, as shown in **Fig. 17**(a). As a result, a significant dielectric relaxation characteristic with a relatively low P_r value was obtained in (1-*x*)BNT-*x*$(Sr_{0.7}Bi_{0.2})(Mg_{1/3}Nb_{2/3})O_3$ ceramics. Remarkably, the optimized 0.85BNT-0.15$(Sr_{0.7}Bi_{0.2})(Mg_{1/3}Nb_{2/3})O_3$ ceramic displayed a large ΔP value of 48.7 μC/cm^2 and a relatively high W_{rec} of 3.6 J/cm^3 at a low electric field (200 kV/cm), indicating a great application potential for energy storage devices of advanced pulse power systems, as given in **Fig. 17**(b-e).

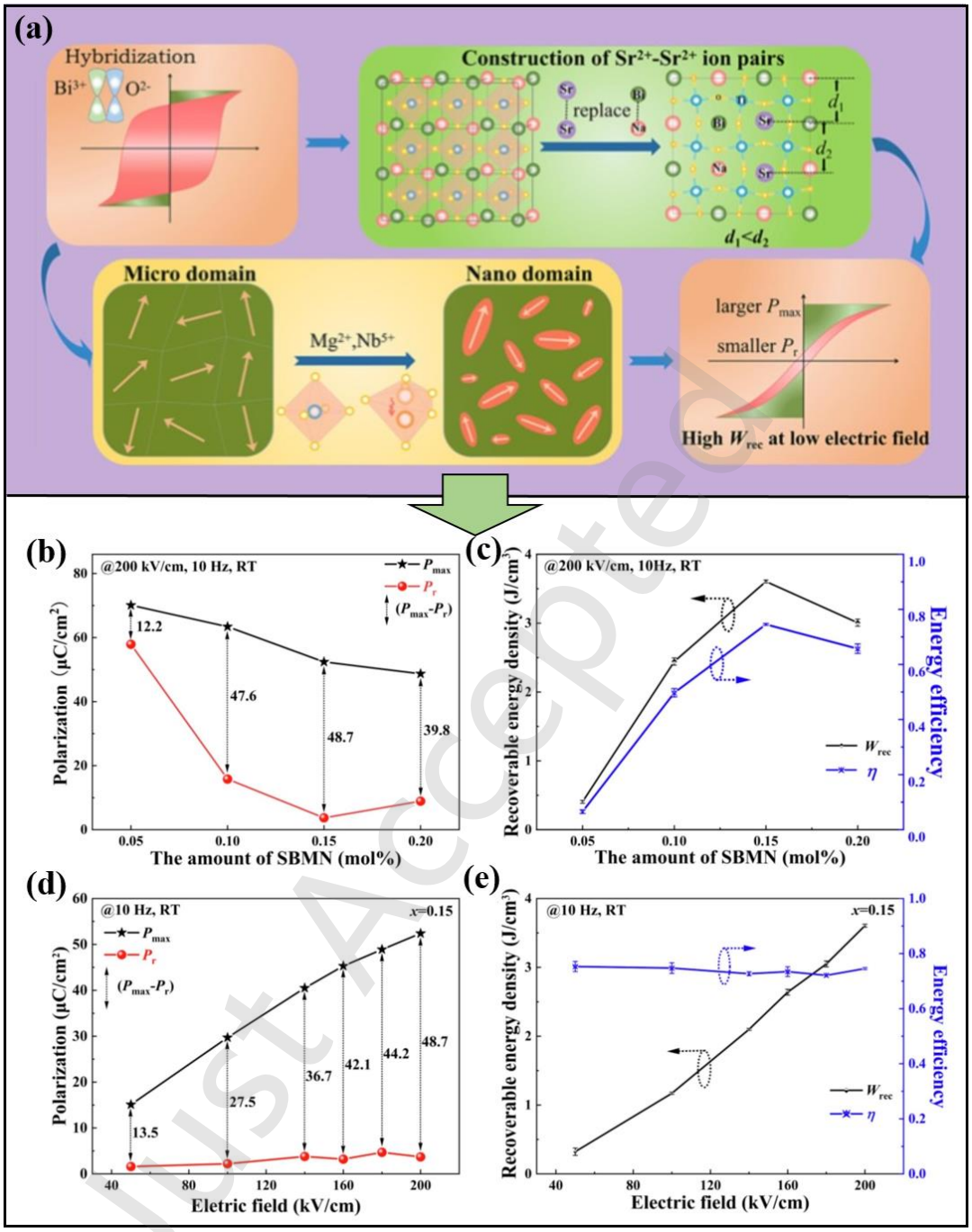

Fig. 17 (a) Schematic diagram of the bidirectional optimization strategy to enhance energy storage characteristics via ion pair construction and domain engineering, (b) comparison of P_{max}. (c) P_r, W_{rec}, and η for different compositions at 200 kV/cm, 10 Hz, RT, variations of P_{max}, P_r (d), and W_{rec}, η (e) for 0.85BNT-0.15SBMN ceramics at different electric fields, 10 Hz, RT. Reproduced with permission from Ref [261]. Copyright © 2023 Elsevier Ltd.

Interestingly, employing a collaborative design strategy regarding the multi-phase structure and multi-domain demonstrates exceptional potential for significantly enhancing the energy storage performance of BNT-based ceramics. Previous work has demonstrated that the incorporation of heterovalent Sr^{2+} ions, coupled with the utilization of $Ag_{0.97}Nd_{0.01}Ta_{0.2}Nb_{0.8}$ (ANTN) as a dopant to substitute the BNT-SBT matrix, could induce the formation of a multi-phase structure [262]. This substitution in the BNT-SBT matrix optimized the *R*/*T* phase proportion and the local random fields in the structure, disrupting the long-range ferroelectric order, as shown in **Fig. 18**. Ultimately, this led to the formation of an optimized *R*/*T* phase ratio and *R*/*T* phase PNRs in the (0.65-*x*)BNT-0.35SBT-*x*ANTN ceramics. The existence of PNRs and the establishment of multi-phase structures were verified by TEM and SAED, respectively, as given in **Fig. 18**(a-c). Additionally, **Fig. 18**(d) displayed the PFM surface topographies, amplitude, and phase images of the *x*=0 and *x*=0.02 ceramics, which also strongly demonstrated the formation of nano-domains or PNRs in the *x*=0.02 ceramic. Moreover, in comparison with conventional ferroelectric domains, the PNRs revealed significantly reduced switching energy barriers and enhanced dynamic characteristics, which collectively facilitated the formation of a slim *P*-*E* hysteresis loop with nearly linear polarization behavior. Meanwhile, the substitution resulted in decreased grain size, increased density, and enhanced temperature stability of this dielectric material. These features led to a progressively slimmer *P*-*E* hysteresis loop in (0.65-*x*)BNT-0.35SBT-*x*ANTN ceramics, as presented in **Fig. 18**(e). It is worth noting that a high ΔP of 47.5 $\mu C/cm^2$ was realized in the *x*=0.02 ceramic sample under a low electric field

(200 kV/cm), resulting in a high W_{rec} of 3.61 J/cm^3 and a good η of 80.6% in the 0.63BNT-0.35SBT-0.02ANTN ceramic under 200 kV/cm, as shown in **Fig. 18**(f-g). Furthermore, A-site cation defect engineering, which disrupts the orderly arrangement of A-site ions, forms different types of defect dipoles and is considered a viable method to enhance the energy storage performance of BNT-based ceramics [216]. Based on the above analysis, to highlight the effect of various optimization strategies on the energy storage properties of BNT-based ceramics, the energy storage performance of the represented BNT-based ceramics under low electric fields is summarized, as shown in **Table 1**.

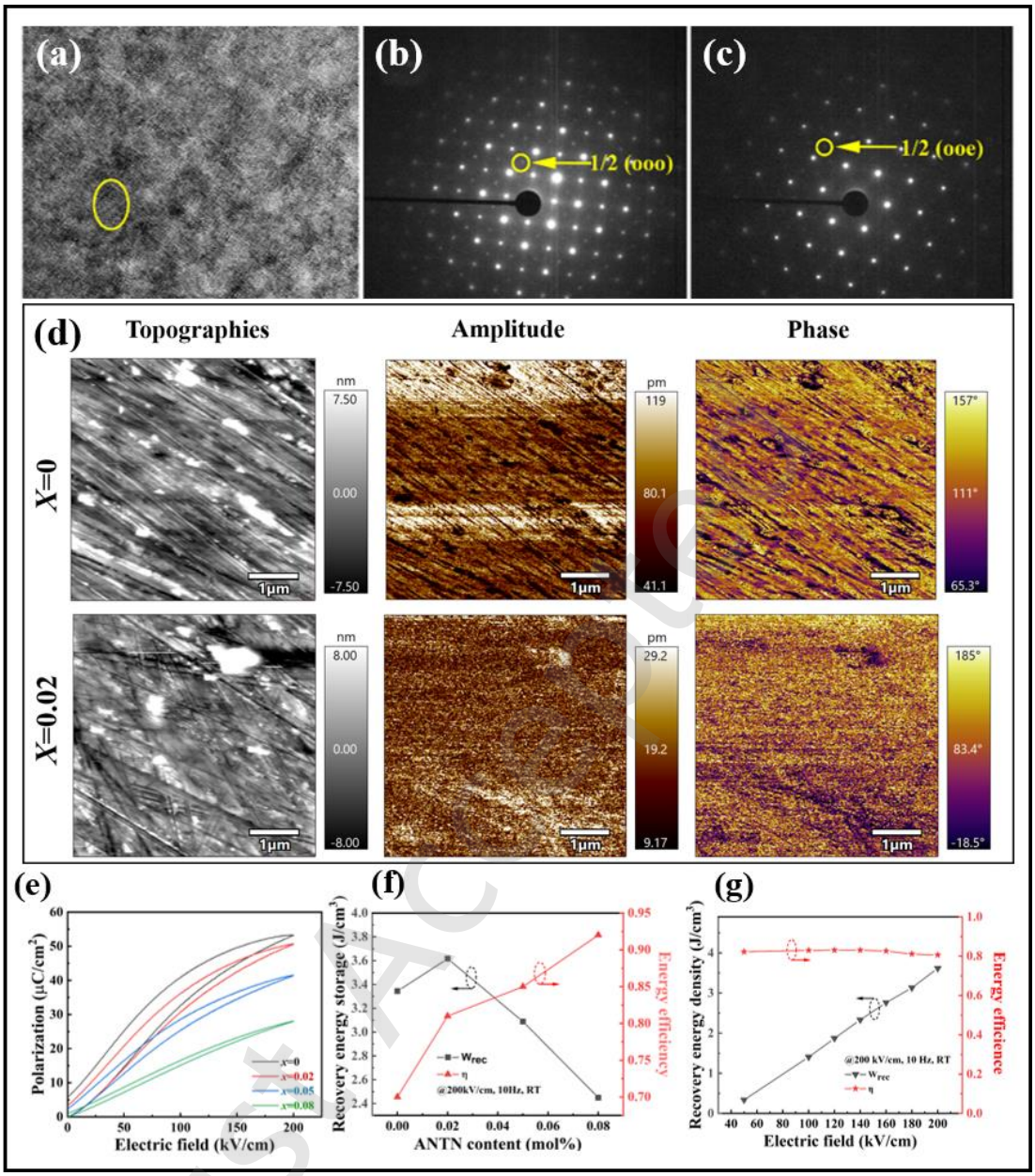

Fig. 18 HR-TEM images. (a) SAED patterns of superlattice reflections along the (b) [111]c and (c) [110]c zone axes of the 0.63BNT-0.35SBT-0.02ANTN ceramic, out-of-plane PFM topographies. (d)The amplitude and phase images of (0.65-*x*) BNT-0.35SBT-*x*ANTN ceramics with *x*=0 and *x*=0.02. (e) The unipolar *P*-*E* loops, (f) W_{rec} and η of (0.65-*x*)BNT-0.35SBT-*x*ANTN ceramic sample at 10 Hz at RT under 200 kV/cm (g) the $W_{rec\ and}$ η of the 0.63BNT-0.35SBT-0.02ANTN ceramic at different electric fields at 10 Hz at RT. Reproduced with permission from Ref [262]. Copyright

As mentioned above, enhancing the energy storage performance of BNT-based ceramics under low *E*-fields is primarily achieved by increasing the maximum polarization to a higher ΔP, especially since the applied voltage is strictly limited. Major optimization tracks include phase boundary engineering, domain texture modulation, and A-site defect design. Among these approaches, the synergistic construction of multi-phase structure configurations demonstrates the most exceptional performance, enabling a remarkable $W_{rec} > 3.6$ J/cm^3 and a high $\eta > 80\%$ at fields below 200 kV/cm [262]. This prominent improvement is driven by the formation of highly dynamic PNRs, which significantly reduce polarization switching energy barriers and delay saturation. Future research should focus on precisely designing local random fields to simultaneously achieve high maximum polarization and low energy loss, thereby driving the practical application of these dielectrics in integrated, low-field pulse power systems.

Table 1 Summary of energy storage performance of BNT-based ceramics under low electric fields.

Ceramics system	E_b (kV·cm^{-1})	P_{max} (μC·cm^{-2})	P_r (μC·cm^{-2})	W_{rec} (J·cm^{-3})	η (%)	Ref.
0.8BNT-0.2$(Bi_{0.5}K_{0.5})(Hf_{0.03}Ti_{0.97})O_3$	60	30	5	0.51	47	[251]
0.7BNT-0.3$SrTiO_3$	65	~37	~6	0.65	73.6	[250]
0.5BNT-0.5$Ba_{0.85}Ca_{0.15}Ti_{0.9}Zr_{0.1}O_3$	70	~22	-	~0.67	83.17	[263]
$[(Bi_{0.5}Na_{0.5})_{0.94}Ba_{0.06}]La_{0.98}Zr_{0.02}TiO_3$	83.4	37.5	-	1.58	-	[248]
0.98$[(Bi_{0.5}Na_{0.4}K_{0.1})]La_{0.02}$-$Ta_{0.025}Ti_{0.975}O_3$	95	37	2.5	1.56	88.5	[249]
0.84BNT-0.16$K_{0.5}Na_{0.5}NbO_3$	100	34	4	1	-	[252]
0.45BNT-0.55$Sr_{0.7}Bi_{0.2}TiO_3$	100	~32.8	~1.6	1.34	96	[264]
$(Ba_{0.3}Sr_{0.7})_{0.5}(Bi_{0.5}Na_{0.5})_{0.5}TiO_3$	100	~32	~2	1.04	77	[265]
0.96$[(Bi_{0.5}Na_{0.5})_{0.94}Ba_{0.06}]$	105	44	4.5	1.66	-	[202]

$La_{0.04}TiO_3$						
$Ba_{0.12}Na_{0.3}Bi_{0.3}Sr_{0.28-1.5x}\square_{0.5x}Sm_xTiO_3$	114	20	-	2.1	91	[266]
0.9BNT-0.1Bi($Mg_{2/3}Nb_{1/3}$)O_3	140	58.8	24.9	1.405	-	[224]
0.55($Bi_{0.5}Na_{0.5}$)TiO_3-0.4($Sr_{0.7}Bi_{0.2}$)TiO_3 - 0.05($Ag_{0.94}La_{0.02}$)($Nb_{0.85}Ta_{0.15}$)O_3	150	55.7	0.8	3.07	82.7	[267]
0.85(0.94BNT-0.06BT)-0.15$BiMg_{2/3}Nb_{1/3}O_3$	170	56	6	3.36	81	[167]
0.85BNT-0.15$Ag_{0.91}Sm_{0.03}NbO_3$	170	~28	~2.5	2.1	83	[268]
0.95(0.6BNT-0.4$Sr_{0.7}Bi_{0.2}TiO_3$)-0.05$AgNbO_3$	180	43.2	5.83	2.35	63	[269]
0.94(0.65BNT-0.35$Sr_{0.85}Bi_{0.15}TiO_3$)-0.06$K_{0.5}Na_{0.5}TiO_3$	180	~39.5	-	2.65	84.6	[270]
0.7BNT-0.3$Sr_{0.7}Nd_{0.2}TiO_3$	182	39.95	-	3.09	77	[271]
0.9BNT-$LiTaO_3$	200	~28	~3	3.1	74.2	[272]
0.85BNT-0.15($Sr_{0.7}Bi_{0.2}$)($Mg_{1/3}Nb_{2/3}$)O_3	200	52.4	3.7	3.6	74	[261]
0.7[0.8BNT-0.2Ba($Zr_{0.3}Ti_{0.7}$)O_3]-0.3Sr0.7$La_{0.2}TiO_3$	210	~31.62	-	2.6	92.2	[88]
0.93BNT-0.07$LaAlO_3$	210	45	-	3.18	60	[273]
0.85BNT-0.15Ca($Nb_{0.5}Al_{0.5}$)O_3	210	~45	~2.6	4.41	88	[91]
0.96(0.65BNT-0.35$Sr_{0.85}Bi_{0.15}TiO_3$)-0.04NN	220	50.46	~3.6	3.08	81.4	[274]
0.7BNT-0.24ST-0.06NN	220	42.1	1.1	3.53	93.5	[233]
0.85[0.7BNT-0.3$Bi_{0.1}Sr_{0.85}TiO_3$]-0.15$KNbO_3$	290	~36.8	~1.18	3.72	90.7	[251]

Notes: Given that factors such as the type of electrode material, the area of electrodes, testing temperature, thickness, and geometry can exert certain influences on the measurement results, and considering the inherent discrepancies in the evaluation of breakdown fields, the data listed in the table are presented for reference and comparison only.

4.2 Improving Energy Storage Performance under Moderate *E*-Fields

For dielectric capacitors operating under moderate electric fields, achieving high energy storage performance critically depends on optimizing the trade-off between polarization strength and E_b. The challenge of simultaneously achieving polarization

enhancement and maintaining a high E_b continues to pose a significant obstacle to improving the energy storage performance of BNT-based ceramics under moderate electric fields. Aiming to the issues of high polarization and low electric fields for the BNT-based ceramics applied under low electric fields, it can synthetically maintain a high polarization by modifying the tolerance factor (t), modulating dielectric constant, and enhancing relaxation behavior, and then, improving the dielectric E_b through optimizing grain size, decreasing oxygen vacancy and broadening band gap, as shown in **Fig. 19**. Benefitting from the optimized key parameters mentioned above, the BNT-based ceramics have the potential to achieve excellent energy storage performances under a moderate electric field. Therefore, summarizing the recently state-of-the-art BNT-based ceramics with brilliant energy storage performance is particularly important, as it will provide an effective route for subsequent corresponding investigations in this field.

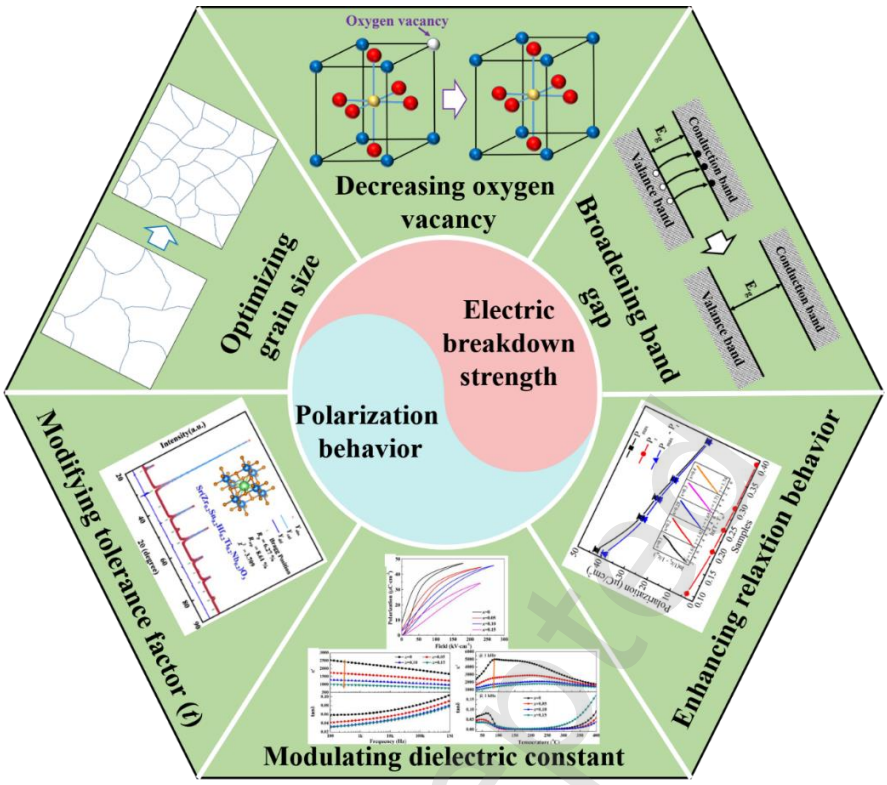

Fig. 19 Schematic illustration of the strategies for enhancing the energy storage performance in BNT-based ceramics under moderate electric fields.

As reported, enhancing the breakdown field strength of BNT-based ceramics typically involves strategies such as reducing oxygen vacancies, minimizing leakage current, decreasing grain size, and increasing the band gap. According to the relationship between the E_b of dielectric materials and grain size (G): $E_b = G^{-a}$, it can be easily seen that the E_b of dielectric ceramic materials exhibits a progressive enhancement as their grain size decreases. Specifically, through combining grain size engineering, Lu *et al.* introduced $Sr(Sc_{0.5}Nb_{0.5})O_3$ (SSN) into the $0.6Bi_{0.5}Na_{0.5}TiO_3$-$0.4Bi_{0.2}Sr_{0.7}TiO_3$ (BNT-BST) ceramic system, and the significant enhancement in E_b was realized by refining the grain size [275]. Furthermore, improvements in the relaxation behavior of the BNT-BST-SSN ceramic system were observed due to the disrupted long-order ferroelectric structure. Meanwhile, the formation of smaller nano-

domains further reduced P_r. As a result, a high W_{rec} of 5.49 J/cm^3 and a high η of 93.6% were simultaneously obtained in the BNT-BST-0.15SSN ceramic under a moderate electric field (455 kV/cm). Considering this situation, a synergistic effect can be achieved by combining grain size engineering with other modification strategies to enhance the energy storage performance of dielectric ceramic materials. Similar results have been demonstrated in other reported works [276-280].

Specifically, the enhancement in E_b of BNT-based ceramics was also effectively confirmed through broadening the band gap. Generally, a large band-gap metal oxide (such as Ta_2O_5) was selected to enhance the E_b of dielectric ceramic materials [99, 281-286]. Deng *et al.* constructed the (1-*x*)BNT-*x*KNN binary solid solution. The results showed that the optimized ceramic of x=0.25 exhibited a slimmer *P*-*E* loop, as illustrated in **Fig. 20**(a-b). Consequently, a W_{rec} of 5.96 J/cm³ and a high η of 80% under a moderate electric field of 400 kV/cm were obtained in this ceramic. Notably, this ceramic also exhibited excellent frequency stability in terms of both energy storage density and efficiency at 400 kV/cm (**Fig. 20**(c)). This phenomenon is primarily ascribed to the pronounced relaxor characteristics and the resultant grain refinement, which collectively broaden the operational window of E_b (**Fig. 20**(d)). As presented in the PFM data of **Fig. 20**(e-f), a voltage of 15 V was applied to a 2×2 μm^2 region. The ceramic with x=0.25 demonstrated superior domain switching capability upon voltage removal, which was attributed to its small domain size and rapid polarization response after the external voltage was withdrawn. As illustrated in **Fig. 20**(g-h), atomic-scale analysis revealed that the gradually enhanced polarization strength and deflection in the

BNT-KNN relaxor ferroelectric led to the formation of PNRs and achieved an enhancement in relaxation behavior [287]. Crucially, critical trade-off analysis of these grain-refinement cases reveals that while abundant resistive grain boundaries effectively increase charge-carrier scattering and intercept breakdown treeing, the excessive volume fraction of grain boundaries introduces severe local lattice strain and domain-wall clamping. Excessive domain wall pinning hinders the movement of domains, preventing the polarization behavior from fully developing under moderate electric fields. Meanwhile, the elevated grain boundary volume also implies a higher content of defects, which raises the leakage current density, reduces the E_b, and increases the dielectric loss. Therefore, tailoring the grain size can improve the dielectric breakdown behavior of dielectric ceramics. Notably, the effect of increased grain boundary content on both polarization and breakdown must be taken into account.

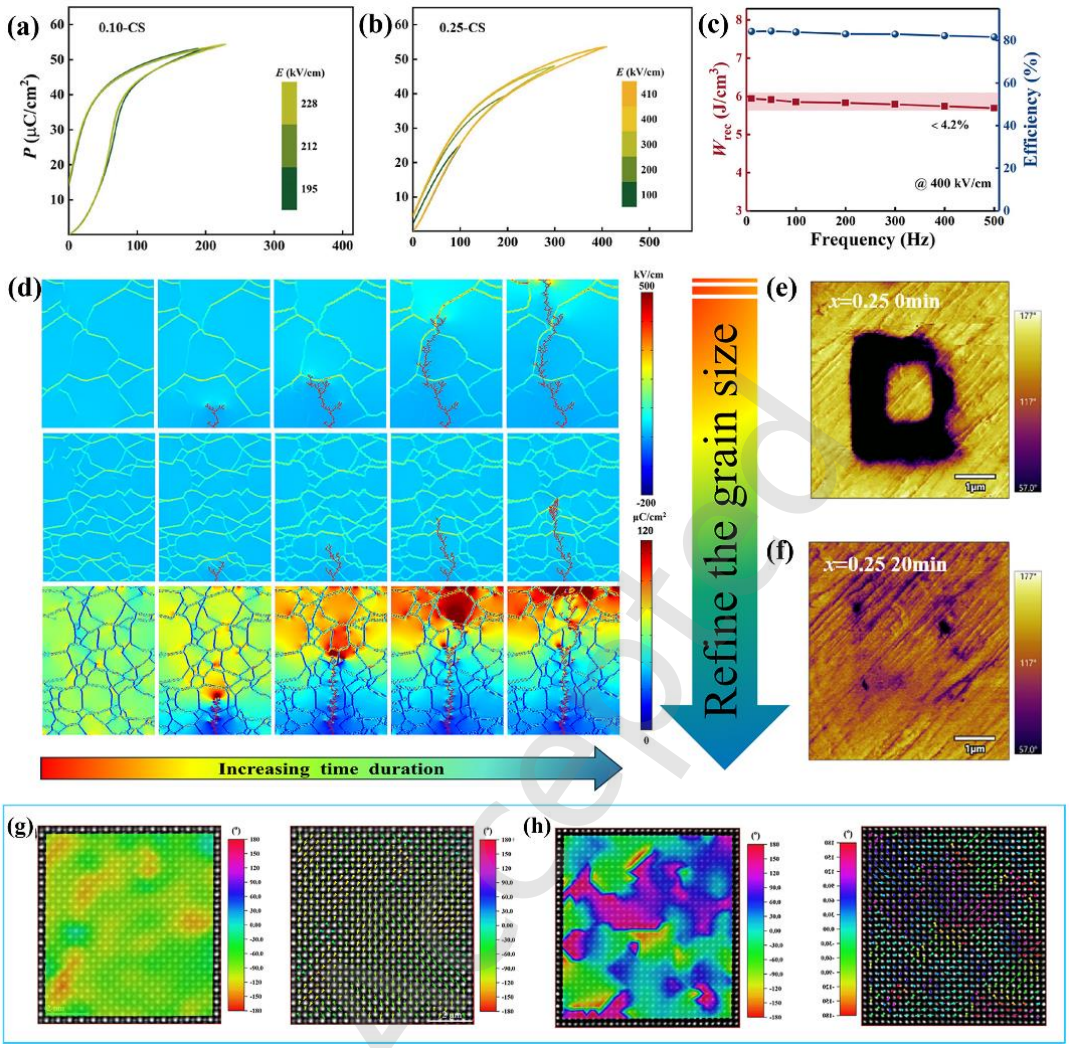

Fig. 20 (a) *P-E* loops of 0.10-KNN ceramic (b) 0.25-KNN ceramic (c) frequency-dependent change of W_{rec} and η at 400kV/cm. (d) Breakdown processes simulation. (e-f) PFM phase pictures and domain reversal in 20 min under 15 V (x=0.25) (g-h) Atomic-resolution HAADF-STEM polarization vector image along [100] direction of 0.10KNN ceramic and 0.25KNN ceramic. Reproduced with permission from Ref [287]. Copyright © 2024 Elsevier Ltd.

For BNT-based ceramics, the formation of oxygen vacancies is inevitable due to the volatilization of Bi or Na elements during the high-temperature sintering process of ceramics. The presence of oxygen vacancies not only elevates the leakage current and

thus reduces resistivity, but also enhances mass transport kinetics, thereby accelerating grain growth. These factors collectively contribute to a reduction in the E_b of dielectric ceramic materials [288-293]. Considering these points, Ning *et al.* proposed an innovative strategy to reduce the oxygen concentration through the synergistic combination of a scheelite-type structure ($SmTaO_4$) and a high-entropy perovskite structure ($(NaBiBaSrCa)_{0.2}TiO_3$) [294]. The doping donor ions (Ta^{5+} and Sm^{3+}) effectively suppress the volatility of constituent elements, thereby mitigating the formation of oxygen vacancies. As anticipated, the NBBSCT-$x$$STO_4$ ceramic with x=0.05 exhibited the lowest leakage current density, which was attributed to the effective suppression of oxygen vacancy formation. Meanwhile, the grain size of this optimized system was reduced by the inhibiting effect of the Ta element on grain growth, resulting in an enhanced E_b of 450 kV/cm. Consequently, the x=0.05 ceramic displayed outstanding energy storage properties with W_{rec} of 5.6 J/cm^3 and a high η of 92.4%. Furthermore, to mitigate the current leakage in BNT-based ceramics caused by the high-temperature volatilization of Bi and Na elements during sintering, additives such as MnO_2, MgO, and ZnO have been demonstrated to be highly effective in reducing the sintering temperature of these ceramics [295-298].

From the phase structure perspective, Koichiro Sakata demonstrated in 1974 that the BNT ceramic possessed an AFE-FE phase transition, as evidenced by the emergence of double *P-E* hysteresis loops at high temperatures [194]. Based on this finding, the BNT ceramic is also recognized as an AFE, which can further enhance its energy storage performance. To modulate the phase structure of AFE BNT ceramic, t can be

identified as an important structural parameter to characterize the stability of the perovskite structure as per the following Equation [299]:

$$t = \frac{R_A + R_O}{\sqrt{2}(R_B + R_O)} \quad (7)$$

where R_A, R_B, and R_O represent the ion radius of the A-site, B-site, and oxygen in the perovskite structure cell, respectively. Generally, the BNT-based ceramics generate a stable FE phase structure when $t > 1$, while the AFE phase structure can be stabilized when $t < 1$. The AFE phase can be further stabilized by decreasing the t value [300, 301]. For example, Nie *et al.* [302] doped the multifunctional $AgNbO_3$ (AN) (t=0.93) into the $0.55Bi_{0.5}Na_{0.5}TiO_3$-$0.45Sr_{0.7}Nd_{0.2}TiO_3$ (BNT-SNT) system. Eventually, a high W_{rec} of 3.08 J/cm^3 and a mid η of 79.94% were achieved in the x=0.5 ceramic under 330 kV/cm. Jiang *et al.* incorporated $NaNbO_3$ (NN) with t=0.97 into the 0.95BNT-$0.05SrZrO_3$ (BNT-SZ) system to postpone the AFE-FE phase transition field, and the best comprehensive energy storage performance (W_{rec}=3.78J/cm^3, η=86%) was achieved in the 0.5(BNT-SZ)-0.5NN ceramic under 320 kV/cm [303].

Besides, nearly linear hysteresis loops can be obtained by adjusting the dielectric constant and delaying the polarization saturation to higher electric fields for the BNT-based ceramics. Therefore, paraelectric phase materials possess a considerable E_b at room temperature and a near-zero P_r, which are used to adjust the properties of most ferroelectrics, especially the energy storage properties [304-308]. According to the work reported by Shi *et al.*, incorporating $SrTiO_3$ (ST) and $Bi(Mg_{2/3}Nb_{1/3})O_3$ (BMN) into the BNT matrix resulted in the formation of a solid solution. The substitution of Sr^{2+} at the A-site not only reduced the dielectric constant (ε_r) (**Fig. 21**(a-b)), but also

introduced A-site disorder and disrupted the long-range ferroelectric order. As illustrated in **Fig. 21**(c-d), the High-resolution TEM revealed the presence of PNRs (<5 nm), with random orientations, which contributed to the reduced dielectric losses. Additionally, the ST-BMN doping could increase the grain boundary activation energy (E_g increases from 0.90 eV to 1.21 eV), thereby inhibiting carrier migration and enhancing the E_b, as demonstrated in **Fig. 21**(g). Ultimately, through these synergistic effects, it was observed in **Fig. 21**(f) that the 0.5BNKT-0.5(2/3ST-1/3BMN) ceramic achieved a high energy storage density of W_{rec}=7.19 J/cm^3 and an ultra-high η of 93.8% under a moderate electric field of 460 kV/cm [9].

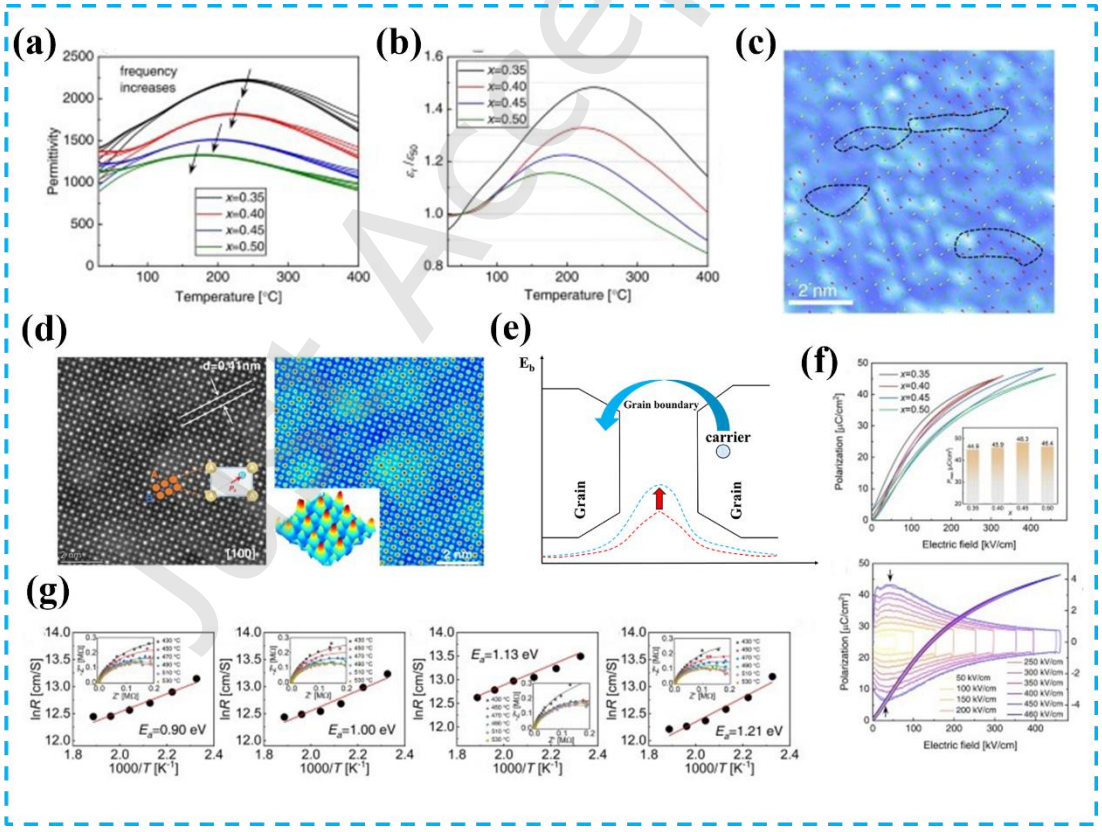

Fig. 21 (a) Temperature-dependent ε_r and tanδ for x=0.35, 0.40, 0.45, and 0.50. (b) $\varepsilon_r/\varepsilon_{50}$ as a function of temperature measured at 1 kHz. (c) The polarization vector. d) High-resolution TEM image of BSB-0.5 ceramic. (e) Enhanced insulation performance and

domain structure of BNKT through ST-BMN doping. (g) Relationship between temperature and grain boundary resistance. (h) *P-E* loops and *I-E* curves for x=0.35, 0.40, 0.45, and 0.50. Reproduced with permission from Ref. [9] Copyright © 2024 SPRINGER NATURE

Furthermore, Lai *et al.* proposed a synergistic regulation strategy by doping $Sr_{1/2}Nd_{1/3}(Mg_{1/3}Nb_{2/3})O_3$ (NSMN) into the BNT-based ceramics. As demonstrated in **Fig. 22**(a-b), it was evident that the *P-E* loops became slimmer as the NSMN content increased, which led to an enhanced ΔP. This improvement was attributed to the disrupted ferroelectric order and the formed PNRs induced by the incorporation of Nb^{5+} (**Fig. 22**(c)). Moreover, the introduction of Mg^{2+} and Nb^{5+} formed the wide-bandgap compounds (Nb_2O_5 and MgO), as illustrated in **Fig. 22**(d) **and Fig. 22**(h), thereby reducing the grain size (from 1.83 μm to 0.96 μm). The introduction of Nd^{3+} at the A-site substitutes part of the volatile Bi^{3+} and Na^{+}, resulting in a decrease in oxygen vacancy concentration, which in turn reduces the mass transfer rate during ceramic sintering. In this situation, the local breakdown of doped BNT ceramics was effectively suppressed. Simultaneously, **Fig. 22**(e-g) revealed that the multivalent states and different ionic radii of dopants suppressed the formation of oxygen vacancy, thereby reducing dielectric loss and yielding a macroscopic enhancement in impedance [309]. Furthermore, Long *et al.* [310] proposed that introducing $Nd(Mg_{0.5}Hf_{0.5})O_3$ (NMH) into $0.94Bi_{0.5}Na_{0.5}TiO_3$–$0.06BaTiO_3$ (0.94BNT–0.06BT) promotes the formation of short-range ordered PNRs, thereby enhancing the energy storage efficiency of the ceramics. Local heterogeneous structures formed in Bi-rich and Ti-rich regions give rise to small-

sized nanodomains with high polarization intensity. The multiscale polymorphic domain structure, comprising coexisting rhombohedral/tetragonal phase nanodomains and PNRs, achieves high polarization coupled with low hysteresis. Excellent electrical insulation is collectively attributed to the high insulation resistivity, submicron-scale grain size, and wide band gap achieved through NMH doping. Under multiscale synergistic effects, BNT-BT-0.25NMH delivers a W_{rec} of 7.82 J/cm^3 and an ultrahigh η of 93.1% at a moderate electric field of 400 kV/cm.

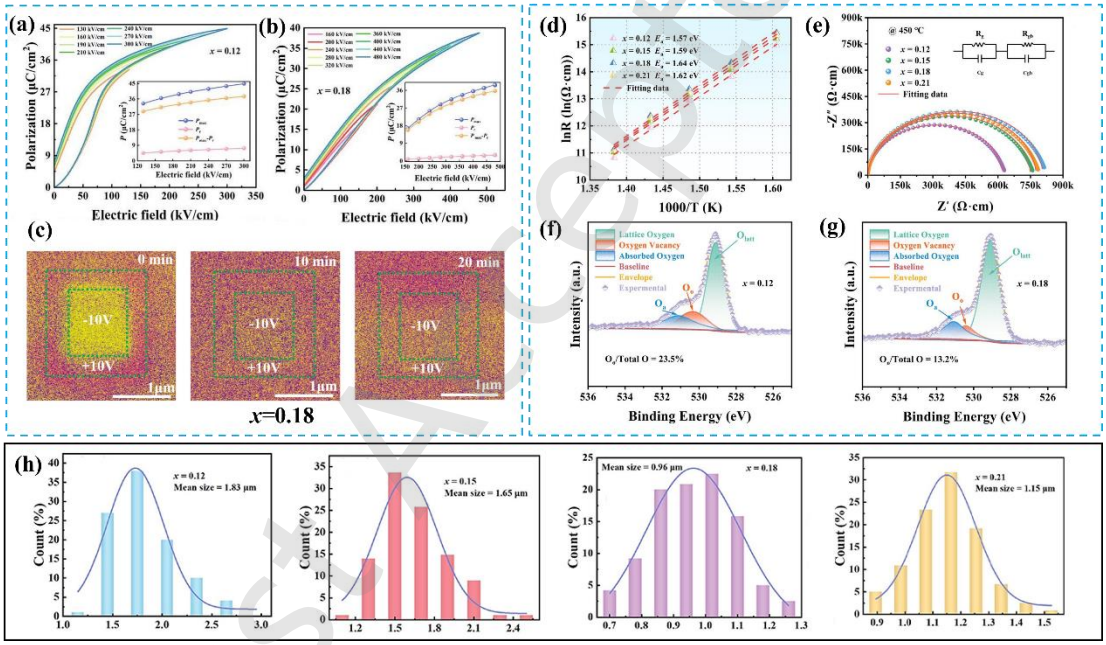

Fig. 22 (a-b) Unipolar *P-E* loops of (1-*x*)BNT-*x*NSMN ceramics for *x*=0.12, 0.18. (c) PFM images of pure BNT and 0.82BNT-0.18NSMN ceramics. (d) Resistivity-Temperature Arrhenius Plots. (e) Complex impedance spectra of each component. (f)-(g) XPS of O1s for *x*=0.12 and *x*=0.18 ceramics. (h) Average grain size distribution. Reproduced with permission from Ref. [309] Copyright © 2025 Elsevier Ltd.

In moderate and high electric fields, microstructural design serves as an effective strategy to further break through the upper limit of breakdown field strength. The core–

shell structure is regarded as a useful approach to reduce local electric field concentration and leakage current, while improving wide-temperature stability [311]. It was found from the microstructure of the BNT-$KTaO_3$-2%$LiCO_3$ ceramic in **Fig. 23**(a-f) that the core-shell microstructure was successfully formed in this ceramic. The formation of the core-shell microstructure was related to the limited diffusion of Ta^{5+}, and it was favorable to enhance the E_b of BNT-$KTaO_3$ ceramic (see **Fig. 23**(g)). Interestingly, the existence of the *R* phase and *T* phase was found in both core and shell regions of BNT-$KTaO_3$-2%$LiCO_3$, resulting in a high P_{max}. As a result, the x=2 ceramic achieved an excellent W_{rec} of 5.07 J/cm^3 and a good η of 85.17% under 440 kV/cm (see **Fig. 23**(h-j)) [312]. As we mentioned above, microstructural heterogeneity of dielectric ceramics, such as core-shell architectures and polymorphic nanodomain boundaries, provides another effective avenue to modulate polarization and breakdown behaviors. Currently, the introduction of local microstructures delays polarization saturation and deflects electric trees. However, the inherent mismatch in permittivity and electrical conductivity at heterogeneous structural boundaries leads to the localized electric field stress concentration. If the interface is abrupt or fails to achieve a graded transition, localized space-charge accumulation occurs, ultimately resulting in a breakdown avalanche. Therefore, interface engineering for enhancing the energy storage performance of dielectric ceramics requires precise matching of bandgaps and impedances across heterogeneous regions. Based on the descriptions earlier, the energy storage properties of representative BNT-based ceramics under moderate electric fields are summarized in **Table 2**.

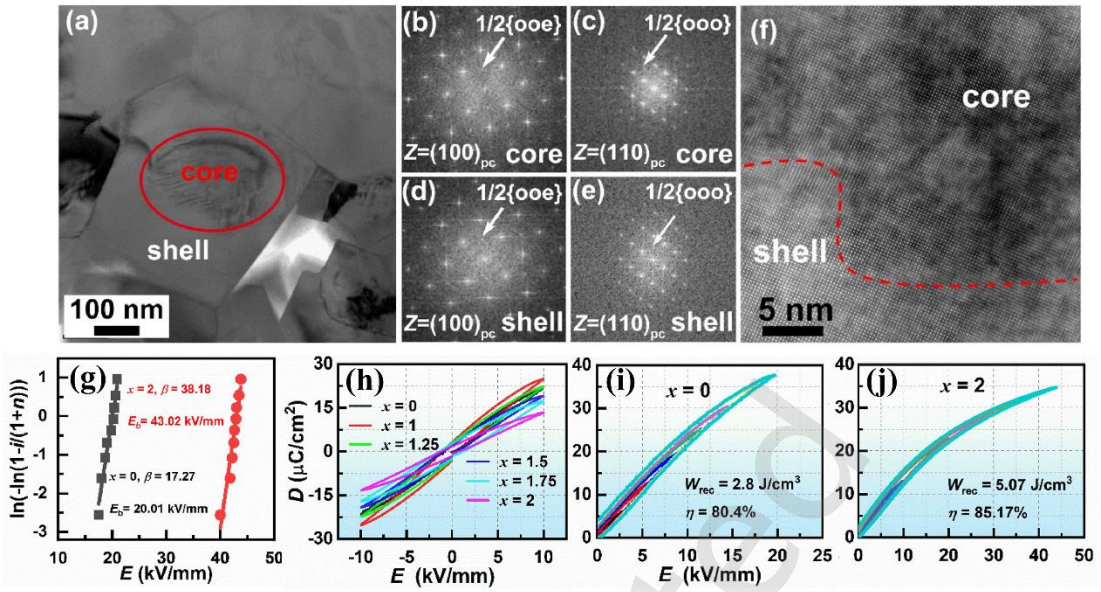

Fig. 23 (a) Bright-field TEM images of the x=2 ceramics. (b) electron diffraction patterns for the core and shell regions recorded along the (100)pc and (110)pc orientations. (c) atomic-scale HAADF-STEM image near the core/shell interface. d)Weibull distributions of E_b and corresponding P-E loops for the x=0 and x=2 ceramics. Reproduced with permission from Ref [313]. Copyright © 2020 Royal Society of Chemistry

To conclude, the moderate E-field region requires a careful balance between polarization and voltage endurance. Delaying polarization saturation is primarily achieved by adjusting the t, lowering the dielectric constant, and stabilizing antiferroelectric or relaxor states. Meanwhile, voltage endurance is effectively enhanced by grain refinement, bandgap broadening, defect dipole compensation, and core-shell heterostructure design. Among these methods, a multiscale synergistic modulation strategy integrating polymorphic nanodomain coexistence with grain boundary engineering exhibits exceptional efficiency. Therefore, the multiscale design strategy should be widely adopted to balance polarization behavior and E_b for achieving

excellent energy storage performance in BNT-based ceramics in a moderate *E*-field region.

Table 2 Summary of energy storage properties of BNT-based ceramics under moderate electric fields.

Ceramics system	E_b (kV·cm^{-1})	P_{max} (μC·cm^{-2})	P_r (μC·cm^{-2})	W_{rec} (J·cm^{-3})	η (%)	Ref.
$0.7(0.65BNT\text{-}0.35BT)\text{-}0.3SrZr_{0.5}Ti_{0.5}O_3$	302	-	-	4.32	93.48	[270]
$0.84BNT\text{-}0.16KNbO_3$	320	~36	~1.3	5.2	88	[314]
$Bi_{0.4465}Na_{0.4465}Ba_{0.057}La_{0.05}TiO_3\text{-}xSr_{0.85}Bi_{0.1}TiO_3$	320	43.07	~2	4.55	~90	[141]
$0.88[0.7BNT\text{-}0.3SBT]\text{-}0.12Sr(Zn_{1/3}(Nb_{0.85}Ta_{0.15})_{2/3})O_3$	330	~40	--	5.2	91	[315]
$(NaBaBi)_{0.205}(SrCa)_{0.1925}TiO_3$	335	~40	~2.8	3.86	-	[316]
$0.9BNT\text{-}0.1(0.5Ba_{0.7}Ca_{0.3}TiO_3\text{-}0.5BaTi_{0.8}Zr_{0.2}O_3)$	360	~32.7	~7.7	3.49	64.9	[317]
$0.7BNT\text{-}0.3Na_{0.91}Bi_{0.09}Nb_{0.94}Mg_{0.06}O_3$	370	~37	-	5.54	87	[285]
$0.95(0.9BNT\text{-}0.1Ba_{0.85}Ca_{0.15}Zr_{0.1}Ti_{0.9}O_3)\text{-}0.05BaSnO_3$	378.6	-	-	4.97	84.4	[238]
$0.8BNT\text{-}0.2NaTaO_3$	380	~30	~2.5	4.21	77.8	[243]
$0.70BLNBT\text{-}0.3SrTi_{0.875}Nb_{0.103}$	380	~34	-	4.2	89.3	[318]
$0.85(0.7BNT\text{-}0.3SBT)\text{-}0.15Bi(Mg_{0.5}Zr_{0.5})O_3$	385	~54.8	~4.22	6.75	79.44	[281]
$0.76BNT\text{-}0.04SZ\text{-}0.2NN\text{-}0.15MnO_2$	387	~46	~4.6	7.05	65	[294]
$0.78BNT\text{-}0.22NaNbO_3$	390	~47	-	7.02	85	[287]
$0.97(BNT\text{-}Sr_{0.7}Sm_{0.2}TiO_3)\text{-}0.03La(Mg_{2/3}Nb_{1/3})O_3$	390	~34	-	5.94	86.9	[278]
$0.8BNT\text{-}0.2Ba_{0.7}Sr_{0.3}Zr_{0.8}Sn_{0.2}O_3$	400	50	-	7.4	89	[319]
$(0.94BNT\text{-}0.06BT)\text{-}BiMg_{2/3}Nb_{1/3}O_3$	420	-	-	6.3	79.6	[320]
$0.6[0.955BNT\text{-}0.045Ba(Al_{0.5}Ta_{0.5})O_3]\text{-}0.4CaTiO_3$	440	-	-	5.81	97.8	[277]
$[(Bi0.5Na0.5)_{0.94}Ba_{0.06}]0.82La_{0.12}TiO_3$	440	-	-	6.69	87	[321]
$0.82BNT\text{-}0.18Sr_{1/2}Nd_{1/3}(Mg_{1/3}Nb_{2/3})O_3$	480	37.83	2.04	6.4	86.4	[309]

Notes: Given that factors such as the type of electrode material, the area of electrodes, testing temperature, thickness, and geometry can exert certain influences on the measurement results, and considering the inherent discrepancies in the evaluation of breakdown fields, the data listed in the table are presented for reference and comparison only.

4.3 Improving Energy Storage Performance under High *E*-Fields

As a promising energy storage material, it should be capable of wider applications in modern electronic ceramic industries, especially under extremely applied electric fields. Therefore, the energy storage performance of bulk BNT-based ceramics under high electric fields is of great importance. **Fig. 24** displays the schematic illustration of strategies for BNT-based energy storage ceramics under high electric fields. It is considered that the multi-phase structure, multi-domain engineering, and macro-structure design are effective ways to maintain high polarization and improve E_b for the BNT-based ceramics, which is based on meeting the small grain size, low leakage current, wide band-gap, *etc*.

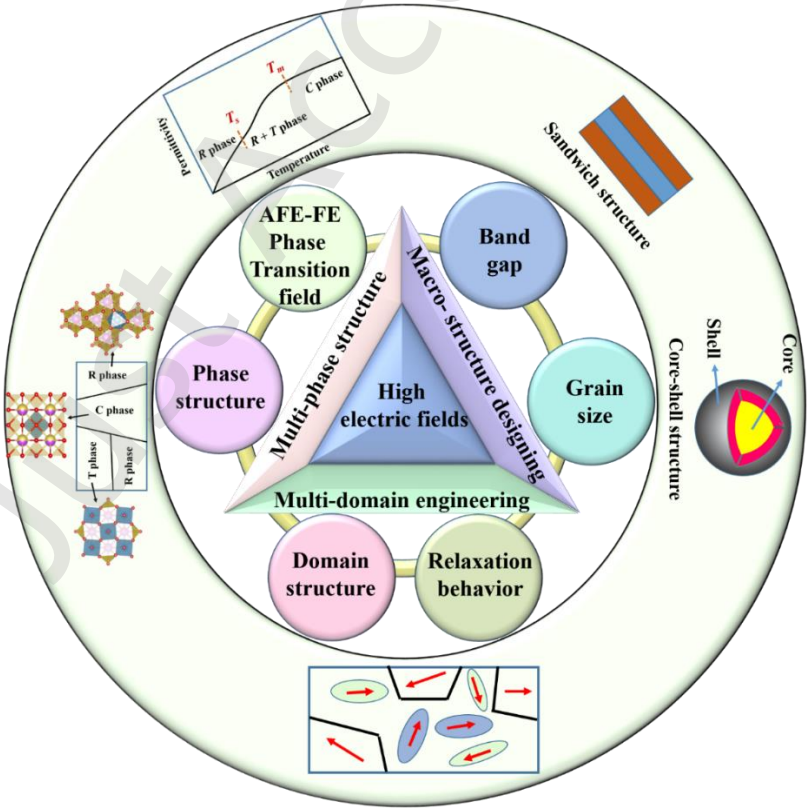

Fig. 24 Schematic illustration of the strategies for energy storage performances in BNT-based ceramics under high electric fields.

Notably, grain refinement can effectively modulate the microstructure of dielectric ceramics, thereby enhancing the E_b to achieve superior energy storage performance [322]. Zhou *et al*. introduced La^{3+} ions into the A-sites of 0.9BNT-0.1$SrAl_{0.5}Nb_{0.5}O_3$ ceramics, which remarkably reduced the grain size and suppressed oxygen vacancies after partially substituting La^{3+} for Bi^{3+}. Atomic-scale studies revealed that the introduction of La^{3+} ions induced a phase transition from the rhombohedral and tetragonal phases to the cubic phase. Additionally, the size of PNRs was further reduced to 2–3 nm due to the weaker orbital coupling of La-O bonds compared to Bi-O bonds, resulting in ultrafast polarization response and low polarization hysteresis. Consequently, a recorded W_{rec} of 11.2 J/cm^3 under 820 kV/cm was achieved in this optimized ceramic [323]. Particularly, Zhu *et al.* incorporated $Bi(Mg_{0.5}Zr_{0.5})O_3$ into the BNST ceramic, which restrained grain growth and formed a compact structure to reduce the concentration of oxygen vacancies [324]. This was favorable for enhancing the activation energy and improving the E_b. Additionally, the induced random field broke the long-range polar order and increased the number of high-dynamic PNRs, suppressing the early polarization saturation. Fortunately, an ultrahigh W_{rec} of 8.46 J/cm^3 and high efficiency of 85.9% were achieved in 0.9$(Bi_{0.5}Na_{0.5})_{0.65}Sr_{0.35}TiO_3-0.1Bi(Mg_{0.5}Zr_{0.5})O_3$ ceramic, as illustrated in **Fig. 25**. Wang *et al.* achieved a record-breaking ultrahigh energy density and excellent efficiency (W_{rec} = 8.58 J/cm^3, η = 93.5%) simultaneously under a high electric field of 565 kV/cm for the BNST-0.08BMT ceramic through employing domain and bandgap engineering. Significantly, other similar studies have successfully improved the energy storage performance of BNT-

based ceramics under high electric fields [325, 326].

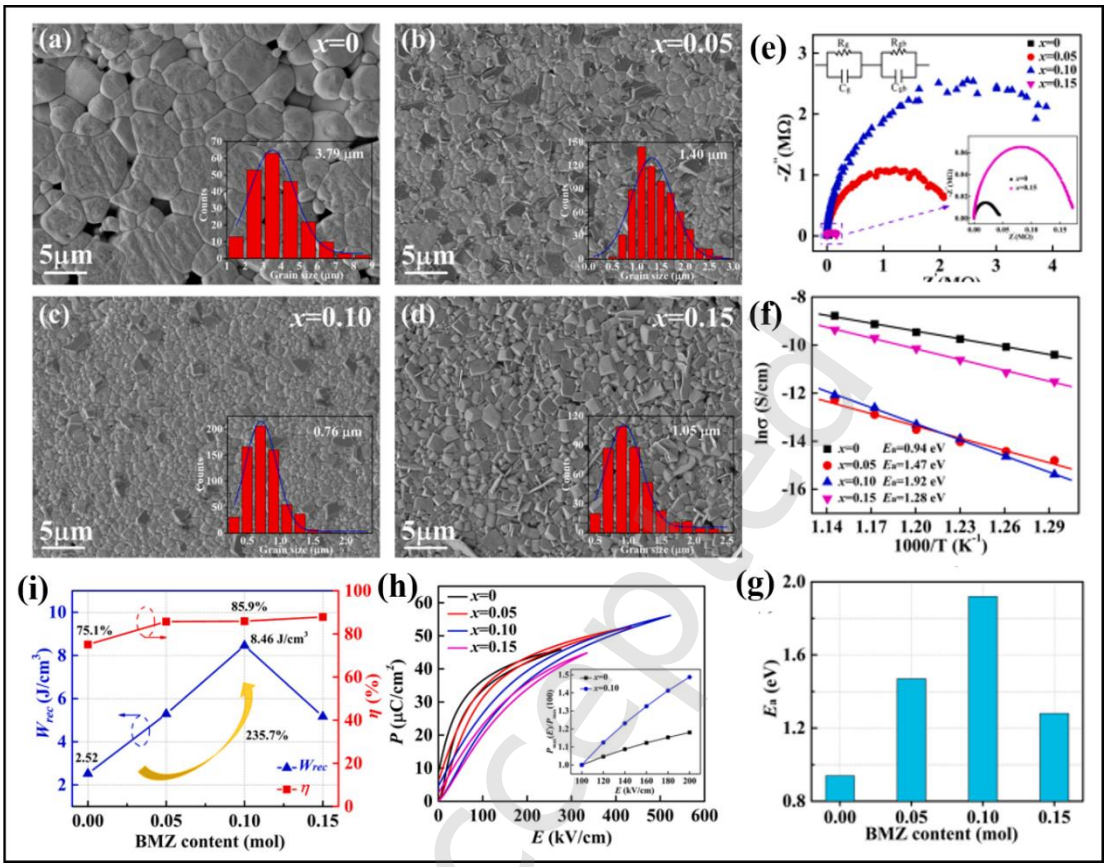

Fig. 25 (a-d) SEM pictures, (e)complex impedance spectra of the samples tested under 500 ℃, (f) the Arrhenius lines, variations of E_a (g) under various BMZ content, (h) unipolar *P*-*E* loops, and the corresponding inset shows the change of normalized P_{max} at different electric fields for x=0 and x=0.10, (i) the largest W_{rec} and η under various BMZ contents. Reproduced with permission from Ref [324], Copyright © 2022 Elsevier Ltd.

Also importantly, constructing the MPB or further preparing the relaxor antiferroelectric ceramic combined with the characteristics of AFE and RFE offers a feasible way to enhance the properties of BNT-based ceramics [327, 328]. Considering this, Qi *et al*. fabricated the (1-x)BNT-$x$$NaNbO_3$ (BNT-NN) ceramics system [329]. As shown in **Fig. 26**(a), the depolarization temperature gradually reduced until it

disappeared with the rise of NN content, and a nearly temperature-stable permittivity was achieved when it exceeded x=0.2. This indicated that incorporating the NN AFE into the BNT RFE could enhance the dielectric relaxation feature. Moreover, it was observed from **Fig. 26**(b-c) that the stability of the room temperature P4bm AFE phase was within the range of $0.2 \leq x \leq 0.4$, and the *P-E* loops became slimmer as the NN content increased. As a result, slim *P-E* loops with a record-high W_{rec}~7.02 J/cm^3 and a high η~85% were simultaneously achieved in the 0.78BNT-0.22NN bulk ceramic. Additionally, Ma *et al*. also explored the impact of the ferroelectric $BaTiO_3$ on the energy storage performances of BNT ceramics. **Fig. 26**(d) displayed the phase structure transition diagram of the BNT-BT system. It was found that the unique relaxor *P4bm* AFF phase with nanodomain was displayed in 0.07~0.1, while the complex domain in the FE state was accompanied by the long-range order ferroelectric and short-range order nanodomains at room temperature when $x \leq 0.06$. For the ceramics with $x \geq 0.11$, nanodomains with P4mm symmetry and large lamellar ferroelectric domains, with mixed domains, were discovered [330]. Hereafter, it was found that the addition of $Sr(Al_{0.5}Ta_{0.5})O_3$ into the BNT-BT system was effective in reducing the grain size. This design strategy disrupted the long-range ferroelectric order of this composition and constructed the polymorphic PNRs structure. Consequently, the optimized $0.85Bi_{0.47}Na_{0.47}Ba_{0.06}TiO_3$-$0.15Sr(Al_{0.5}Ta_{0.5})O_3$ ceramic simultaneously achieved a remarkable W_{rec} of 8.33 J/cm^3 and an excellent η of 90.8% [331], as shown in **Fig. 26** (e-f).

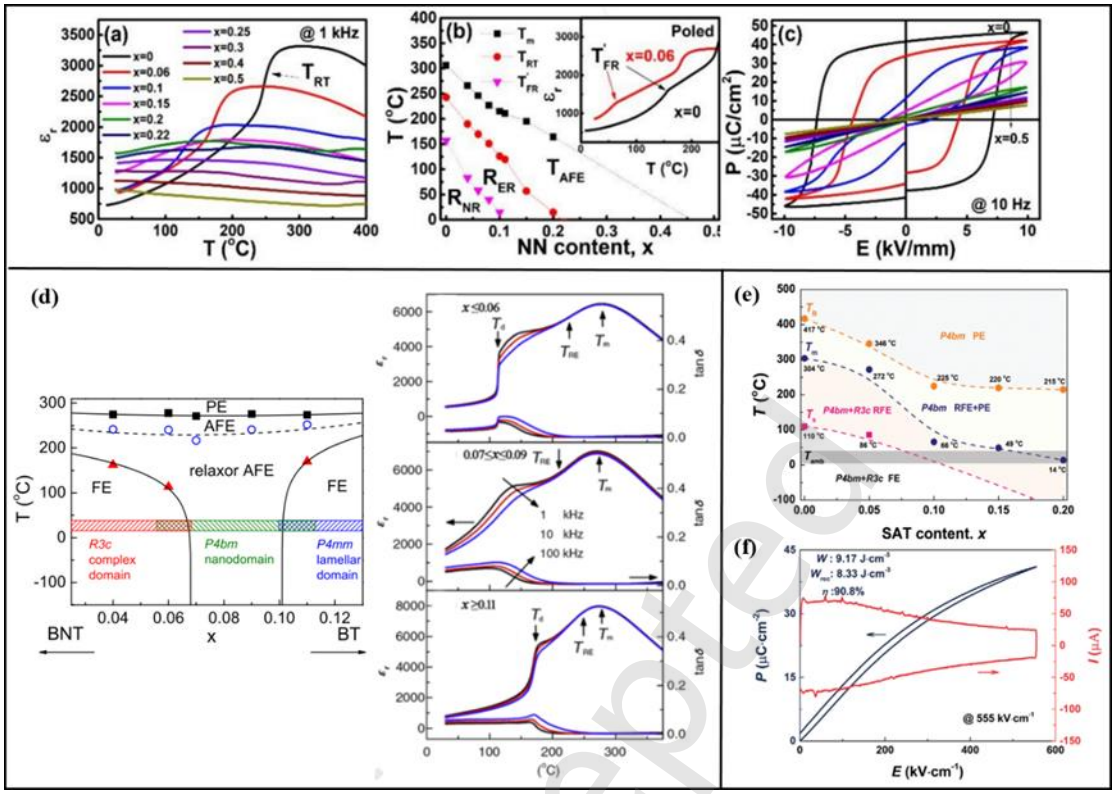

Fig. 26 (a) Temperature-dependent dielectric permittivity ε_r for (1-*x*)BNT-*x*NN ceramics, (b) the phase diagram of (1-*x*)BNT-*x*NN binary system, (c) *P*-*E* loops of (1-*x*)BNT-*x*NN ceramics. Reproduced with permission from Ref [329]. Copyright ©2019 Royal Society of Chemistry. (d) A schematic phase diagram for structural phase transitions in unpoled (1-*x*)BNT-*x*$BaTiO_3$ ceramics, and temperature-dependent ε_r and tanδ of (1-*x*)BNT-*x*BT ceramics. Reproduced with permission from Ref. Reproduced with permission from Ref [225]. Copyright ©2010 AIP Publishing. (e) Possible composition temperature has a diagram of (1-*x*)BNBT-*x*SAT system (Tamb indicates the ambient temperature), (f) *P*-*E*, *I*-*E* loops of *x*=0.15 ceramic. Reproduced with permission from Ref [284]. Copyright © 2023 Advanced Science News.

Recently, Liu *et al.* adopted a modulation design of the structure distortion (δ) and the *t* to improve the energy storage performance of BNT-based ceramics. The long-range correlation of polar vectors was broken, which induced the establishment of

short-range polar clusters with lower symmetry of polymorphic *R*, *T*, and *O* phases when $x = 0.15$. Meanwhile, a large polar length exists in the Bi-rich polar clusters, and strong local polar fluctuations are shown in the nanoscale structure (See **Fig. 27**(a)). This indicated that the $0.85(0.75BNT\text{-}0.25BaTiO_3)\text{-}0.15BaZrO_3$ ceramic could obtain a large P_{max} and a slender *P-E* loop. Remarkably, a new record W_{rec} of 13.6 J/cm^3 and high η of 94% at 660 kV/cm were achieved in the x=0.15 ceramic, as shown in **Fig. 27**(b-c) [332]. Afterward, Zhao *et al.* employed the phase-field simulation method to design a novel BNT-based ceramic with high-energy storage performance. They optimized the polymorphic PNRs of the BNT-$Bi_{0.5}K_{0.5}TiO_3$ (BNKT) binary system by incorporating $Sr(Sc_{0.5}Nb_{0.5})O_3$. Consequently, the coexistent multiphase nanoregions destroyed the long-range ferroelectric order and produced abundant small-sized PNRs. Moreover, the randomly distributed nanoregions of different polarization directions and magnitudes could reduce polarization anisotropy, and the enhancement in polarization magnitude implied that the internal field was strong, as illustrated in **Fig. 27**(d). These factors could all lead to a more accessible and quicker polarization response to the external electric field, resulting in higher η (96.3%) and better W_{rec} (9.22 J/cm^3) achieved in the $0.8BNKT\text{-}0.2Sr(Sc_{0.5}Nb_{0.5})O_3$ ceramic (see **Fig. 27**(e-f)) [333]. Encouragingly, an ultrahigh W_{rec} of 8.33 J/cm^3 and a high η of 90.8% at 555 kV/cm were obtained in the $0.85(0.94BNT\text{-}0.06BaTiO_3)\text{-}0.15Sr(Al_{0.5}Ta_{0.5})O_3$ ceramic via a polymorphic PNRs design [331]. These results demonstrate that the synergistic effect of multi-phase and multi-domain is a potential route to achieve excellent energy storage performance of BNT-based ceramics at high electric fields.

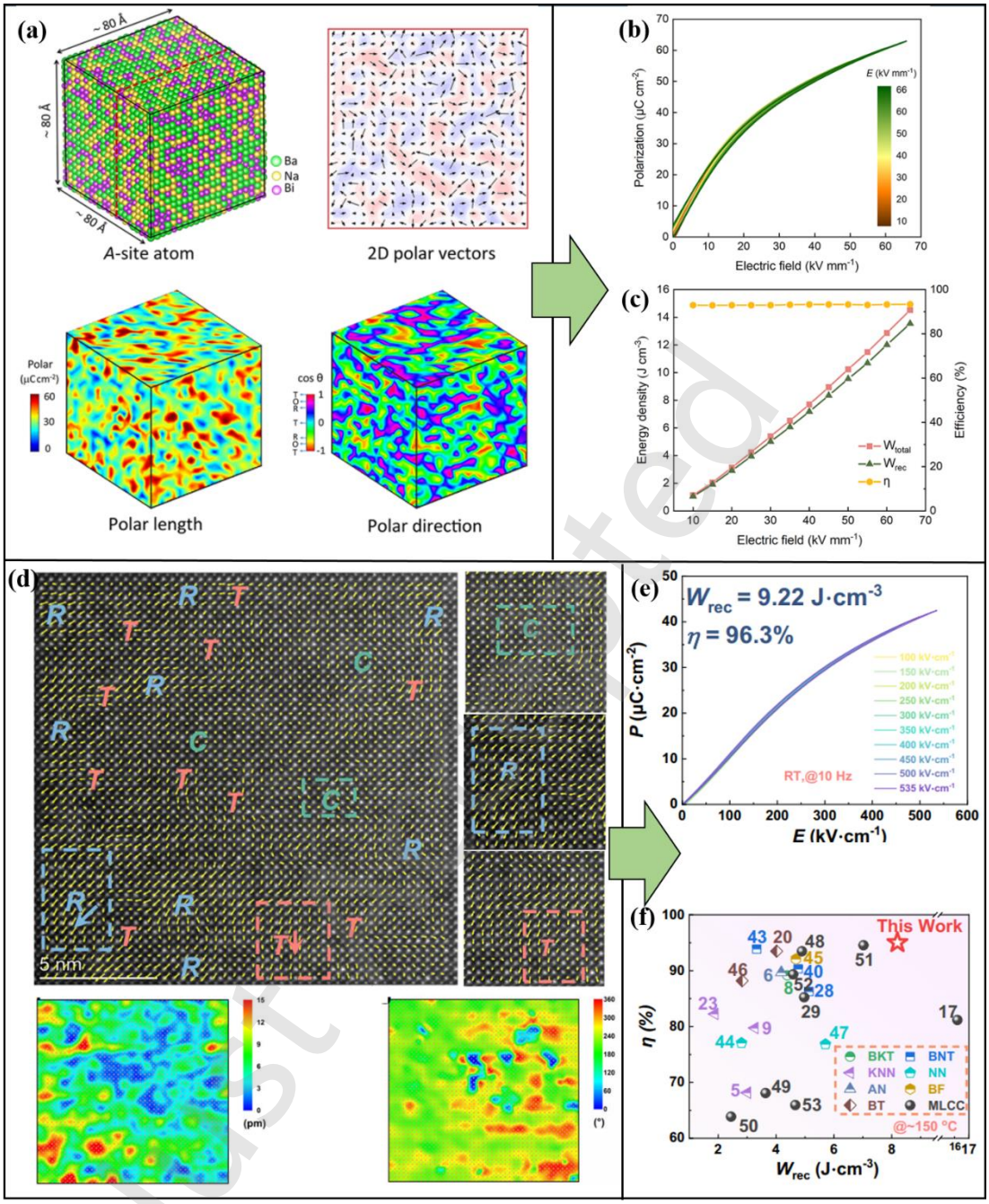

Fig. 27 (a)The A-site atom distribution and the corresponding polar mapping for *x*=0.15 ceramic, (b) electric field-induced unipolar *P*-*E* loops of the BNT-25BT-*x*BZ (*x*=0.15) bulk ceramics, (c) calculated energy density and efficiency of the BNT-25BT-*x*BZ (*x*=0.15). Reproduced with permission from Ref. [332]. Copyright © 2023 American Chemical Society. (d) Crystal structure analysis and local structure analysis of the BNKT-20SSN, (e) room-temperature *P*-*E* loops were measured till the critical

electric field of the BNKT-20SSN ceramic, (f) comparisons of W_{rec} versus η (~150 °C) between our work with some recently reported lead-free bulk ceramics and certain MLCCs. Reproduced with permission from Ref [333]. Copyright © 2023 Nature Publishing Group

Under a very high electric field, the formation of oxygen vacancies in BNT-based ceramics will increase oxide ion conductivity and grain growth, which further deteriorates the energy storage performance of BNT-based ceramics. This phenomenon is mainly ascribed to the volatilization of Bi and Na elements during the sintering process. To address this issue, Yan *et al.* utilized A-defect engineering with Bi-excess and Na-deficiency to weaken the influence of oxygen vacancies. The results showed that the average grain size decreased from 1.61 μm to 1.15 μm with an increase in x from 0 to 0.10, which was related to the decrement of oxygen vacancy concentration due to the Bi-excess and Na-deficiency, as given in **Fig. 28**(a-c). In addition, the stability of the dielectric constant of $0.75Bi_{(0.5+x)}Na_{(0.5-x)}TiO_3$-$0.25SrTiO_3$ (BNST-x) was gradually elevated as the content x increased. An ultrahigh W_{rec} of 5.63 J/cm^3 together with a high η of 94% was obtained in the x=0.08 ceramic, as shown in **Fig. 28**(d-e) [334]. Zhou *et al*. [335] incorporated $Sm(Mg_{2/3}Sb_{1/3})O_3$ (SMS) into the $Bi_{0.47}Na_{0.47}Ba_{0.06}TiO_3$ (BNBT) matrix to form a solid solution, which effectively modulated the defect concentration. The disparity in ionic radii among Sm^{3+}, Mg^{2+}, and Sb^{5+} ions in SMS induced lattice strain, thereby refining the microstructure, as substantiated by the reduced average grain size of 2.14 μm observed in BNBT-0.16SMS ceramic. Concurrently, this compositional tuning suppressed oxygen vacancy formation,

evidenced by a marked decline in oxygen vacancy concentration from 16.59% to 8.75%. These combined effects, including grain refinement, reduced oxygen vacancies, and enhanced insulating properties, collectively led to a notable increase in E_b up to 760.0 kV/cm. Consequently, an ultrahigh W_{rec} of 13.6 J/cm^3 and an energy storage efficiency of 83.9% were achieved. Collectively, defect engineering strategies have yielded substantial advancements in the electrostatic energy storage capabilities of BNT-based ceramics.

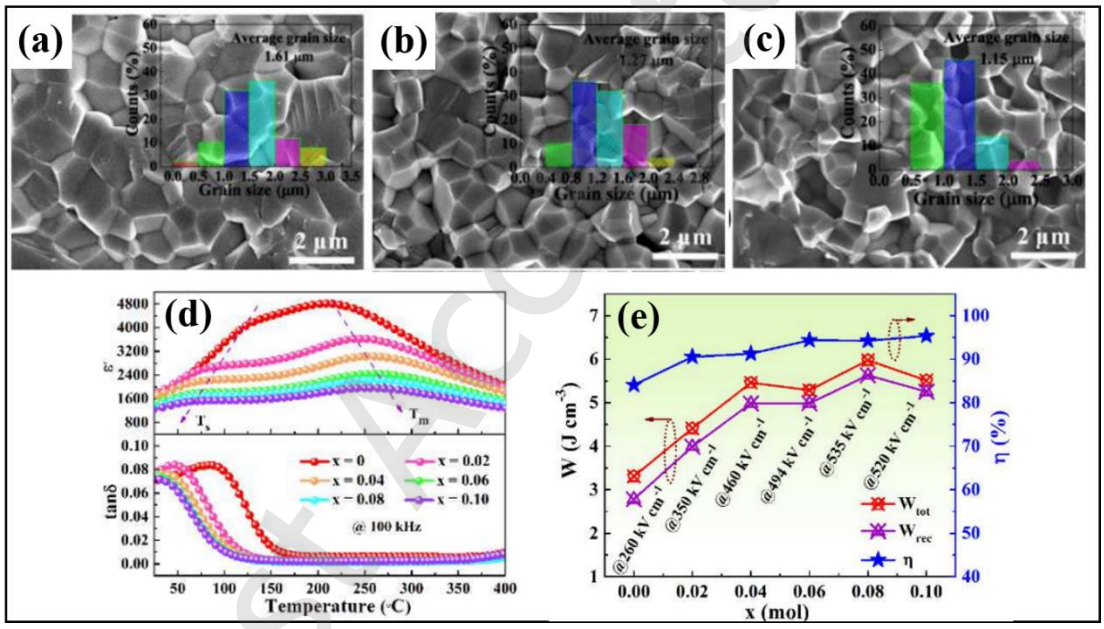

Fig. 28 (a-c) The SEM images of the cross-sections and the grain size distribution for BNST-x ceramics: x = 0, x = 0.08, x = 0.10, (d) temperature-dependent ε' and tanδ of the BNST-x ceramics at 100 kHz, (e) the W_{total}, W_{rec}, and η of the BNST-x ceramics and their breakdown at room temperature. Reproduced with permission from Ref. Reproduced with permission from Ref [334]. Copyright © 2023 Elsevier Ltd.

In addition, the energy storage performance of BNT-based ceramics can be improved by implementing the macrostructure design [336-340]. As shown in **Fig. 29**

(a), ferroelectric ceramics and linear-like ceramics were selected as the outer layer and middle layer, respectively. This ceramic showed the obvious sandwich structure confirmed by the cross-section SEM images (see **Fig. 29**(b-d)). By optimizing the number of layers between the ferroelectric ceramics and linear-like ceramics, the composite ceramics simultaneously exhibit the large P_{max} of ferroelectric ceramics and the high E_b of the linear ceramics, leading to a high W_{rec} of 6.78 J/cm^3 and a very high η of 89.7% under 572 kV/cm, as shown in **Fig. 29**(e). Additionally, Yan *et al.* also reported another work about the sandwich-structured lead-free $Bi_{0.5}Na_{0.5}TiO_3$ relaxor ferroelectric ceramics with high energy storage performances, which further demonstrated that constructing the sandwich structure was a potential way to achieve excellent energy storage performances of BNT-based ceramics [341].

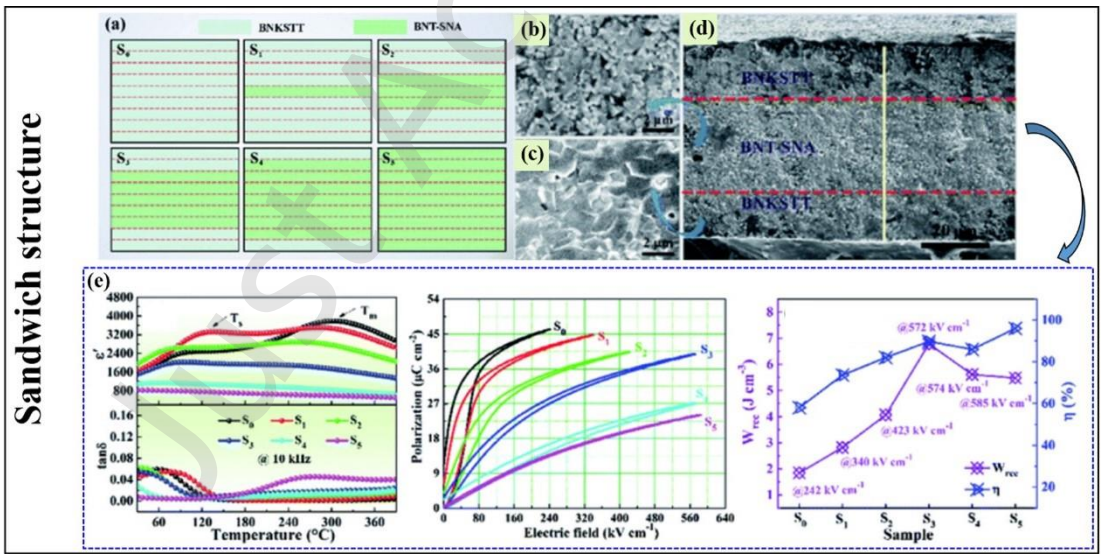

Fig. 29 (a) Schematic diagram of the prepared lead-free ceramics with sandwich structures, (b) cross-section images of the BNKSTT layer, (c)BNT-SNA layer, (d) and S_3, (e) temperature-dependent ε' and tanδ for different samples, unipolar *P-E* loops of their breakdown, W_{rec}, and η for the various samples. Reproduced with permission from

Ref [341]. Copyright © 2020 Royal Society of Chemistry.

Moreover, the recent dual-phase design has achieved excellent performance in BNT-based ceramics, attracting widespread attention. Xiong *et al.* proposed a dual-phase strategy to realize the high reversible polarization and simultaneously enhance the E_b by introducing $CdZrO_3$ into the BNT-BT system. As shown in **Fig. 30**(a-b), the dual-phase structure could be clearly observed based on the SEM images. It was observed from **Fig. 30**(c) that this engineered structure achieved an excellent energy storage performance featuring an ultrahigh W_{rec} of 23.6 J/cm^3 and a high η of 92% under an ultrahigh applied electric field of 990 kV/cm. As illustrated in **Fig. 30**(d), the C2 phase was mainly composed of Cd-rich compounds, with a calculated entropy as high as 1.3R. This finding implied a stronger lattice distortion and a smaller grain size, further contributing to the polarization diversity. There is no direct evidence that the dual-phase structure is responsible for achieving ultrahigh breakdown field strength; however, the doping of Zr^{4+} increases the band gap of the compound, thereby enhancing the intrinsic E_b of the material. Besides, it was clearly observed in **Fig. 30**(e-f) that introducing the C1 and C2 phases could enhance the local heterogeneity, resulting in a more diverse domain structure [153]. It is worth noting that the CdO, as a highly toxic heavy metal oxide, generates harmful dust during the ceramic sample preparation, requiring operators to strictly adopt protective measures such as wearing respirators and working inside fume hoods. Alternatively, in addition to Cd element, the A-site substitution by Ca and certain rare-earth elements with smaller ionic radii (such as Nd and Sm) can likewise enhance the polarization strength of BNT-based ceramics, serving

as an effective strategy for polarization regulation.

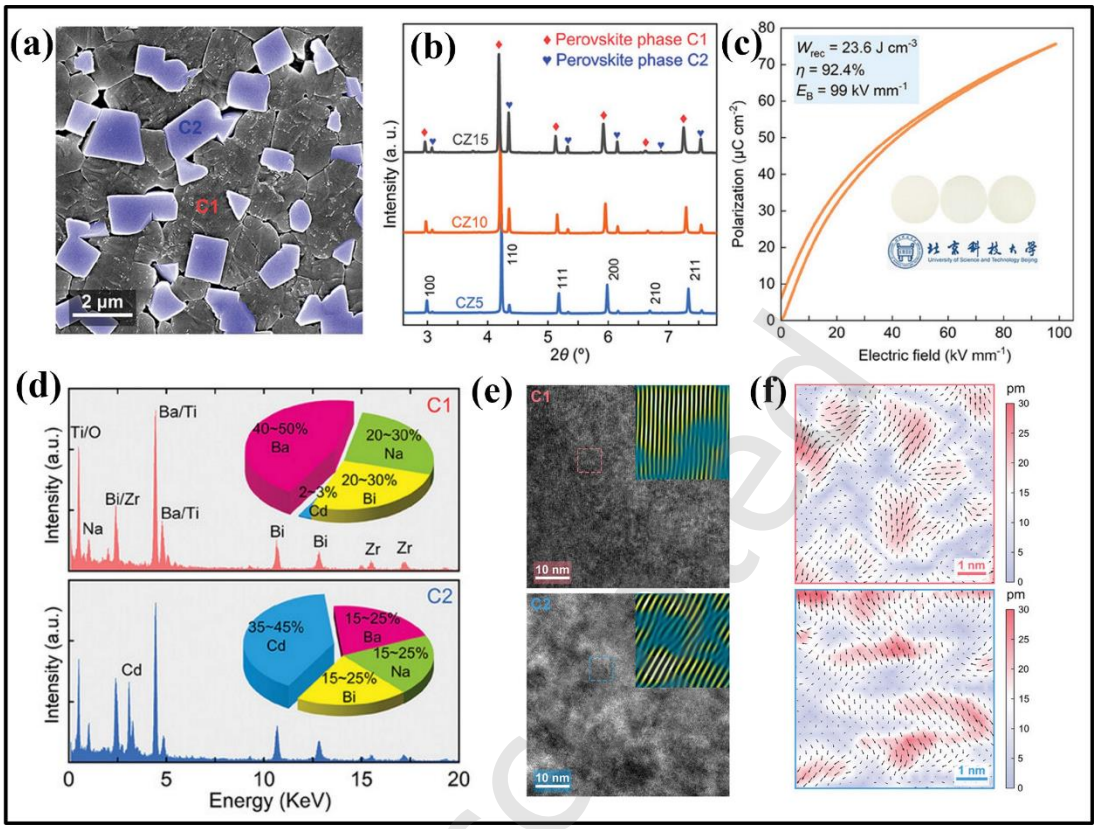

Fig. 30 (a) SEM micrograph of the polished and acid-etched surface. (b) X-ray diffraction analysis of dual-phase CZ10 ceramic. (c) Unipolar *P*-*E* loop of 0.5BNT-0.4BT-0.1$CdZrO_3$. (d) The EDS patterns of dual-phase. (e) HR-TEM images recorded along the $[110]_c$ direction. (f) The atomic displacement vector mapping. Reproduced with permission from Ref [153]. Copyright © 2024 Wiley-VCH GmbH.

Recently, the concept of high entropy has been introduced into dielectric ceramics, especially providing a guided strategy for developing the BNT-based ceramics with high energy storage performance [342-347]. Specifically, the random distribution of multiple cations with varying ionic radii and valence states at the lattice sites increases the configuration entropy, generating intense local lattice distortions, random stresses, and electric field fluctuations. This enhanced random field disrupts the long-range

ferroelectric order, driving its fragmentation into ultrasmall PNRs with a multi-phase random orientation. Consequently, the polarization anisotropy is significantly reduced, lowering the switching barrier. Under an external electric field, a much larger field intensity is required to force these decoupled, highly dynamic clusters into a stable long-range ordered state, effectively delaying polarization saturation. Upon removal of the electric field, the ultrasmall PNRs promptly revert to a macroscopically nonpolar, chaotic state, minimizing the P_r to near zero, which achieves superior energy storage density and efficiency under high electric fields [348].

Previous work developed a lead-free relaxor ferroelectric ceramic of $(Bi_{0.5}Na_{0.5})_x(Sr_{0.25}Ba_{0.25}La_{0.25}K_{0.25})_{(1-x)}TiO_3$ (abbreviated as BNSLBKT-x) via a high-entropy strategy. The results showed that the optimized BNSLBKT-0.2 high-entropy ceramic achieved a high E_b of 510 kV/cm and a high W_{rec} of 4.6 J/cm^3 with η=86% [349]. Yang *et al.* [350] proposed a strategy involving A-site multi-ion doping combined with B-site Zr^{4+} substitution, designing a high-entropy relaxor ferroelectric ceramic of $(Na_{0.2}Bi_{0.2}Ba_{0.2}Sr_{0.2}Ca_{0.2})(Ti_{1-x}Zr_x)O_3$. The core mechanism involves enhancing the disorder at the B-site by introducing Zr^{4+}, which further refines the PNRs, weakens inter-regional coupling, delays polarization saturation, and optimizes E_b. When x=6, the ceramic achieves a high W_{rec} of 6.6 J/cm^3 and an ultrahigh η of 93.5% at 550 kV/cm, while also exhibiting excellent frequency/thermal stability and fast charge-discharge performance. More importantly, the emergence of machine learning has greatly improved design efficiency and reduced trial-and-error costs of novel dielectric ceramics. As we all know, the high-entropy strategy constructs strong local random

fields by introducing multiple ions with varying radii and valences in dielectric ceramics. These random fields effectively suppress long-range ferroelectric order and reduce the P_r, thereby significantly enhancing the energy storage efficiency of dielectric ceramics under moderate-to-high *E*-fields. However, excessive lattice chemical disorder, while pinning PNRs, also suppresses ferroelectric activity and depresses the P_{max}. This narrows the ΔP and limits further improvement in W_{rec}. To address this issue, current research tends to adopt synergistic strategies combining high entropy with defect dipoles or multiphase relaxor structures, enabling fine-tuning of the local random field strength in dielectric ceramics. Such approaches maintain a low P_r while alleviating the sacrifice of P_{max} caused by over-pinning, achieving simultaneous optimization of energy storage density and efficiency. Given this, Wang *et al.* selected a random forest model, collected data from 121 literature sources related to the BNT-based ceramics, and constructed a database with a total of 60 different descriptors. With the assistance of machine learning, they successfully designed the $(Bi_{0.36}Na_{0.34}La_{0.13}Sr_{0.17})(Ti_{0.86}Ta_{0.01}Mg_{0.08}Hf_{0.05})O_3$ high-entropy ($\Delta S \sim 1.8R$) near-linear RFEs, which possess refined grains, weakly coupled polar clusters, and low polarization anisotropy. Remarkably, a record-high W_{rec} of 20.7 J/cm^3 with a η of 86% was achieved for this material [351]. Benefiting from the various effective design strategies, the energy storage performances of advanced BNT-based ceramics under high electric fields are displayed in **Table 3**.

Overall, optimizing the energy storage performance of BNT-based ceramics under high *E*-fields aims to simultaneously maintain a high P_{max} and enhance the E_b under

extreme voltage stress. Contemporary high-field optimization strategies are comprehensively classified into several practical pathways, including domain and phase engineering (constructing multi-phase transitions or AFE/RFE features), defect engineering (A-site defect compensation and valence tuning), macrostructure design (sandwich-structured composites), and high-entropy multi-component configurations. Among these diverse strategies, the dual-phase heterostructure design and machine learning-assisted high-entropy strategies have encouraging performance records in breaking through conventional limits. The dual-phase configuration incorporating a high-entropy Cd-rich compound achieved a W_{rec} of 23.6 J/cm^3 and η of 92% under an ultrahigh field of 990 kV/cm [153]. In parallel, data-driven machine learning models successfully design near-linear high-entropy perovskite ceramics, delivering a record-high W_{rec} of 20.7 J/cm^3 [351]. The E_b of BNT-based ceramics is effectively enhanced by heterostructure design strategies, which deflect electrical breakdown pathways by dielectric properties mismatch across grains and grain boundaries. Subsequent research on second-phase engineering will focus on delineating solubility limits, fine-tuning compositional modulation, and optimizing sintering regimes. These efforts aim to engineer multi-phase solid solutions that transcend current dielectric breakdown thresholds, thereby realizing superior energy storage capabilities in BNT-based ceramics.

Table 3 Summary of energy storage performances of BNT-based ceramics under high electric fields.

Ceramics system	E_b (kV·cm^{-1})	P_{max} (μC·cm^{-2})	P_r (μC·cm^{-2})	W_{rec} (J·cm^{-3})	η (%)	Ref.

$0.85BNT\text{-}0.15AgNb_{0.5}Ta_{0.5}O_3$	510	~45	~7	6.6	72	[293]
$0.9BNST\text{-}0.1Bi(Mg_{0.5}Zr_{0.5})O_3$	522	-	-	8.64	85.9	[282]
$0.6BNT\text{-}0.28ST\text{-}0.12Bi_{0.5}Li_{0.5}TiO_3+0.5at\%Nb_2O_5$	520	50	-	8.63	89.6	[352]
$0.6(0.8Bi_{0.5}Na_{0.5}TiO_3\text{-}0.2NaNbO_3)\text{-}0.4SrTiO_3$	525	53.65	1.26	10.3	94	[353]
$BNT\text{-}Bi_{0.5}K_{0.5}TiO_3\text{-}0.2Sr(Sc_{0.5}Nb_{0.5})O_3$	535	~43	~0	9.22	96.3	[290]
$0.3(0.94BNT\text{-}0.06BT)\text{-}0.3Sr_{0.7}Nd_{0.2}TiO_3\text{-}1at\%Nb$	540	41	~2	8.08	92.1	[354]
$Bi_{0.2}Na_{0.2}Ba_{0.2}Sr_{0.2}Ca_{0.2}TiO_3\text{-}Li_2CO_3$	555	55	~5	8.33	90.8	[355]
$0.75Bi_{0.58}Na_{0.42}TiO_3\text{-}0.25SrTiO_3$	569	40	2	5.63	94	[334]
$0.85(Bi_{0.375}Na_{0.3}Sr_{0.25}K_{0.075})TiO_3\text{-}0.15Bi(Mg_{0.5}Sn_{0.5})O_3$	610	66.8	1.12	11.24	88.3	[356]
$0.9(Bi_{0.5}Na_{0.5})_{0.7}Sr_{0.3}TiO_3\text{-}0.1Sm(Mg_{2/3}Sb_{1/3})O_3$	650	~40	~2	8	82	[357]
$0.85(0.75BNT\text{-}0.25BaTiO_3)\text{-}0.15BaZrO_3$	660	63	3.8	13.6	94	[120]
$[0.6(Bi_{0.4}7Na_{0.47}Yb_{0.03}Tm_{0.01})TiO_3\text{-}0.4(Ba_{0.5}Sr_{0.5})TiO_3]\text{-}0.06Sr(Zr_{0.5}Hf_{0.5})O_3$	685	35	1.5	10.46	86.3	[358]
$(Na_{1/6}Bi_{1/6}Ca_{1/6}Sr_{1/6}Nd_{1/6}Li_{1/6})TiO_3$	700	59.01	1.21	18.2	85.6	[359]
$0.8[0.94BNT\text{-}0.06BT]\text{-}0.2Sm\ (Mg_{2/3}Ta_{1/3})O_3$	815	35.48	1.96	12.25	86.5	[360]
$(Bi_{0.36}Na_{0.34}La_{0.13}Sr_{0.17})(Ti_{0.86}Ta_{0.01}Mg_{0.08}Hf_{0.05})O_3$	950	58.5	3.8	20.7	86	[351]

Notes: Given that factors such as the type of electrode material, the area of electrodes, testing temperature, thickness, and geometry can exert certain influences on the measurement results, and considering the inherent discrepancies in the evaluation of breakdown fields, the data listed in the table are presented for reference and comparison only.

4.4 From Bulk Ceramics to Multilayer Ceramic Capacitors (MLCCs)

Although bulk BNT-based ceramics demonstrate exceptional energy storage performance in laboratory environments, their considerable specimen thickness mandates prohibitively high absolute operating voltages to achieve the target electric field. Consequently, they fail to satisfy the stringent industrial demands for miniaturization and integration in advanced electronic devices. Multilayer ceramic capacitors (MLCCs) facilitate the realization of elevated operating electric fields at

reduced applied voltages through the interleaving of ultrathin dielectric layers (typically with individual layer thicknesses less than 10 μm) and internal electrodes in a parallel configuration. However, the structural transition from bulk ceramics to multilayer devices introduces complex size effects, interfacial effects, and significant thickness-dependent E_b challenges. Moreover, to reduce commercialization costs, MLCCs often require the use of base metal electrodes, which necessitates high-temperature co-firing in a reducing atmosphere. This processing condition readily generates high concentrations of oxygen vacancy defects within the thin dielectric layers, and under extreme electric fields, it induces space charge migration, leading to deteriorated leakage current or even thermal breakdown.

To address the thermal effects induced by energy loss, which can lead to performance degradation, device aging, and even catastrophic failure in MLCCs due to Joule heating. Huang *et al.* [361] proposed a more rigorous dipole design strategy that simultaneously tailored both the spatial arrangement and interaction strength of polarization dipoles. In contrast to the intrinsically disordered heterogeneity of PNRs, in **Fig. 31** (a-b), the dynamic dipole engineering strategy offered distinct performance advantages by replacing random dipolar clusters with a discrete and spatially regulated dipole network. Specifically, multiple relaxor agents were introduced into a long-range ordered ferroelectric matrix to reconstruct dipole interactions and reduce energy loss during domain switching. The composition consisted of BNT-BKT providing ferroelectricity, the paraelectric ST diluting ferroelectric domains, and the relaxor agent $Bi(Mg_{2/3}Ta_{1/3})O_3$ (BMT). As shown in **Fig. 31**(c), the 0.6BNKT-0.4(0.7ST-0.3BMT)

achieved a high E_b of 650 kV/cm while delivering an astonishing η of 98.5% and a W_{rec} of approximately 16.2 J/cm^3. Based on the design concept of reducing Joule heat generation during energy conversion, MLCCs achieved excellent stability over a broad temperature span from 30°C to 180°C in thermal stability tests. This strategy also offers inspiration for the design of conventional bulk ceramics: reducing energy loss during domain switching not only enhances efficiency but also improves the resistance to thermal breakdown, thereby elevating the E_b.

Interestingly, Zhai *et al.* [362] fabricated a lead-free relaxor ferroelectric ceramic capacitor with the composition $(Bi_{0.5}Na_{0.5})_{0.65}(Sr_{0.7}Bi_{0.2})_{0.35}Ti_{1-x}Hf_xO_3$, realizing both ultrahigh E_b and excellent η. Specifically, the researchers employed the paraelectric $Sr_{0.7}Bi_{0.2}TiO_3$ to modify the BNT ceramic, constructing a polymorphic relaxor ferroelectric matrix. **Fig. 31**(e) shows the modeling of the dual-phase structure in the material. Doping the B-site with larger-radius Hf^{4+} ions lowered the *t*, which facilitated the precipitation of plate-like pyrochlore $Bi_2Ti_2O_7$ embedded within the perovskite host. The sheet-like pyrochlore phase effectively suppresses the electric-field propagation and hinders charge trapping, thereby significantly enhancing the breakdown strength (E_b=1150kV/cm). Simultaneously, the intrinsic switching field generated by the pyrochlore phase promotes overall polarization reversal, which further improves the energy-storage efficiency of the composite. Moreover, the introduction of large-radius Hf^{4+} ions expands the polarization displacement space and establishes a novel coupled polarization mode, contributing to the preservation of high polarization characteristics in the perovskite phase. Based on the calculation from the hysteresis loop, as shown in

Fig. 31 (e), a higher W_{rec} of 14.9 J/cm^3 was attained. In addition, it was found from **Fig. 31** (g) that the device efficiency showed no degradation after multiple cycling tests, thereby fulfilling cycling requirements for practical applications.

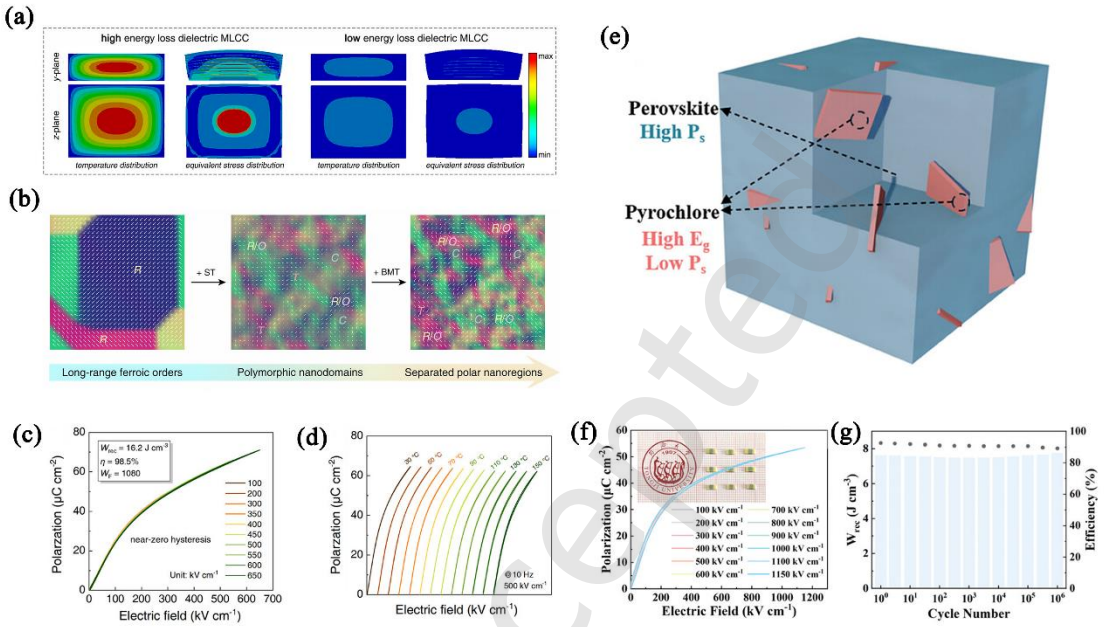

Fig. 31 (a) Finite element simulation of temperature and equivalent stress distributions in high/low-loss MLCCs under working states. (b) Structural evolution from long-range ferroelectric orders to polymorphic nanodomains and separated PNRs. (c) Near-zero hysteresis *P-E* loop of the optimized material at 650 kV/cm. (d) Unipolar *P-E* loops at 500 kV/cm under various testing temperatures (30℃-150℃). Reproduced with permission from Ref [361] Copyright © 2026 Wiley-VCH GmbH (e) Schematic of the microscopic heterostructure featuring plate-like pyrochlore secondary phase embedded in the perovskite matrix. (f) Unipolar *P-E* loops of the composite ceramics under different electric fields up to 1150 kV/cm. (g) Fatigue characteristics of energy storage density and efficiency under 10^6 high-field cycles. Reproduced with permission from Ref [362] Copyright © 2026 Wiley-VCH GmbH

5 Summary, Challenge, and Perspectives

Nowadays, dielectric capacitors have been widely applied in numerous electric fields, including electronic devices, power transmission systems, aerospace, and advanced weaponry. Although traditional lead-based capacitors have demonstrated excellent energy storage performance under low electric fields, their environmental contamination contradicts the principles of sustainable development. Therefore, developing new lead-free relaxor ferroelectric energy storage ceramics has become an important and urgent research topic. Among various lead-free material systems, BNT-based relaxor ferroelectric ceramics, owing to their outstanding performance and environmentally friendly nature, have emerged as one of the most promising candidates to replace lead-based capacitors.

This review systematically summarizes advancements in energy storage performance of BNT-based lead-free relaxor ferroelectric ceramics from the viewpoint of multiscale design strategies under low *E*-fields, moderate *E*-fields, and high *E*-fields according to different application scenarios. Studies have shown that through phase structure engineering (e.g., constructing pseudo-cubic phases or polymorphic phase boundaries), domain structure engineering (inducing PNRs and refining domain sizes), and defect engineering (regulating oxygen vacancy concentration and A-site ionic defects), the maximum polarization intensity of BNT-based ceramics can be effectively enhanced under low *E*-fields, while the P_r can be significantly reduced, resulting in slim polarization hysteresis loops. Under moderate to high electric fields, strategies such as grain refinement, interface engineering, and the construction of core-shell/sandwich

structures or composite phase macrostructures can synergistically optimize the polarization response and E_b of the material. For example, by constructing a dual-phase composite structure and leveraging the synergy between a high-entropy phase and the matrix phase, a remarkable W_{rec} of 23.6 J/cm^3 was achieved under an ultrahigh E_b of 990 kV/cm. Similarly, introducing a pyrochlore phase can increase the E_b of BNT-based MLCCs to 1150 kV/cm. These examples demonstrate that breakthroughs in energy storage performance under different electric fields primarily stem from precise control of the material's microstructure. Through multiscale structural engineering, the inherent trade-offs among high polarization intensity, high E_b, and high η can be effectively balanced.

Despite significant progress in microstructural regulation, a deeper understanding of the structure–performance relationship still faces numerous challenges. BNT-based ceramics exhibit complex phase transition behaviors (e.g., coexistence of rhombohedral, tetragonal, and antiferroelectric phases), while the dynamic evolution mechanisms of PNRs and defects under electric fields remain unclear. There is an urgent need to employ advanced characterization techniques, such as in situ electron microscopy and synchrotron radiation, to observe real-time interfacial structural evolution and PNRs dynamics driven by external fields. While notable progress has been achieved in multiscale structural regulation, the intricate coupling mechanisms across multiphase heterointerfaces remain inadequately understood, and systematic theoretical models for guiding the rational design of heterogeneous architectures are still lacking. Moreover, it is experimentally challenging to achieve precise control over phase distribution and

interfacial states. Additionally, current first-principles calculations struggle to accurately simulate the complex defect and interface effects in practical materials, while mesoscale phase-field simulations remain highly dependent on experimental data for parameterization, limiting their predictive and design capabilities.

Future progress relies on integrating in-depth mechanistic research with innovative preparation techniques. On the one hand, it is essential to combine multiscale computational simulations (such as first-principles and phase-field methods) with in situ high-resolution characterization techniques to reveal the dynamic evolution of material microstructures under external fields. Moreover, data-driven approaches like machine learning should be employed to establish accurate predictive models linking composition, structure, and macroscopic properties, thereby accelerating the rational design of new material systems.

Despite notable advancements in lead-free energy storage ceramics at the laboratory scale, a substantial disparity persists between fundamental research and full-scale industrial implementation. Future research should focus on the following key areas: First, regarding the transition to multilayer ceramic capacitor (MLCC) devices, the scale-up capability and the effective control of large-scale fabrication and sintering conditions must be addressed. Second, to reduce commercial costs, compatibility with base metal electrodes (BMEs like Ni or Cu) through co-firing is essential. Given the propensity of bismuth in BNT-based systems to undergo reduction under reductive atmospheres or exhibit diffusion and undesirable chemical interactions during high-temperature sintering, the development of low-reducibility or low-firing dielectric

ceramics is imperative for ensuring commercial viability. Furthermore, we must thoroughly study the long-term performance, insulation resistance, and fatigue failure mechanisms under coupled electric, thermal, mechanical, and humid conditions. This is necessary to guarantee high reliability. Finally, current evaluations based on low-frequency (typically 100 Hz) polarization loops deviate from practical operating conditions, such as high-frequency fields under large DC-bias with AC superpositions. Therefore, establishing standardized application measurement and evaluation criteria is highly necessary for the future development of dielectric capacitors in energy storage fields. Through cross-scale collaborative design and optimization, BNT-based lead-free dielectric ceramics are expected to play a crucial role in next-generation high-power pulse electronic systems.

Acknowledgments

The study was financially supported by the National Natural Science Foundation of China (No. 52202136, 52562019), the Natural Science Foundation of Jiangxi Province (No. 20232BAB204017).

Declaration of Competing Interest

The authors declare that they have no known competing financial interests or personal relationships that could have appeared to influence the work reported in this paper.

References

[1] Pan H, Lan S, Xu S, et al. Ultrahigh energy storage in superparaelectric relaxor ferroelectrics. *Science* 2021, **374:** 100-104.

[2] Yang L, Kong X, Li F, et al. Perovskite lead-free dielectrics for energy storage applications. *Prog Mater Sci* 2019, **102:** 72-108.

[3] Tong Y, Liang J, Liu H K, et al. Energy storage in Oceania. *Energy Storage Mater* 2019, **20:** 176-187.

[4] Wang G, Lu Z, Li Y, et al. Electroceramics for High-Energy Density Capacitors: Current Status and Future Perspectives. *Chem Rev* 2021, **121:** 6124-6172.

[5] Wang Y, Song Y, Xia Y Electrochemical capacitors: mechanism, materials, systems, characterization and applications. *Chem Soc Rev* 2016, **45:** 5925-5950.

[6] Yan F, Qian J, Wang S, et al. Progress and outlook on lead-free ceramics for energy storage applications. *Nano Energ* 2024, **123:** 109394.

[7] Fan X, Wang J, Yuan H, et al. Multi-scale synergic optimization strategy for dielectric energy storage ceramics. *J Adv Ceram* 2023, **12:** 649-680.

[8] Li D, Zeng X, Li Z, et al. Progress and perspectives in dielectric energy storage ceramics. *J Adv Ceram* 2021, **10:** 675-703.

[9] Shi W, Zhang L, Jing R, et al. Moderate fields, maximum potential: achieving high records with temperature-stable energy storage in lead-free BNT-based ceramics. *Nano-Micro Lett* 2024, **16:** 91.

[10] Hao X, et al. A review on the dielectric materials for high energy-storage application. *J Adv Dielectr* 2013, **03:** 1330001.

[11] Yang Z, Du H, Jin L, et al. High-performance lead-free bulk ceramics for electrical

energy storage applications: design strategies and challenges. *J Mater Chem A* 2021, **9:** 18026-18085.

[12] Dai S, Li M, Wu X, et al. Combinatorial optimization of perovskite-based ferroelectric ceramics for energy storage applications. *J Adv Ceram* 2024, **13:** 877-910.

[13] Lu X, Zou X, Shen J, et al. High energy density with ultrahigh discharging efficiency obtained in ceramic-polymer nanocomposites using a non-ferroelectric polar polymer as matrix. *Nano Energ* 2020, **70:** 104551.

[14] Zhang C, et al. Advancing with dipolar glass polymers. *Nat Energy* 2023, **8:** 220-220.

[15] Raegen A N, Yin J, Zhou Q, et al. Ultrastable monodisperse polymer glass formed by physical vapour deposition. *Nat Mater* 2020, **19:** 1110-1113.

[16] Li C, Zhang K, Cheng X, et al. Polymers for flexible energy storage devices. *Prog Poly Sci* 2023, **143:** 101714.

[17] Dong X, Zhao Q, Li Y, et al. Fabrication and high temperature electrical conductivity of polymer-derived SiHfBCN ceramic coating. *Journal of Adv Ceram* 2025, **14:** 9221011.

[18] Ren Z, Shi Z, Tang Q, et al. Core-shell TiO_2@Au Nanofibers Derived from a Unique Physical Coating Strategy for Excellent Capacitive Energy Storage Nanocomposites. *Adv Funct Mater* 2024, **34:** 2401907.

[19] Dou L, Yang B, Lan S, et al. Nanonet-/fiber-structured flexible ceramic membrane enabling dielectric energy storage. *J Adv Ceram* 2023, **12:** 145-154.

[20] Jin Z, Su B, Wu S, et al. Tribocatalytic recycling of lithium-ion batteries. *J Adv Ceram* 2025, **14:** 9221121.

[21] Li Q, Yao F-Z, Liu Y, et al. High-temperature dielectric materials for electrical energy storage. *Ann Rev Mater Res* 2018, **48:** 219-243.

[22] Li Q, Chen L, Gadinski M R, et al. Correction: Corrigendum: Flexible high-temperature dielectric materials from polymer nanocomposites. *Nature* 2016, **536:** 112-112.

[23] Tang Y D, Xu W H, Niu S, et al. Crosslinked dielectric materials for high-

temperature capacitive energy storage. *J Mater Chem A* 2021, **9:** 10000-10011.

[24] Palneedi H, Peddigari M, Hwang G T, et al. High-Performance Dielectric Ceramic Films for Energy Storage Capacitors: Progress and Outlook. *Adv Funct Mater* 2018, **28:** 33.

[25] Wang Q, Wang T, Chen L, et al. Designing high dielectric breakdown strategy for high-temperature capacitive energy storage and filtering performance via carrier trap mechanism. *Journal of Adv Ceram* 2025, **14:** 9221103.

[26] Zubairi H, Lu Z, Zhu Y, et al. Current development, optimisation strategies and future perspectives for lead-free dielectric ceramics in high field and high energy density capacitors. *Chem Soc Rev* 2024, **53:** 10761-10790.

[27] Xie J, Yao M, Gao W, et al. Significantly enhanced dielectric constant and energy density in Au/Al_2O_3 nanocomposite thin films. *J Alloys Compd* 2019, **772:** 324-331.

[28] Spahr H, Nowak C, Hirschberg F, et al. Enhancement of the maximum energy density in atomic layer deposited oxide based thin film capacitors. *Appl Phys Lett* 2013, **103:**

[29] Lin M, Zhuo J, Huang S, et al. Sandwich-structured polymer dielectrics exhibiting significantly improved capacitive performance at high temperatures by roll-to-roll physical vapor deposition. *Chemical Engineering Journal* 2024, **498:** 155586.

[30] Song L N, Myers A C, Adams J J, et al. Stretchable and reversibly deformable radio frequency antennas based on silver nanowires. *ACS Appl Mater Interfaces* 2014, **6:** 4248-4253.

[31] Zhang X, Sun S, Yin C, et al. Giant recoverable energy storage density for lead-free SrTiO3-based dielectric films coated by the amorphous Al2O3 insulating layers. *Journal of Adv Ceram* 2025, **14:** 9221175.

[32] He R, Guo H, Yao Z, et al. Negligible-hysteresis piezoceramic achieved by multiphase assisting and domain configuration manipulating. *Journal of Adv Ceram* 2025, **14:** 9221160.

[33] Xu L-Y, Ouyang J, Cheng Z-X, et al. A Review on the Dielectric Ceramics for High Energy-Storage Application. *Adv Ceram* 2025, **46:** 195-246.

[34] Haertling G H Ferroelectric Ceramics: History and Technology. *J Am Ceram Soc* 1999, **82:** 797-818.

[35] Acosta M, Novak N, Rojas V, et al. $BaTiO_3$-based piezoelectrics: Fundamentals, current status, and perspectives. *Appl Phys Rev* 2017, **4:** 041305.

[36] Wang C, Lou X High energy storage properties of $0.94Bi_{0.5}Na_{0.5}TiO_3$-$0.06BaTiO_3$ ceramics by incorporating $Sr_{0.8}Bi_{0.1\gamma0.1}Ti_{0.8}Zr_{0.2}O_{2.95}$. *Microstructures* 2023, **3:** 2023023.

[37] Jayakrishnan A R, Silva J P B, Kamakshi K, et al. Are lead-free relaxor ferroelectric materials the most promising candidates for energy storage capacitors? *Prog Mater Sci* 2023, **132:** 101046.

[38] Huang X, Sun B, Zhu Y, et al. High-k polymer nanocomposites with 1D filler for dielectric and energy storage applications. *Prog Mater Sci* 2019, **100:** 187-225.

[39] Hao X, Zhai J, Kong L B, et al. A comprehensive review on the progress of lead zirconate-based antiferroelectric materials. *Prog Mater Sci* 2014, **63:** 1-57.

[40] Liu Z, Lu T, Ye J, et al. Antiferroelectrics for energy storage applications: a review. *Adv Mater Technol.* 2018, **3:** 1800111.

[41] Zhang S, Malič B, Li J-F, et al. Lead-free ferroelectric materials: Prospective applications. *J Mater Res* 2021, **36:** 985-995.

[42] Pan H, Ma J, Ma J, et al. Giant energy density and high efficiency achieved in bismuth ferrite-based film capacitors via domain engineering. *Nat Commun* 2018, **9:** 1813.

[43] Pan H, Li F, Liu Y, et al. Ultrahigh–energy density lead-free dielectric films via polymorphic nanodomain design. *Science* 2019, **365:** 578-582.

[44] Li J, Jin L, Tian Y, et al. Enhanced energy storage performance under low electric field in Sm^{3+} doped $AgNbO_3$ ceramics. *J Materiomics* 2022, **8:** 266-273.

[45] Li F, Zhou M, Zhai J, et al. Novel barium titanate based ferroelectric relaxor ceramics with superior charge-discharge performance. *J Eur Ceram Soc* 2018, **38:** 4646-4652.

[46] Wang T, Jin L, Li C, et al. Relaxor ferroelectric $BaTiO_3$–$Bi(Mg_{2/3}Nb_{1/3})O_3$ ceramics for energy storage application. *J Am Ceram Soc* 2015, **98:** 559-566.

[47] Yuan Q, Li G, Yao F-Z, et al. Simultaneously achieved temperature-insensitive high energy density and efficiency in domain engineered $BaTiO_3$-$Bi(Mg_{0.5}Zr_{0.5})O_3$ lead-free relaxor ferroelectrics. *Nano Energ* 2018, **52:** 203-210.

[48] Chen X, Li X, Sun J, et al. Achieving ultrahigh energy storage density and energy efficiency simultaneously in barium titanate based ceramics. *Appl Phys A* 2020, **126:** 146.

[49] Si F, Tang B, Fang Z, et al. A new type of $BaTiO_3$-based ceramics with $Bi(Mg_{1/2}Sn_{1/2})O_3$ modification showing improved energy storage properties and pulsed discharging performances. *J Alloys Compd* 2020, **819:** 153004.

[50] Yang H, Lu Z, Li L, et al. Novel $BaTiO_3$-Based, Ag/Pd-Compatible Lead-Free relaxors with superior energy storage performance. *ACS Appl Mater Interfaces* 2020, **12:** 43942-43949.

[51] Li W B, Zhou D, Pang L X, et al. Novel barium titanate based capacitors with high energy density and fast discharge performance. *J Mater Chem A* 2017, **5:** 19607-19612.

[52] Li X, Chen X, Sun J, et al. Novel lead-free ceramic capacitors with high energy density and fast discharge performance. *Ceram Int* 2020, **46:** 3426-3432.

[53] Li W-B, Zhou D, Xu R, et al. $BaTiO_3$–$Bi(Li_{0.5}Ta_{0.5})O_3$, lead-free ceramics, and multilayers with high energy storage density and efficiency. *ACS Appl Energy Mater* 2018, **1:** 5016-5023.

[54] Si F, Tang B, Fang Z, et al. Enhanced energy storage and fast charge-discharge properties of (1-x)$BaTiO_3$-x$Bi(Ni_{1/2}Sn_{1/2})O_3$ relaxor ferroelectric ceramics. *Ceram Int* 2019, **45:** 17580-17590.

[55] Lin Y, Li D, Zhang M, et al. Excellent energy-storage properties achieved in $BaTiO_3$-based lead-free relaxor ferroelectric ceramics via domain engineering on the nanoscale. *ACS Appl Mater Interfaces* 2019, **11:** 36824-36830.

[56] Yang H, Yan F, Lin Y, et al. A lead free relaxation and high energy storage efficiency ceramics for energy storage applications. *J Alloys Compd* 2017, **710:** 436-445.

[57] Dong X, Chen X, Chen H, et al. Simultaneously achieved high energy-storage

density and efficiency in $BaTiO_3$–$Bi(Ni_{2/3}Ta_{1/3})O_3$ lead-free relaxor ferroelectrics. *J Mater Sci: Mater Electron* 2020, **31:** 22780-22788.

[58] Li Y, Tang M-Y, Zhang Z-G, et al. $BaTiO_3$-based ceramics with high energy storage density. *Rare Met* 2023, **42:** 1261-1273.

[59] Kong X, Yang L, Meng F, et al. High-entropy engineered $BaTiO_3$-based ceramic capacitors with greatly enhanced high-temperature energy storage performance. *Nat Commun* 2025, **16:** 885.

[60] Wang C, Cao W, Liang C, et al. Ultrahigh energy-storage density of $BaTiO_3$-Based ceramics via the interfacial polarization strategy. *ACS Appl Mater Interfaces* 2023, **15:** 42774-42783.

[61] Qi J, Zhang M, Chen Y, et al. High-entropy assisted $BaTiO_3$-based ceramic capacitors for energy storage. *Cell Rep Phys Sci* 2022, **3:** 101110.

[62] Ouyang J, Xue Y, Song C, et al. Simultaneously achieving high energy density and responsivity in submicron BaTiO3 film capacitors integrated on Si. *J Adv Ceram* 2024, **13:** 198-206.

[63] Yan F, Yang H B, Ying L, et al. Enhanced energy storage properties of a novel lead-free ceramic with a multilayer structure. *J Mater Chem C* 2018, **6:** 7905-7912.

[64] Cui C, Pu Y, Gao Z, et al. Structure, dielectric and relaxor properties in lead-free ST-NBT ceramics for high energy storage applications. *J Alloys Compd* 2017, **711:** 319-326.

[65] Wang C, Yan F, Yang H B, et al. Dielectric and ferroelectric properties of $SrTiO_3$-$Bi_{0.54}Na_{0.46}TiO_3$-$BaTiO_3$ lead-free ceramics for high energy storage applications. *J Alloys Compd* 2018, **749:** 605-611.

[66] Yang H, Yan F, Lin Y, et al. Enhanced recoverable energy storage density and high efficiency of $SrTiO_3$-based lead-free ceramics. *Appl Phys Lett* 2017, **111:** 253903.

[67] Jan A, Liu H, Hao H, et al. Enhanced dielectric breakdown strength and ultra-fast discharge performance of novel $SrTiO_3$ based ceramics system. *J Alloys Compd* 2020, **830:** 154611.

[68] Cui C, Pu Y, Shi R High-energy storage performance in lead-free (0.8-x)$SrTiO_3$-0.2$Na_{0.5}Bi_{0.5}TiO_3$-x$BaTiO_3$ relaxor ferroelectric ceramics. *J Alloys Compd* 2018,

740: 1180-1187.

[69] Yang H, Yan F, Lin Y, et al. Improvement of dielectric and energy storage properties in $SrTiO_3$-based lead-free ceramics. *J Alloys Compd* 2017, **728:** 780-787.

[70] Kong X, Yang L T, Cheng Z X, et al. Bi-modified $SrTiO_3$-based ceramics for high-temperature energy storage applications. *J Am Ceram Soc* 2020, **103:** 1722-1731.

[71] Yang H B, Yan F, Lin Y, et al. Novel strontium titanate-based lead-free ceramics for high-energy storage applications. *ACS Sustainable Chem Eng* 2017, **5:** 10215-10222.

[72] Li L, Yu X, Cai H, et al. Preparation and dielectric properties of $BaCu(B_2O_5)$-doped $SrTiO_3$-based ceramics for energy storage. *J Mater Sci Eng B* 2013, **178:** 1509-1514.

[73] Zhao G H, Li Y Q, Liu H X, et al. Effect of SiO_2 additives on the microstructure and energy storage density of $SrTiO_3$ ceramics. *J Ceram Process Res* 2012, **13:** 310-314.

[74] Zuo C, Xu J, Yang S, et al. Superior energy storage properties in $SrTiO_3$-based dielectric ceramics through all-scale hierarchical architecture. *Mater Horiz* 2024, **11:** 1732-1740.

[75] Liu L, Liu Y, Hao J, et al. Multi-scale collaborative optimization of $SrTiO_3$-based energy storage ceramics with high performance and excellent stability. *Nano Energ* 2023, **109:** 108275.

[76] Zhou H Y, Zhu X N, Ren G R, et al. Enhanced energy storage density and its variation tendency in $CaZr_xTi_{1-x}O3$ ceramics. *J Alloys Compd* 2016, **688:** 687-691.

[77] Zhou H Y, Liu X Q, Zhu X L, et al. $CaTiO_3$ linear dielectric ceramics with greatly enhanced dielectric strength and energy storage density. *J Am Ceram Soc* 2018, **101:** 1999-2008.

[78] Yang L, Song L, Li Q, et al. Dielectric properties and electrical response of yttrium-doped Bi2/3Cu3Ti4O12 ceramics. *J Adv Dielectr* 2021, **11:** 2150007.

[79] Guo Q, Dai Z, Liu C, et al. High-efficiency lead-free BNT-CTT perovskite energy storage ceramics under high electric field. *J Energy Storage* 2024, **102:** 114154.

[80] Bian J J, Otonicar M, Spreitzer M, et al. Structural evolution, dielectric and energy storage properties of $Na(Nb_{1-x}Ta_x)O_3$ ceramics prepared by spark plasma sintering. *J Eur Ceram Soc* 2019, **39:** 2339-2347.

[81] Qi H, Zuo R, Xie A, et al. Excellent energy-storage properties of $NaNbO_3$-based lead-free antiferroelectric orthorhombic P-phase (Pbma) ceramics with repeatable double polarization-field loops. *J Eur Ceram Soc* 2019, **39:** 3703-3709.

[82] Yang Z, Du H, Jin L, et al. A new family of sodium niobate-based dielectrics for electrical energy storage applications. *J Eur Ceram Soc* 2019, **39:** 2899-2907.

[83] Zhou M X, Liang R H, Zhou Z Y, et al. Superior energy storage properties and excellent stability of novel $NaNbO_3$-based lead-free ceramics with A-site vacancy obtained via a Bi_2O_3 substitution strategy. *J Mater Chem A* 2018, **6:** 17896-17904.

[84] Zhou M X, Liang R H, Zhou Z Y, et al. Novel sodium niobate-based lead-free ceramics as new environment-friendly energy storage materials with high energy density, high power density, and excellent stability. *ACS Sustainable Chem Eng* 2018, **6:** 12755-12765.

[85] Qu N, Du H L, Hao X H A new strategy to realize high comprehensive energy storage properties in lead-free bulk ceramics. *J Mater Chem C* 2019, **7:** 7993-8002.

[86] Ye J M, Wang G S, Zhou M X, et al. Excellent comprehensive energy storage properties of novel lead-free $NaNbO_3$-based ceramics for dielectric capacitor applications. *J Mater Chem C* 2019, **7:** 5639-5645.

[87] Tian A, Zuo R Z, Qi H, et al. Large energy-storage density in transition-metal oxide modified $NaNbO_3$-$Bi(Mg_{0.5}Ti_{0.5})O_3$ lead-free ceramics through regulating the antiferroelectric phase structure. *J Mater Chem A* 2020, **8:** 8352-8359.

[88] Yang Z T, Du H L, Jin L, et al. Realizing high comprehensive energy storage performance in lead-free bulk ceramics via designing an unmatched temperature range. *J Mater Chem A* 2019, **7:** 27256-27266.

[89] Qi H, Zuo R, Xie A, et al. Ultrahigh Energy-Storage Density in $NaNbO_3$-Based Lead-Free Relaxor Antiferroelectric Ceramics with Nanoscale Domains. *Adv Funct Mater* 2019, **29:** 1903877.

[90] Shi J P, Chen X L, Li X, et al. Realizing ultrahigh recoverable energy density and

superior charge-discharge performance in $NaNbO_3$-based lead-free ceramics via a local random field strategy. *J Mater Chem C* 2020, **8:** 3784-3794.

[91] Wang M, Feng Q, Luo C Y, et al. Ultrahigh energy storage density and efficiency in $Bi_{0.5}Na_{0.5}TiO_3$-based ceramics via the domain and bandgap engineering. *ACS Appl Mater Interfaces* 2021, **13:** 51218-51229.

[92] Chen H Y, Shi J P, Chen X L, et al. Excellent energy storage properties and stability of $NaNbO_3$-$Bi(Mg_{0.5}Ta_{0.5})O_3$ ceramics by introducing $(Bi_{0.5}Na_{0.5})_{0.7}Sr_{0.3}TiO_3$. *J Mater Chem A* 2021, **9:** 4789-4799.

[93] Lv Z, Lu T, Liu Z, et al. $NaNbO_3$-Based multilayer ceramic capacitors with ultrahigh energy storage performance. *Adv Energy Mater* 2024, **14:** 2304291.

[94] Xu M, Pan Y, Dong Q, et al. High energy storage performance obtained by adjusting the polarization ability of $NaNbO_3$ based ceramics. *J Power Sources* 2025, **630:** 235923.

[95] Zhang Y, Xie A, Tian A, et al. Superior multilayer ceramic energy-storage capacitors using $NaNbO_3$-based relaxor ferroelectrics with heterogeneous nanodomains. *Chem Eng J* 2025, **507:** 160821.

[96] Ge G, Qian J, Xu K, et al. Excellent Energy Storage Performance of Polymorphic Modulated Antiferroelectric Lead Zirconate Ceramic. *Adv Mater* 2025, **37:** 2505731.

[97] Tian Y, Jin L, Zhang H F, et al. High energy density in silver niobate ceramics. *J Mater Chem A* 2016, **4:** 17279-17287.

[98] Tian Y, Jin L, Zhang H F, et al. Phase transitions in bismuth-modified silver niobate ceramics for high power energy storage. *J Mater Chem A* 2017, **5:** 17525-17531.

[99] Zhao L, Liu Q, Gao J, et al. Lead-free antiferroelectric silver niobate tantalate with high energy storage performance. *Adv Mater* 2017, **29:** 7.

[100] Gao J, Zhang Y C, Zhao L, et al. Enhanced antiferroelectric phase stability in La-doped $AgNbO_3$: perspectives from the microstructure to energy storage properties. *J Mater Chem A* 2019, **7:** 2225-2232.

[101] Lu Z, Bao W, Wang G, et al. Mechanism of enhanced energy storage density in $AgNbO_3$-based lead-free antiferroelectrics. *Nano Energ* 2021, **79:** 105423.

[102] Luo N, Han K, Cabral M J, et al. Constructing phase boundary in $AgNbO_3$ antiferroelectrics: pathway simultaneously achieving high energy density and efficiency. *Nat Commun* 2020, **11:** 4824.

[103] Gao S, Huang Y, Jiang Y, et al. Ultrahigh energy density and excellent discharge properties in Ce^{4+} and Ta^{5+} co-modified $AgNbO_3$ relaxor antiferroelectric ceramics via multiple design strategies. *Acta Mater* 2023, **246:** 118730.

[104] Zhao M-Y, Wang J, Chen L, et al. Enhanced breakdown strength and energy storage density of $AgNbO_3$ ceramics via tape casting. *Rare Met* 2023, **42:** 495-502.

[105] Zhao M, Shen X, Wang J, et al. Superior comprehensive energy storage performances in Eu-doped $AgNbO_3$ antiferroelectric ceramics. *Chem Eng J* 2023, **478:** 147527.

[106] Tian T-F, Chen F-L, Zhang L-B, et al. Advances in Energy Storage of $AgNbO_3$-based Antiferroelectric Ceramics. *Adv Ceram* 2023, **44:** 153-172.

[107] Hu Z, Liu Z, Han B, et al. Designing silver niobate-based relaxor antiferroelectrics for ultrahigh energy storage performance. *J Adv Ceram* 2024, **13:** 1282-1290.

[108] Wang T, Jin L, Tian Y, et al. Microstructure and ferroelectric properties of Nb_2O_5-modified $BiFeO_3$-$BaTiO_3$ lead-free ceramics for energy storage. *Mater Lett* 2014, **137:** 79-81.

[109] Zheng D, Zuo R, Zhang D, et al. Novel $BiFeO_3$–$BaTiO_3$–$Ba(Mg_{1/3}Nb_{2/3})O_3$ lead-free relaxor ferroelectric ceramics for energy-storage capacitors. *J Am Ceram Soc* 2015, **98:** 2692-2695.

[110] Zheng D, Zuo R Enhanced energy storage properties in $La(Mg_{1/2}Ti_{1/2})O_3$-modified $BiFeO_3$-$BaTiO_3$ lead-free relaxor ferroelectric ceramics within a wide temperature range. *J Eur Ceram Soc* 2017, **37:** 413-418.

[111] Gao X, Li Y, Chen J, et al. High energy storage performances of $Bi_{1-x}Sm_xFe_{0.95}Sc_{0.05}O_3$ lead-free ceramics synthesized by rapid hot press sintering. *J Eur Ceram Soc* 2019, **39:** 2331-2338.

[112] Chen Z, Bai X, Wang H, et al. Achieving high-energy storage performance in $0.67Bi_{1-x}Sm_xFeO_3$-$0.33BaTiO_3$ lead-free relaxor ferroelectric ceramics. *Ceram Int*

2020, **46:** 11549-11555.

[113] Qi H, Xie A, Tian A, et al. Superior energy-storage capacitors with simultaneously giant energy density and efficiency using nanodomain engineered $BiFeO_3$-$BaTiO_3$-$NaNbO_3$ lead-free bulk ferroelectrics. *Adv Energy Mater* 2020, **10:** 1903338.

[114] Zhao J H, Hu T F, Fu Z Q, et al. Delayed polarization saturation induced superior energy storage capability of $BiFeO_3$-based ceramics via Introduction of non-isovalent ions. *Small* 2023, **19:** 9.

[115] Kang F, Zhang L, Yang W, et al. Achieving ultrahigh energy storage performance in $BiFeO_3$-$BaTiO_3$ based lead free relaxors via a composition optimization strategy. *J Eur Ceram Soc* 2022, **42:** 6958-6967.

[116] Zhou Z, Bai W, Liu N, et al. Ultrahigh capacitive energy storage of BiFeO3-based ceramics through multi-oriented nanodomain construction. *Nat Commun* 2025, **16:** 2075.

[117] Zhao J, Li H, Du Y, et al. Superior energy storage performance of $BiFeO_3$–$BaTiO_3$–$CaHfO_3$ lead-free ceramics. *J Mater Chem A* 2024, **12:** 5261-5268.

[118] Zhou Z, Hu J, Lv L, et al. Enhanced energy storage density in $BiFeO_3$-Based ceramics via phase ratio modulation and microstructure engineering. *J Power Sources* 2025, **629:** 236023.

[119] Ye W, Zhu C, Xiao Y, et al. Remarkable energy-storage performances and excellent stability in $CaTiO_3$-doped $BiFeO_3$-$BaTiO_3$ relaxor ferroelectric ceramics. *J Eur Ceram Soc* 2023, **43:** 900-908.

[120] Zhou Z, Pan Z, Hu J, et al. Engineering nanocluster and pyrochlore phase in $BiFeO_3$-based ceramics for electrostatic energy storage. *Compos Part B Eng* 2024, **287:** 111829.

[121] Guo X, Pu Y, Wang W, et al. High Insulation Resistivity and Ultralow Dielectric Loss in La-Doped SrTiO3 Colossal Permittivity Ceramics through Defect Chemistry Optimization. *ACS Sustainable Chemistry & Engineering* 2019, **7:** 13041-13052.

[122] Yang Z, Gao F, Du H, et al. Grain size engineered lead-free ceramics with both

large energy storage density and ultrahigh mechanical properties. *Nano Energ* 2019, **58:** 768-777.

[123] Qu B Y, Du H L, Yang Z T Lead-free relaxor ferroelectric ceramics with high optical transparency and energy storage ability. *J Mater Chem C* 2016, **4:** 1795-1803.

[124] Shao T Q, Du H L, Ma H, et al. Potassium-sodium niobate based lead-free ceramics: novel electrical energy storage materials. *J Mater Chem A* 2017, **5:** 554-563.

[125] Du J H, Li Y, Sun N N, et al. Dielectric, ferroelectric and high energy storage behavior of (1-*x*)$K_{0.5}Na_{0.5}NbO_3$-*x*$Bi(Mg_{0.5}Ti_{0.5})O_3$ lead free relaxor ferroelectric ceramics. *Acta Phys Sin* 2020, **69:** 12.

[126] Yang Z T, Du H L, Qu S B, et al. Significantly enhanced recoverable energy storage density in potassium-sodium niobate-based lead free ceramics. *J Mater Chem A* 2016, **4:** 13778-13785.

[127] Zhang M, Yang H B, Li D, et al. Giant energy storage efficiency and high recoverable energy storage density achieved in $K_{0.5}Na_{0.5}NbO_3$-$Bi(Zn_{0.5}Zr_{0.5})O_3$ ceramics. *J Mater Chem C* 2020, **8:** 8777-8785.

[128] Li W, Hao J, Fu P, et al. Large electrostrictive effect and strong photoluminescence properties in Sm_2O_3-modified lead-free potassium sodium niobate-based piezoelectric ceramics. *J Materiomics* 2020, **6:** 768-780.

[129] Qu B Y, Du H L, Yang Z T, et al. Enhanced dielectric breakdown strength and energy storage density in lead-free relaxor ferroelectric ceramics prepared using transition liquid phase sintering. *RSC Adv* 2016, **6:** 34381-34389.

[130] Qu B, Du H, Yang Z, et al. Large recoverable energy storage density and low sintering temperature in potassium-sodium niobate-based ceramics for multilayer pulsed power capacitors. *J Am Ceram Soc* 2017, **100:** 1517-1526.

[131] Zhang Y, Zuo R Excellent energy-storage performances in La_2O_3 doped (Na,K)NbO_3-based lead-free relaxor ferroelectrics. *J Eur Ceram Soc* 2020, **40:** 5466-5474.

[132] Chai Q Z, Yang D, Zhao X M, et al. Lead-free (K,Na)NbO_3-based ceramics with

high optical transparency and large energy storage ability. *J Am Ceram Soc* 2018, **101:** 2321-2329.

[133] Zhang M, Yang H, Lin Y, et al. Significant increase in comprehensive energy storage performance of potassium sodium niobate-based ceramics via synergistic optimization strategy. *Energy Storage Mater* 2022, **45:** 861-868.

[134] Dai Z, Li D, Zhou Z, et al. A strategy for high performance of energy storage and transparency in KNN-based ferroelectric ceramics. *Chem Eng J* 2022, **427:** 131959.

[135] Chen Q, Mo M, Chen N, et al. Simultaneous improvement of energy storage characteristics and temperature stability in $K_{0.5}Na_{0.5}NbO_3$-based ceramics via LiF modification. *ACS Appl Mater Interfaces* 2024, **16:** 52487-52500.

[136] Gao T, Mo M, Chen N, et al. Enhanced comprehensive energy storage properties of lead-free KNN based ceramics through composition optimization strategy. *Chem Eng J* 2024, **500:** 157560.

[137] Bi W, Li Y, Tian G, et al. Energy storage properties, transmittance and hardness of Er doped $K_{0.5}Na_{0.5}NbO_3$-based ceramics. *J Eur Ceram Soc* 2025, **45:** 116851.

[138] Zha J, Liu J, Yang Y, et al. High energy storage performance of (1-x)$Ba_{0.5}Sr_{0.5}TiO_3$-x$K_{0.5}Na_{0.5}NbO_3$ ceramics via a combined strategy of fine grains and multiphase polar nanoregions. *Chem Eng J* 2024, **486:** 150441.

[139] Huan Y, Gui D, Li C, et al. Simultaneously enhanced energy storage performance and luminance resistance in $(K_{0.5}Na_{0.5})NbO_3$-based ceramics via synergistic optimization strategy. *J Adv Ceram* 2024, **13:** 34-43.

[140] Liu Y, Ji Y, Yang Y Growth, properties and applications of $Bi_{0.5}Na_{0.5}TiO_3$ ferroelectric nanomaterials. *Nanomaterials* 2021, **11:** 18.

[141] Zhu L Exploring strategies for high dielectric constant and low loss polymer dielectrics. *J Phys Chem Lett* 2014, **5:** 3677-3687.

[142] Shi P, Liu J, Song Y, et al. Significant improvement of energy storage density and efficiency of 0.72$Bi_{0.5}Na_{0.5}TiO_3$-0.28$SrTiO_3$ ceramics and study of the mechanism of high temperature energy storage performance. *Appl Phys Lett* 2025, **126:** 032901.

[143] Pan Y, Zhang Y, Dong Q, et al. Entropy-driven multi-scale enhancement of energy storage performance in $(Bi_{0.5}Na_{0.5})_{0.5}Ba_{0.5}TiO_3$ ceramics. *J Materiomics* 2025, 101055.

[144] Li P, Yang H, Yuan Q, et al. Enhanced energy storage performance of $Na_{0.5}Bi_{0.5}TiO_3$-based relaxor ferroelectric ceramics by synergistic optimization strategies. *Mater Today Phys* 2024, **43:** 101420.

[145] Spreitzer M, Valant M, Suvorov D Sodium deficiency in $Na_{0.5}Bi_{0.5}TiO_3$. *J Mater Chem* 2007, **17:** 185-192.

[146] Kang R, Wang Z, Yang W, et al. Enhanced energy storage performance in $Sr_{0.7}La_{0.2}Zr_{0.15}Ti_{0.85}O_3$-modified $Bi_{0.5}Na_{0.5}TiO_3$ ceramics via constructing local phase coexistence. *Chem Eng J* 2022, **446:** 137105.

[147] Zhou X, Xue G, Luo H, et al. Phase structure and properties of sodium bismuth titanate lead-free piezoelectric ceramics. *Prog Mater Sci* 2021, **122:** 100836.

[148] Xu Q, Li T, Hao H, et al. Enhanced energy storage properties of $NaNbO_3$ modified $Bi_{0.5}Na_{0.5}TiO_3$ based ceramics. *J Eur Ceram Soc* 2015, **35:** 545-553.

[149] Zhang Y, Zhang X, Zhang J, et al. Multi-scale domain enhanced energy storage performance in lead-free $Bi_{0.5}Na_{0.5}TiO_3$-based complex perovskites with low sintering temperature. *J Power Sources* 2025, **641:** 236845.

[150] Li W, Xu J, Chen J, et al. Boosting energy storage performance with lead-free relaxor ferroelectric in BNT-based ceramics via introducing scheelite La_2WTiO_8. *J Mater Chem A* 2024, **12:** 29044-29053.

[151] Wang Y, Dang S, Chai Q, et al. Superior energy storage performance in $Bi_{0.5}Na_{0.5}TiO_3$ based ceramics via synergistic design of multi-size domain construction and multiple phase structures. *Chem Eng J* 2024, **500:** 156460.

[152] Liu H, Sun Z, Zhang J, et al. Chemical design of Pb-free relaxors for giant capacitive energy storage. *Journal of the American Chemical Society* 2023, **145:** 11764-11772.

[153] Xiong X, Liu H, Zhang J, et al. Ultrahigh energy-storage in dual-phase relaxor ferroelectric ceramics. *Adv Mater* 2024, **36:** 2410088.

[154] Zhang Y, Liu P, Kandula K R, et al. Achieving excellent energy storage density

of $Pb_{0.97}La_{0.02}(Zr_xSn_{0.05}Ti_{0.95-x})O_3$ ceramics by the B-site modification. *J Eur Ceram Soc* 2021, **41:** 360-367.

[155] Lv L, Zhuo F, He C, et al. Achieving high energy storage performance of $Pb(Lu_{1/2}Nb_{1/2})O_3$ antiferroelectric ceramics via equivalent A-site engineering. *J Eur Ceram Soc* 2022, **42:** 5606-5614.

[156] Guo J, Yang T Giant energy storage density in Ba, La co-doped $PbHfO_3$-based antiferroelectric ceramics by a rolling process. *J Alloys Compd* 2021, **888:** 161539.

[157] Xu R, Xu Z, Feng Y, et al. Energy storage and release properties of Sr-doped (Pb,La)(Zr,Sn,Ti)O_3 antiferroelectric ceramics. *Ceram Int* 2016, **42:** 12875-12879.

[158] Liu Z, Bai Y, Chen X, et al. Linear composition-dependent phase transition behavior and energy storage performance of tetragonal PLZST antiferroelectric ceramics. *J Alloys Compd* 2017, **691:** 721-725.

[159] Wang X, Zhu Q, Sun H, et al. Ultrahigh energy storage density and efficiency in PLZST antiferroelectric ceramics via multiple optimization strategy. *J Eur Ceram Soc* 2023, **43:** 4051-4059.

[160] Wang H, Liu Y, Yang T, et al. Ultrahigh Energy-Storage Density in Antiferroelectric Ceramics with Field-Induced Multiphase Transitions. *Adv Funct Mater* 2019, **29:** 1807321.

[161] Sun Z, Wang Z, Tian Y, et al. Progress, outlook, and challenges in lead-free energy-storage ferroelectrics. *Adv. Electron. Mater.* 2020, **6:** 1900698.

[162] Jin L, Li F, Zhang S J Decoding the Fingerprint of Ferroelectric Loops: Comprehension of the Material Properties and Structures. *J Am Ceram Soc* 2014, **97:** 1-27.

[163] Ge G, Huang K, Wu S, et al. Synergistic optimization of antiferroelectric ceramics with superior energy storage properties via phase structure engineering. *Energy Storage Mater* 2021, **35:** 114-121.

[164] Li S, Hu T, Nie H, et al. Giant energy density and high efficiency achieved in silver niobate-based lead-free antiferroelectric ceramic capacitors via domain engineering. *Energy Storage Mater* 2021, **34:** 417-426.

[165] Wang L-M, Liu Q-X, Zhou D Dielectric and energy storage properties of the (1-

x)$BaTiO_3$-x$Bi(Li_{1/3}Hf_{2/3})O_3$ ($0.08 \leq x \leq 0.14$) ceramics. *Mater Lett* 2021, **283:** 128823.

[166] Lv J, Li Q, Li Y, et al. Significantly improved energy storage performance of NBT-BT based ceramics through domain control and preparation optimization. *Chem Eng J* 2021, **420:** 129900.

[167] Guo B, Yan Y, Tang M, et al. Energy storage performance of $Na_{0.5}Bi_{0.5}TiO_3$ based lead-free ferroelectric ceramics prepared via non-uniform phase structure modification and rolling process. *Chem Eng J* 2021, **420:** 130475.

[168] Liu J, Wang Y, Zhu H, et al. Synergically improved energy storage performance and stability in sol–gel processed $BaTiO_3$/(Pb,La,Ca)TiO_3/$BaTiO_3$ tri-layer films with a crystalline engineered sandwich structure. *J Adv Ceram* 2023, **12:** 2300-2314.

[169] Owate I O, Freer R ac breakdown characteristics of ceramic materials. *J. Appl. Phys.* 1992, **72:** 2418-2422.

[170] Tang L, Pan Z, Zhao J, et al. Nanoscale grain sizes in BNT-based ceramics with superb energy storage performances via coating boron nitride nanosheets. *Chem Eng J* 2023, **455:** 140524.

[171] Liu B, Wang X, Zhang R, et al. Grain size effect and microstructure influence on the energy storage properties of fine-grained $BaTiO_3$-based ceramics. *J Am Ceram Soc* 2017, **100:** 3599-3607.

[172] Neusel C, Jelitto H, Schmidt D, et al. Thickness-dependence of the breakdown strength: Analysis of the dielectric and mechanical failure. *J Eur Ceram Soc* 2015, **35:** 113-123.

[173] Messing G L, Stevenson A J Toward pore-free ceramics. *Science* 2008, **322:** 383-384.

[174] Ye H, Yang F, Pan Z, et al. Significantly improvement of comprehensive energy storage performances with lead-free relaxor ferroelectric ceramics for high-temperature capacitors applications. *Acta Mater* 2021, **203:** 116484.

[175] Liu N, Liang R, Zhao X, et al. Novel bismuth ferrite-based lead-free ceramics with high energy and power density. *J Am Ceram Soc* 2018, **101:** 3259-3265.

[176] Wang D W, Fan Z M, Li W B, et al. High energy storage density and large strain in $Bi(Zn_{2/3}Nb_{1/3})O_3$-doped $BiFeO_3$-$BaTiO_3$ ceramics. *ACS Appl Energy Mater* 2018, **1:** 4403-4412.

[177] Yang H, Qi H, Zuo R Enhanced breakdown strength and energy storage density in a new $BiFeO_3$-based ternary lead-free relaxor ferroelectric ceramic. *J Eur Ceram Soc* 2019, **39:** 2673-2679.

[178] Zhao C, Wu B, Wang K, et al. Practical high strain with superior temperature stability in lead-free piezoceramics through domain engineering. *J Mater Chem A* 2018, **6:** 23736-23745.

[179] Lv X, Zhang X-x, Wu J Nano-domains in lead-free piezoceramics: a review. *J Mater Chem A* 2020, **8:** 10026-10073.

[180] Chen L, Wang N, Zhang Z, et al. Local diverse polarization optimized comprehensive energy-storage performance in lead-free superparaelectrics. *Adv Mater* 2022, **34:** 2205787.

[181] Ghayour H, Abdellahi M A brief review of the effect of grain size variation on the electrical properties of BaTiO3-based ceramics. *Powder Technol* 2016, **292:** 84-93.

[182] Chattopadhyay S, Ayyub P, Palkar V R, et al. Size-induced diffuse phase transition in the nanocrystalline ferroelectric $PbTiO_3$. *Physical Review B* 1995, **52:** 13177-13183.

[183] Mudinepalli V R, Feng L, Lin W-C, et al. Effect of grain size on dielectric and ferroelectric properties of nanostructured $Ba_{0.8}Sr_{0.2}TiO_3$ ceramics. *J Adv Ceram* 2015, **4:** 46-53.

[184] Liu J S, Zhang S R, Zeng H Z, et al. Coercive field dependence of the grain size of ferroelectric films. *Physical Review B* 2005, **72:** 172101.

[185] Qin M, Zhang L, Wu H Dielectric loss mechanism in electromagnetic wave absorbing materials. *Adv. Sci.* 2022, **9:** 2105553.

[186] Glazunova E V, Shilkina L A, Chekhova A S, et al. Structure and dielectric properties of $(1-x)Na_{0.5}Bi_{0.5}TiO_3$-$xNa_{0.5}K_{0.5}NbO_3$ ceramics. *J Adv Dielectr* 2024, **14:** 2350023.

[187] McQuade R R, Dolgos M R A review of the structure-property relationships in lead-free piezoelectric $(1-x)Na_{0.5}Bi_{0.5}TiO_3$–$(x)BaTiO_3$. *J. Solid State Chem.* 2016, **242:** 140-147.

[188] Zheng T, Wu J, Xiao D, et al. Recent development in lead-free perovskite piezoelectric bulk materials. *Prog Mater Sci* 2018, **98:** 552-624.

[189] Zhang H, Ramadan A H H, De Souza R A Atomistic simulations of ion migration in sodium bismuth titanate (NBT) materials: towards superior oxide-ion conductors. *J Mater Chem A* 2018, **6:** 9116-9123.

[190] Wang D, Ke X Q, Wang Y Z, et al. Phase diagram of polar states in doped ferroelectric systems. *Physical Review B* 2012, **86:** 7.

[191] He S, Lou K, Han B, et al. Superior energy storage density and efficiency in antiferroelectric-like BNT-based ceramics via single-element phase engineering. *J Adv Ceram* 2025, **14:** 9221056.

[192] Zheng Q, Xie B, Wang Q, et al. Remarkable energy storage properties in $(Bi_{0.5}Na_{0.5})TiO_3$-based quasilinear relaxor ferroelectrics via superparaelectric regulation. *Chem Eng J* 2024, **483:** 149154.

[193] Zhang S-T, Kounga A B, Jo W, et al. High-Strain Lead-free Antiferroelectric Electrostrictors. *Adv Mater* 2009, **21:** 4716-4720.

[194] Sakata K, Masuda Y Ferroelectric and antiferroelectric properties of $(Na_{0.5}Bi_{0.5})TiO_3$-$SrTiO_3$ solid solution ceramics. *Ferroelectrics* 1974, **7:** 347-349.

[195] Qiao X, Zhang F, Wu D, et al. Superior comprehensive energy storage properties in Bi0.5Na0.5TiO3-based relaxor ferroelectric ceramics. *Chem Eng J* 2020, **388:** 124158.

[196] Trolliard G, Dorcet V Reinvestigation of phase transitions in $Na_{0.5}Bi_{0.5}TiO_3$ by TEM: Part II: Second order orthorhombic to tetragonal phase transition. *Chem. Mater.* 2008, **20:** 5074-5082.

[197] Dorcet V, Trolliard G, Boullay P The structural origin of the antiferroelectric properties and relaxor behavior of $Na_{0.5}Bi_{0.5}TiO_3$. *Journal of Magnetism and Magnetic Materials* 2009, **321:** 1758-1761.

[198] Suchanicz J, Kwapulinski J X-ray diffraction study of the phase transitions in

Na0.5Bi0.5TiO3. *Ferroelectrics* 1995, **165:** 249-253.

[199] Vakhrushev S B, Isupov V A, Kvyatkovsky B E, et al. Phase transitions and soft modes in sodium bismuth titanate. *Ferroelectrics* 1985, **63:** 153-160.

[200] Schmitt L A, Kleebe H-J Single grains hosting two space groups — a transmission electron microscopy study of a lead-free ferroelectric. *Funct. Mater Lett* 2010, **03:** 55-58.

[201] Daniels J E, Jo W, Rödel J, et al. Electric-field-induced phase-change behavior in $(Bi_{0.5}Na_{0.5})TiO_3$–$BaTiO_3$–$(K_{0.5}Na_{0.5})NbO_3$: A combinatorial investigation. *Acta Mater* 2010, **58:** 2103-2111.

[202] Li F, Liu Y, Lyu Y, et al. Huge strain and energy storage density of A-site La^{3+} donor doped $(Bi_{0.5}Na_{0.5})_{0.94}Ba_{0.06}TiO_3$ ceramics. *Ceram Int* 2017, **43:** 106-110.

[203] Liu X, Guo H, Tan X Evolution of structure and electrical properties with lanthanum content in $[(Bi_{1/2}Na_{1/2})_{0.95}Ba_{0.05}]_{1-x}La_xTiO_3$ ceramics. *J Eur Ceram Soc* 2014, **34:** 2997-3006.

[204] Wang M, Bai T, He A, et al. Excellent thermal stability and high energy storage performances of BNT-based ceramics via phase-structure engineering. *J Materiomics* 2023, **9:** 1015-1023.

[205] Cross L E Relaxor ferroelectrics. *Ferroelectrics* 1987, **76:** 241-267.

[206] Jin L, Li F, Zhang S Decoding the Fingerprint of Ferroelectric Loops: Comprehension of the Material Properties and Structures. *J Am Ceram Soc* 2014, **97:** 1-27.

[207] Beuerlein M A, Kumar N, Usher T-M, et al. Current Understanding of Structure–Processing–Property Relationships in $BaTiO_3$–$Bi(M)O_3$ Dielectrics. *J Am Ceram Soc* 2016, **99:** 2849-2870.

[208] Ortega N, Kumar A, Scott J F, et al. Relaxor-ferroelectric superlattices: high energy density capacitors. *J Phys: Condens Matter* 2012, **24:** 445901.

[209] Nicole A B, Craig J F Why are there so few perovskite ferroelectrics? *The Journal of Physical Chemistry C* 2013,

[210] Kai-Christian M, Leonie K, Karsten A Phase transformations in the relaxor $Na_{1/2}Bi_{1/2}TiO_3$ studied by means of density functional theory calculations. *J Am*

Ceram Soc 2017,

[211] Zheng S, Li Q, Chen Y, et al. Enhanced energy storage density with excellent temperature-stable dielectric properties of (1-*x*)[($Bi_{0.5}Na_{0.5}$)$_{0.94}Ba_{0.06}TiO_3$]-*x*$AgNbO_3$ lead-free ceramics. *J Alloys Compd* 2022, **911:** 165019.

[212] Rao B N, Datta R, Chandrashekaran S S, et al. Local structural disorder and its influence on the average global structure and polar properties in $Na_{0.5}Bi_{0.5}TiO_3$. *Physical Review B* 2013, **88:** 15.

[213] Otonicar M, Park J, Logar M, et al. External-field-induced crystal structure and domain texture in (1−*x*)$Na_{0.5}Bi_{0.5}TiO_3$–*x*$K_{0.5}Bi_{0.5}TiO_3$ piezoceramics. *Acta Mater* 2017, **127:** 319-331.

[214] Patrick F, Marc K, Attilio F Phase-field modeling of domain evolution in ferroelectric materials in the presence of defects. *Smart Mater. Struct.* 2019,

[215] Yang Y, Liu Z, Ren P, et al. Modulation of phase boundary and domain structures to engineer strain properties in BNT-based ferroelectrics. *J Adv Ceram* 2024, **13:** 967-975.

[216] Li Z, Li D-X, Shen Z-Y, et al. Remarkably enhanced dielectric stability and energy storage properties in BNT—BST relaxor ceramics by A-site defect engineering for pulsed power applications. *J Adv Ceram* 2022, **11:** 283-294.

[217] Luo C, Feng Q, Luo N, et al. Effect of Ca^{2+}/Hf^{4+} modification at A/B sites on energy-storage density of $Bi_{0.47}Na_{0.47}Ba_{0.06}TiO_3$ ceramics. *Chem Eng J* 2021, **420:** 129861.

[218] Hiruma Y, Nagata H, Takenaka T Phase diagrams and electrical properties of ($Bi_{1/2}Na_{1/2}$)TiO_3-based solid solutions. *J. Appl. Phys.* 2008, **104:** 124106.

[219] Yang S M, Jo J Y, Kim T H, et al. ac dynamics of ferroelectric domains from an investigation of the frequency dependence of hysteresis loops. *Physical Review B* 2010, **82:** 174125.

[220] Rao B N, Datta R, Chandrashekaran S S, et al. Local structural disorder and its influence on the average global structure and polar properties in $Na_{0.5}Bi_{0.5}TiO_3$. *Physical Review B* 2013, **88:** 224103.

[221] Riemer L M, Lalitha K V, Jiang X, et al. Stress-induced phase transition in lead-

free relaxor ferroelectric composites. *Acta Mater* 2017, **136:** 271-280.

[222] Jiang S, Zhang J, Wang J, et al. Excellent energy storage properties in non-stoichiometric $Bi_{0.5}Na_{0.5}TiO_3$-based relaxor ferroelectric ceramics. *Chin. Chem. Lett.* 2024, **35:** 108955.

[223] Wu C, Qiu X, Chen L, et al. A strategy to achieve high energy storage performance under a relatively low electric field in NBT-based ceramics. *J Alloys Compd* 2022, **910:** 164851.

[224] Li Z, Wang Z, Yang Q, et al. Phase transition and energy storage properties of $Bi_{0.5}Na_{0.5}TiO_3$–$Bi(Mg_{2/3}Nb_{1/3})O_3$ lead-free ceramics. *Ceram Int* 2023, **49:** 9615-9621.

[225] Ma C, Tan X, Dul'kin E, et al. Domain structure-dielectric property relationship in lead-free $(1-x)(Bi_{1/2}Na_{1/2})TiO_3$-$xBaTiO_3$ ceramics. *J. Appl. Phys.* 2010, **108:** 104105.

[226] Yan F, Zhou X, He X, et al. Superior energy storage properties and excellent stability achieved in environment-friendly ferroelectrics via composition design strategy. *Nano Energ* 2020, **75:** 105012.

[227] Ma Z, Zhu J, Wu J, et al. Optimization of energy storage properties in $(1-x)Na_{0.5}Bi_{0.5}TiO_3$-$xSr_{0.7}La_{0.2}TiO_3$-relaxed ferroelectric ceramics. *J Adv Dielectr* 2023, **13:** 2242003.

[228] Kang R R, Wang Z P, Liu W Y, et al. Domain engineered lead-free ceramics with large energy storage density and ultra-high efficiency under low electric fields. *ACS Appl Mater Interfaces* 2021, **13:** 25143-25152.

[229] Kang R, Wang Z, Lou X, et al. Energy storage performance of $Bi_{0.5}Na_{0.5}TiO_3$-based relaxor ferroelectric ceramics with superior temperature stability under low electric fields. *Chem Eng J* 2021, **410:** 128376.

[230] Fan J, He G, Cao Z, et al. Ultrahigh energy-storage density of a lead-free $0.85B_{i0.5}Na_{0.5}TiO_3$–$0.15Ca(Nb_{0.5}Al_{0.5})O_3$ ceramic under low electric fields. *Inorg. Chem. Front.* 2023, **10:** 1561-1573.

[231] Gao P, Geng W, Liu C, et al. Design of BNT-based ceramics with enhanced energy density and ultrahigh polarization under moderate electric field via introducing

BMW. *Chem Eng J* 2025, **523:** 168818.

[232] Qi X, Zhou W, Tian S, et al. Optimizing the dielectric and energy storage properties of BNT-based lead-free ceramics via A-site defect engineering. *Ceram Int* 2025, **51:** 44612-44618.

[233] Yang J, Zhu X, Wang H, et al. Achieving outstanding energy storage behaviors via combinatorial optimization design in BNT-based relaxor ferroelectric ceramics under medium–low electric fields. *J Mater Chem C* 2024, **12:** 6479-6486.

[234] Chen L, Deng S, Liu H, et al. Giant energy-storage density with ultrahigh efficiency in lead-free relaxors via high-entropy design. *Nat Commun* 2022, **13:** 3089.

[235] Chen M, Zhan S, Yuan Q, et al. Enhanced energy storage performance of $Na_{0.5}Bi_{0.5}TiO_3$ lead–free ceramics under low electric field. *Mater. Today Energy* 2023, **31:** 101193.

[236] Li Q-N, Zhou C-R, Xu J-W, et al. Ergodic relaxor state with high energy storage performance induced by doping $Sr_{0.85}Bi_{0.1}TiO_3$ in $Bi_{0.5}Na_{0.5}TiO_3$ ceramics. *J. Electron. Mater.* 2016, **45:** 5146-5151.

[237] Chen Y, Wang Y, Zhao D, et al. Enhanced energy storage properties and dielectric stabilities in BNT-based ceramics via multiphase and dielectric peak broadening engineering. *Mater. Chem. Phys.* 2022, **290:** 126542.

[238] Wang T, Li Y, Zhang X, et al. Simultaneous excellent energy storage density and efficiency under applied low electric field for high entropy relaxor ferroelectric ceramics. *Mater. Res. Bull.* 2023, **157:** 112024.

[239] Pan Z, Hao H, Li D, et al. Sm doped BNT–BZT lead-free ceramic for energy storage applications with broad temperature range. *J Mater Sci: Mater Electron* 2022, **33:** 14644-14654.

[240] Liu J, Ding Y, Li C, et al. Relaxor ferroelectric $(Bi_{0.5}Na_{0.5})TiO_3$-based ceramic with remarkable comprehensive energy storage performance under low electric field for capacitor applications. *J Mater Sci: Mater Electron* 2021, **32:** 21164-21177.

[241] Wang J, Zhang F, Peng Z, et al. Sodium bismuth titanate-based perovskite

ceramics with high energy storage efficiency and discharge performance. *J Materiomics* 2022, **8:** 1077-1085.

[242] Wang X, Liu X, Xue H, et al. Temperature-independent large strain with small hysteresis in Sb-modified BNT-based lead-free ceramics. *J Am Ceram Soc* 2022, **105:** 2116-2127.

[243] Nie X, Wang J, Peng Z, et al. High transparency and good electric properties in low symmetry BNT-based ceramics. *Solid State Sci.* 2022, **129:** 106906.

[244] Deng A, Wu J Optimized strain properties with small hysteresis in BNT-based ceramics with ergodic relaxor state. *J Eur Ceram Soc* 2021, **41:** 5147-5154.

[245] Deng A, Wu J Enhanced strain and electrostrictive properties in lead-free BNT-based ceramics via rare earth doping. *J Materiomics* 2022, **8:** 401-407.

[246] Lin H, Xu W, Zhang H, et al. Origin of high dielectric performance in fine grain-sized CaCu3Ti4O12 materials. *Journal of the European Ceramic Society* 2020, **40:** 1957-1966.

[247] Zhang L, Pu Y, Chen M, et al. High energy-storage density under low electric fields and improved optical transparency in novel sodium bismuth titanate-based lead-free ceramics. *J Eur Ceram Soc* 2020, **40:** 71-77.

[248] Wang Y, Lv Z, Xie H, et al. High energy-storage properties of $[(Bi_{1/2}Na_{1/2})_{0.94}Ba_{0.06}]La_{(1-x)}Zr_xTiO_3$ lead-free anti-ferroelectric ceramics. *Ceram Int* 2014, **40:** 4323-4326.

[249] Yan B, Fan H, Yadav A K, et al. $[(Bi_{0.5}0Na_{0.4}0K_{0.10})_{0.94}Ba_{0.06}]_{1-x}La_xTi_{0.975}Ta_{0.025}O_3$ lead-free relaxor ceramics with high energy storage density and thermally stable dielectric properties. *J. Mater. Sci.* 2020, **55:** 14728-14739.

[250] Cao W P, Li W L, Dai X F, et al. Large electrocaloric response and high energy-storage properties over a broad temperature range in lead-free NBT-ST ceramics. *J Eur Ceram Soc* 2016, **36:** 593-600.

[251] Wang C, Lou X, Xia T, et al. The dielectric, strain and energy storage density of BNT-BKH_xT_{1-x} piezoelectric ceramics. *Ceram Int* 2017, **43:** 9253-9258.

[252] Hao J, Xu Z, Chu R, et al. Enhanced energy-storage properties of $(1-x)[(1-y)(Bi_{0.5}Na_{0.5})TiO_3–y(Bi_{0.5}K_{0.5})TiO_3]–x(K_{0.5}Na_{0.5})NbO_3$ lead-free

ceramics. *Solid State Commun.* 2015, **204:** 19-22.

[253] Zhang L, Pu X, Chen M, et al. Influence of BaSnO3 additive on the energy storage properties of Na0.5Bi0.5TiO3-based relaxor ferroelectrics. *J Eur Ceram Soc* 2018, **38:** 2304-2311.

[254] Yu Y, Zhang Y, Zhang Y, et al. High-temperature energy storage performances in (1-x)($Na_{0.50}Bi_{0.50}TiO_3$)-x$BaZrO_3$ lead-free relaxor ceramics. *Ceram Int* 2020, **46:** 28652-28658.

[255] Ma W, Zhu Y, Marwat M A, et al. Enhanced energy-storage performance with excellent stability under low electric fields in BNT–ST relaxor ferroelectric ceramics. *J Mater Chem C* 2019, **7:** 281-288.

[256] Wang H, Jiang X, Liu X, et al. An effective approach to achieve high energy storage density and efficiency in BNT-based ceramics by doping $AgNbO_3$. *Dalton Trans.* 2019, **48:** 17864-17873.

[257] Jiang Z, Yang Z, Yuan Y, et al. High energy storage properties and dielectric temperature stability of (1-x)(0.8$Bi_{0.5}Na_{0.5}TiO_3$-0.2$Ba_{0.3}Sr_{0.7}TiO_3$)-x$NaNbO_3$ lead-free ceramics. *J Alloys Compd* 2021, **851:** 156821.

[258] Yang F, Pan Z, Ling Z, et al. Realizing high comprehensive energy storage performances of BNT-based ceramics for application in pulse power capacitors. *J Eur Ceram Soc* 2021, **41:** 2548-2558.

[259] Shi J, Zhao Y, He J, et al. Deferred polarization saturation boosting superior energy-storage efficiency and density simultaneously under moderate electric field in relaxor ferroelectrics. *ACS Appl Energy Mater* 2022, **5:** 3436-3446.

[260] Li X, Yang H, Zhu C, et al. Enhanced high-temperature energy storage properties in BNT-based ceramics with well-controlled low dielectric loss. *Ceram Int* 2024, **50:** 1438-1442.

[261] Wang Q, Xie B, Zheng Q, et al. $Bi_{0.5}Na_{0.5}TiO_3$-based relaxor-ferroelectric ceramics for low-electric-field dielectric energy storage via bidirectional optimization strategy. *Chem Eng J* 2023, **452:** 139422.

[262] Mao P, Guo Y, Lu G, et al. Synergistic effect of multi-phase and multi-domain structures induced high energy storage performances under low electric fields in

$Na_{0.5}Bi_{0.5}TiO_3$-based lead-free ceramics. *Chem Eng J* 2023, **472:** 144973.

[263] Yao M, Pu Y, Zhang L, et al. Enhanced energy storage properties of $(1-x)Bi_{0.5}Na_{0.5}TiO_3$-$xBa_{0.85}Ca_{0.15}Ti_{0.9}Zr_{0.1}O_3$ ceramics. *Mater Lett* 2016, **174:** 110-113.

[264] Zhou X, Liu K, Yan Z, et al. High energy storage efficiency of NBT-SBT lead-free ferroelectric ceramics. *Ceram Int* 2022, **48:** 23266-23272.

[265] Li D, Shen Z-Y, Li Z, et al. P–E hysteresis loop going slim in Ba0.3Sr0.7TiO3-modified Bi0.5Na0.5TiO3 ceramics for energy storage applications. *J Adv Ceram* 2020, **9:** 183-192.

[266] Li D-X, Deng W, Shen Z-Y, et al. Aliovalent Sm-doping enables BNT-based realxor ferroelectric ceramics with > 90% energy efficiency. *J Adv Ceram* 2024, **13:** 2043-2050.

[267] Zhang Z, Zhang F, Niu Y, et al. High energy storage performance in $(Ag_{0.94}La_{0.02})(Nb_{0.85}Ta_{0.15})O_3$-modified BNT-based ceramics at lower electric field. *J Am Ceram Soc* 2025, **n/a:** e20651.

[268] Han K, Luo N, Chen Z, et al. Simultaneously optimizing both energy storage density and efficiency in a novel lead-free relaxor antiferroelectrics. *J Eur Ceram Soc* 2020, **40:** 3562-3568.

[269] Qiao X, Wu D, Zhang F, et al. $Bi_{0.5}Na_{0.5}TiO_3$-based relaxor ferroelectric ceramic with large energy density and high efficiency under a moderate electric field. *J Mater Chem C* 2019, **7:** 10514-10520.

[270] Pan Z, Hu D, Zhang Y, et al. Achieving high discharge energy density and efficiency with NBT-based ceramics for application in capacitors. *J Mater Chem C* 2019, **7:** 4072-4078.

[271] Wang M, Feng Q, Wei Y, et al. Relaxor ferroelectric $Bi_{0.5}Na_{0.5}TiO_3$–$Sr_{0.7}Nd_{0.2}TiO_3$ ceramics with high energy storage density and excellent stability under a low electric field. *J. Phys. Chem. Solids* 2021, **157:** 110209.

[272] Zhang L, Pu Y, Chen M, et al. Novel $Na_{0.5}Bi_{0.5}TiO_3$ based, lead-free energy storage ceramics with high power and energy density and excellent high-temperature stability. *Chem Eng J* 2020, **383:** 123154.

[273] Zhang L, Pu Y, Chen M Ultra-high energy storage performance under low electric fields in $Na_{0.5}Bi_{0.5}TiO_3$-based relaxor ferroelectrics for pulse capacitor applications. *Ceram Int* 2020, **46:** 98-105.

[274] Wu Y, Fan Y, Liu N, et al. Enhanced energy storage properties in sodium bismuth titanate-based ceramics for dielectric capacitor applications. *J Mater Chem C* 2019, **7:** 6222-6230.

[275] Lu Y, Wang X, Li P, et al. The grain size and domain structure synergistic effect on BNT based lead-free ceramics with high energy storage properties. *J. Energy Storage* 2024, **104:**

[276] Shi P, Zhu X, Lou X, et al. Tailoring ferroelectric polarization and relaxation of BNT-based lead-free relaxors for superior energy storage properties. *Chem Eng J* 2022, **428:** 132612.

[277] Ma W, Fan P, Salamon D, et al. Fine-grained BNT-based lead-free composite ceramics with high energy-storage density. *Ceram Int* 2019, **45:** 19895-19901.

[278] Zhu C Q, Cai Z M, Luo B C, et al. Multiphase engineered BNT-based ceramics with simultaneous high polarization and superior breakdown strength for energy storage applications. *ACS Appl Mater Interfaces* 2021, **13:** 28484-28492.

[279] Yuan Q, Zhan S, Li Y, et al. Toward high-end lead-free ceramics for energy storage: $Na_{0.5}Bi_{0.5}TiO_3$-based relaxor ferroelectrics with simultaneously enhanced energy density and efficiency. *Mater. Today Energy* 2023, **31:** 101202.

[280] Bin C, Hou X, Liao L, et al. Improved energy storage performance in rare-earth modified lead-free BNT-based relaxor ferroelectric ceramics. *Appl Phys Lett* 2023, **123:** 012901.

[281] Zhou X F, Qi H, Yan Z N, et al. Superior thermal stability of high energy density and Power Density in Domain-Engineered $Bi_{0.5}Na_{0.5}TiO_3$-$NaTaO_3$ Relaxor Ferroelectrics. *ACS Appl Mater Interfaces* 2019, **11:** 43107-43115.

[282] Li D, Lin Y, Zhang M, et al. Achieved ultrahigh energy storage properties and outstanding charge–discharge performances in $(Na_{0.5}Bi_{0.5})_{0.7}Sr_{0.3}TiO_3$-based ceramics by introducing a linear additive. *Chem Eng J* 2020, **392:** 123729.

[283] Zhou S Y, Pu Y P, Zhao X Y, et al. Dielectric temperature stability and energy

storage performance of NBT-based ceramics by introducing high-entropy oxide. *J Am Ceram Soc* 2022, **105:** 4796-4804.

[284] Su Y, Zhou X, Xue G, et al. Temperature-stable $Na_{0.5}Bi_{0.5}TiO_3$-based ceramics with favorable low-temperature dielectric and energy storage property. *J Am Ceram Soc* 2023, **106:** 3525-3536.

[285] Han D, Zhang B, Zhao D, et al. Superior energy storage properties of (1-x)$Ba_{0.85}Ca_{0.15}Zr_{0.1}Ti_{0.9}O_3$-x$Bi(Mg_{2/3}Ta_{1/3})O_3$ lead-free ceramics. *J Alloys Compd* 2023, **946:** 169300.

[286] Han D, Wang C, Zeng Z, et al. Ultrahigh energy efficiency of (1-x)$Ba_{0.85}Ca_{0.15}Zr_{0.1}Ti_{0.9}O_3$-x$Bi(Mg_{0.5}Sn_{0.5})O_3$ lead-free ceramics. *J Alloys Compd* 2022, **902:** 163721.

[287] Deng T, Hu T, Liu Z, et al. Ultrahigh energy storage performance in BNT-based binary ceramic via relaxor design and grain engineering. *Energy Storage Mater* 2024, **71:** 103659.

[288] Cai Z, Zhu C, Wang H, et al. High-temperature lead-free multilayer ceramic capacitors with ultrahigh energy density and efficiency fabricated via two-step sintering. *J Mater Chem A* 2019, **7:** 14575-14582.

[289] Zhang X, Hu D, Pan Z, et al. Enhancement of recoverable energy density and efficiency of lead-free relaxor-ferroelectric BNT-based ceramics. *Chem Eng J* 2021, **406:** 126818.

[290] Chen C, Liang R, Zhou Z, et al. Enhanced bipolar fatigue resistance in PMN-PZT ceramics prepared by spark plasma sintering. *Ceram Int* 2018, **44:** 3563-3570.

[291] Kumar N, Ansell T Y, Cann D P Role of point defects in bipolar fatigue behavior of $Bi(Mg_{1/2}Ti_{1/2})O_3$ modified $(Bi_{1/2}K_{1/2})TiO_3$-$(Bi_{1/2}Na_{1/2})TiO_3$ relaxor ceramics. *J. Appl. Phys.* 2014, **115:** 154104.

[292] Yao Z H, Song Z, Hao H, et al. Homogeneous/Inhomogeneous-structured dielectrics and their energy-storage performances. *Adv Mater* 2017, **29:** 15.

[293] Yang S, Zeng D, Dong Q, et al. Enhancement of energy storage performances in $BaTiO_3$-based ceramics via introducing $Bi(Mg_{2/3}Sb_{1/3})O_3$. *J. Energy Storage* 2024, **78:** 110102.

[294] Ning Y, Pu Y, Zhang X, et al. Remarkable energy-storage density together with efficiency of above 92% in high-entropy ferroelectric ceramics. *Mater Today Phys* 2024, **43:** 101418.

[295] Chen P, Zhang L, Wang Z, et al. Improved dielectric energy storage performance of Pb-free $0.5Na_{0.5}Bi_{0.5}TiO_3$-$0.5SrTiO_3$ ceramics modified with CaO. *J Adv Dielectr* 2018, **08:** 1850042.

[296] Zhang L, Pu Y, Chen M, et al. Antiferroelectric-like properties in MgO-modified $0.775Na_{0.5}Bi_{0.5}TiO_3$-$0.225BaSnO_3$ ceramics for high power energy storage. *J Eur Ceram Soc* 2018, **38:** 5388-5395.

[297] Huang N, Liu H, Hao H, et al. Energy storage properties of MgO-doped $0.5Bi_{0.5}Na_{0.5}TiO_3$-$0.5SrTiO_3$ ceramics. *Ceram Int* 2019, **45:** 14921-14927.

[298] Li F, Zhai J W, Shen B, et al. Simultaneously high-energy storage density and responsivity in quasi-hysteresis-free Mn-doped $Bi_{0.5}Na_{0.5}TiO_3$-$BaTiO_3$-$(Sr_{0.7}Bi_{0.2}\square_{0.1})TiO_3$ ergodic relaxor ceramics. *Mater. Res. Lett.* 2018, **6:** 345-352.

[299] Thatje S Naturwissenschaften: recent advances, changes and challenges. *Naturwissenschaften* 2012, **99:** 1-2.

[300] Zhao L, Gao J, Liu Q, et al. Silver niobate lead-free antiferroelectric ceramics: enhancing energy storage density by B-Site doping. *ACS Appl Mater Interfaces* 2018, **10:** 819-826.

[301] Shi R, Pu Y, Wang W, et al. A novel lead-free $NaNbO_3$–$Bi(Zn_{0.5}Ti_{0.5})O_3$ ceramics system for energy storage application with excellent stability. *J Alloys Compd* 2020, **815:** 152356.

[302] Nie H, Jiao Y, Jin D, et al. Improved dielectric energy storage performance of $Na_{0.5}Bi_{0.5}TiO_3$–$Sr_{0.7}Nd_{0.2}TiO_3$ lead-free ceramics by adding an appropriate amount of $AgNbO_3$. *Ceram Int* 2022, **48:** 31223-31232.

[303] Jiang Y, Zhu C, Zhao P, et al. Excellent energy storage performance of $NaNbO_3$-based antiferroelectric ceramics with ultrafast charge/discharge rate. *J Eur Ceram Soc* 2021, **41:** 6465-6473.

[304] Cao W, Li L, Zhao H, et al. Outstanding energy storage performance of NBT-Based ceramics under moderate electric field achieved via antiferroelectric

engineering. *ACS Appl Mater Interfaces* 2023, **15:** 38633-38643.

[305] Shang K, Shi W, Yang Y, et al. Medium electric field-induced ultrahigh polarization response and boosted energy-storage characteristics in BNT-based relaxor ferroelectric polycrystalline ceramics. *Ceram Int* 2022, **48:** 37223-37231.

[306] Shi L N, Wang Y G, Ren Z H, et al. Significant improvement in electrical characteristics and energy storage performance of NBT-based ceramics. *Ceram Int* 2022, **48:** 26973-26983.

[307] Shi P, Zhu X, Lou X, et al. $Bi_{0.5}Na_{0.5}TiO_3$-based lead-free ceramics with superior energy storage properties at high temperatures. *Compos Part B Eng* 2021, **215:** 108815.

[308] Zhou Q, Peng Z, Zhang F, et al. Achieving high comprehensive energy storage properties of BNT-based ceramics via multiscale regulation. *Ceram Int* 2023, **49:** 19701-19707.

[309] Lai F, Wang J, Chen M, et al. Improving the electric energy storage performance of BNT-based relaxor ferroelectric ceramics with tunable oxygen vacancies and refined grains through $Sr_{1/2}Nd_{1/3}(Mg_{1/3}Nb_{2/3})O_3$ dopant. *Chem Eng J* 2025, **520:** 165549.

[310] Long C, Su Z, Xu A, et al. High energy storage performance in the $Bi_{0.5}Na_{0.5}TiO_3$–$BaTiO_3$–$Nd(Mg_{1/2}Hf_{1/2})O_3$ ternary system with multiscale polymorphic domains and local heterogeneous structure. *J Adv Ceram* 2025, **14:** 9221063.

[311] Zhang X, Zhao L, Liu L, et al. Interface and defect modulation via a core–shell design in $(Na_{0.5}Bi_{0.5}TiO_3@La_2O_3)$-$(SrSn_{0.2}Ti_{0.8}O_3@La_2O_3)$-$Bi_2O_3$-$B_2O_3$-$SiO_2$ composite ceramics for wide-temperature energy storage capacitors. *Chem Eng J* 2022, **435:** 135061.

[312] Zhang Z X, Tan R H, Wang F F, et al. Core-Shell grain structure and high energy storage performance of BNT-Based relaxor ferroelectric ceramics. *Electron Mater Lett* 2023, **19:** 161-171.

[313] Xue G L, Zhou X F, Su Y C, et al. Core-shell structure and domain engineering in $Bi_{0.5}Na_{0.5}TiO_3$-based ceramics with enhanced dielectric and energy storage performance. *J Materiomics* 2023, **9:** 855-866.

[314] Huang J, Qi H, Gao Y, et al. Expanded linear polarization response and excellent energy-storage properties in $(Bi_{0.5}Na_{0.5})TiO_3$-$KNbO_3$ relaxor antiferroelectrics with medium permittivity. *Chem Eng J* 2020, **398:** 125639.

[315] Wang Z, Zhang L, Kang R, et al. $(Bi_{0.5}Na_{0.5})TiO_3$-based relaxor ferroelectrics with enhanced energy-storage density and efficiency under low/moderate - fields via average ionic polarizability design. *Chem Eng J* 2022, **431:** 133716.

[316] Ning Y, Pu Y, Zhang Q, et al. Achieving high energy storage properties in perovskite oxide via high-entropy design. *Ceram Int* 2023, **49:** 12214-12223.

[317] Shi P, Li T Y, Lou X J, et al. Large electric-field-induced strain and energy storage properties in $Bi_{0.5}Na_{0.5}TiO_3$-$(0.5Ba_{0.7}Ca_{0.3}TiO_3$-$0.5BaTi_{0.8}Zr_{0.2}O_3$) lead-free relaxor ferroelectric ceramics. *J Alloys Compd* 2021, **860:** 10.

[318] Wu L K, Tang L M, Zhai Y Z, et al. Enhanced energy-storage performance in BNT-based lead-free dielectric ceramics via introducing $SrTi_{0.875}Nb_{0.1}O_3$. *J Materiomics* 2022, **8:** 537-544.

[319] Huang Y N, Zhang J, Wang J J, et al. Ultrahigh energy storage density, high efficiency and superior thermal stability in $Bi_{0.5}Na_{0.5}TiO_3$-based relaxor ferroelectric ceramics via constructing multiphase structures. *J Mater Chem A* 2023, **11:** 7987-7994.

[320] Guo B, Yan Y, Tang M Y, et al. Energy storage performance of $Na_{0.5}Bi_{0.5}TiO_3$ based lead-free ferroelectric ceramics prepared via non-uniform phase structure modification and rolling process. *Chem Eng J* 2021, **420:** 12.

[321] Chu B K, Hao J G, Li P, et al. High-energy storage properties over a broad temperature range in La-modified BNT-based lead-free ceramics. *ACS Appl Mater Interfaces* 2022, **14:** 19683-19696.

[322] Chai Q Z, Zhang F D, Zhou Q Y, et al. Superior energy storage properties and optical transparency in $K_{0.5}Na_{0.5}NbO_3$-based dielectric ceramics via multiple synergistic strategies. *Small* 2023, **19:** 7.

[323] Zhou C, Yan F, Zheng Z, et al. Achieving superior capacitive energy storage in tape-casting fabricated $Bi_{0.5}Na_{0.5}TiO_3$-based relaxor ferroelectrics via multiscale regulation. *Energy Storage Mater* 2025, **75:** 104082.

[324] Zhu X, Gao Y, Shi P, et al. Ultrahigh energy storage density in $(Bi_{0.5}Na_{0.5})_{0.65}Sr_{0.35}TiO_3$-based lead-free relaxor ceramics with excellent temperature stability. *Nano Energ* 2022, **98:** 107276.

[325] Li H, Yang F, Chen X, et al. Temperature stability and energy storage performances of $Bi(Li_{1/3}Hf_{2/3})O_3$-added BNT-based ceramics. *Ceram Int* 2023, **49:** 39559-39567.

[326] Deng T, Liu Z, Hu T F, et al. Excellent energy-storage performance in $Bi_{0.5}Na_{0.5}TiO_3$-based lead-free composite ceramics via introducing pyrochlore phase $Sm_2Ti_2O_7$. *Chem Eng J* 2023, **465:** 9.

[327] Wang H, Li Z M, Zhang J J, et al. Tailoring relaxor P4bm+P21ma phases in BNT-based ceramics for enhancing comprehensive energy storage properties. *J. Phys. Chem. Solids* 2023, **177:** 7.

[328] Li Z, Wang H, Zhang J, et al. Stabilizing polar P21ma phase in $Bi_{0.5}Na_{0.5}TiO_3$-$Na_{0.91}Bi_{0.09}Nb_{0.94}Mg_{0.06}O_3$ relaxors by $CaTiO_3$ additive to promote energy storage density, efficiency and discharge rate. *J Alloys Compd* 2023, **945:** 169273.

[329] Qi H, Zuo R Linear-like lead-free relaxor antiferroelectric $(Bi_{0.5}Na_{0.5})TiO_3$–$NaNbO_3$ with giant energy-storage density/efficiency and super stability against temperature and frequency. *J Mater Chem A* 2019, **7:** 3971-3978.

[330] Ma C, Tan X In situ transmission electron microscopy study on the phase transitions in lead-free $(1-x)(Bi_{1/2}Na_{1/2})TiO_3$-$xBaTiO_3$ ceramics. *J Am Ceram Soc* 2011, **94:** 4040-4044.

[331] Li D, Zhou D, Wang D, et al. Lead-free relaxor ferroelectric ceramics with ultrahigh energy storage densities via polymorphic polar nanoregions design. *Small* 2023, **19:** 9.

[332] Liu H, Sun Z, Zhang J, et al. Chemical Design of Pb-Free Relaxors for Giant Capacitive Energy Storage. *Journal of the American Chemical Society* 2023, **145:** 11764-11772.

[333] Zhao W C, Xu D M, Li D, et al. Broad-high operating temperature range and enhanced energy storage performances in lead-free ferroelectrics. *Nat Commun* 2023, **14:** 11.

[334] Yan F, Huang K, Jiang T, et al. Significantly enhanced energy storage density and efficiency of BNT-based perovskite ceramics via A-site defect engineering. *Energy Storage Mater* 2020, **30:** 392-400.

[335] Huang J, Deng L, Zhang Y, et al. Synergistically enhanced energy storage performance of Bi0.47Na0.47Ba0.06TiO3-based relaxor ferroelectrics via dual engineering of dynamic nanodomains and defect regulation. *J Mater Chem A* 2025, **13:** 30053-30064.

[336] Yuan Q B, Cui J, Wang Y F, et al. Significant enhancement in breakdown strength and energy density of the $BaTiO_3$/$BaTiO_3$@SiO_2 layered ceramics with strong interface blocking effect. *J Eur Ceram Soc* 2017, **37:** 4645-4652.

[337] Sun Z X, Ma C R, Liu M, et al. Ultrahigh energy storage performance of lead-free oxide multilayer film capacitors via interface engineering. *Adv Mater* 2017, **29:** 6.

[338] Zheng L, Sun P, Zheng P, et al. Significantly tailored energy-storage performances in $Bi_{0.5}Na_{0.5}TiO_3$–$SrTiO_3$-based relaxor ferroelectric ceramics by introducing bismuth layer-structured relaxor $BaBi_2Nb_2O_9$ for capacitor application. *J Mater Chem C* 2021, **9:** 5234-5243.

[339] Yan F, Qian J, Lin J F, et al. Ultrahigh energy storage density and efficiency of lead-free dielectrics with sandwich structure. *Small* 2024, **20:** 7.

[340] Feng H P, Tang L, Zeng G M, et al. Core-shell nanomaterials: Applications in energy storage and conversion. *Adv. Colloid Interface Sci.* 2019, **267:** 26-46.

[341] Yan F, Bai H, Zhou X, et al. Realizing superior energy storage properties in lead-free ceramics via a macro-structure design strategy. *J Mater Chem A* 2020, **8:** 11656-11664.

[342] Zhang R-Z, Reece M J Review of high entropy ceramics: design, synthesis, structure and properties. *J Mater Chem A* 2019, **7:** 22148-22162.

[343] Zhang J, Lin Y, Wang L, et al. Significantly enhanced energy storage density in sodium bismuth titanate-based ferroelectrics under low electric fields. *J Eur Ceram Soc* 2020, **40:** 5458-5465.

[344] Chen M, Pu Y, Zhang L, et al. Reducing applied field in NBT-based high energy-

storage ceramics via B-site entropy regulation. *Chem Eng J* 2023, **474:** 145386.

[345] Pu Y, Zhang Q, Li R, et al. Dielectric properties and electrocaloric effect of high-entropy $(Na_{0.2}Bi_{0.2}Ba_{0.2}Sr_{0.2}Ca_{0.2})TiO_3$ ceramic. *Appl Phys Lett* 2019, **115:** 223901.

[346] Yang W, Zheng G High energy storage density and efficiency in nanostructured $(Bi_{0.2}Na_{0.2}K_{0.2}La_{0.2}Sr_{0.2})TiO_3$ high-entropy ceramics. *J Am Ceram Soc* 2022, **105:** 1083-1094.

[347] Ren B, Liu Y-F, Meng Z-q, et al. Preparation and Electrical Properties Study of Non-equimolar Sr(Ti,Zr,Y,Sn,Hf)O3-σ High-entropy Perovskite Oxide. *Adv Ceram* 2023, **44:** 497-508.

[348] Li D, Zheng Z, Yang B, et al. Atomic-Scale High-Entropy Design for Superior Capacitive Energy Storage Performance in Lead-Free Ceramics. *Adv Mater* 2025, **37:** 2409639.

[349] Mao P, Guo Y, Wang T, et al. Boosting high electric breakdown strength for excellent energy storage performance in $Bi_{0.5}Na_{0.5}TiO_3$-based lead-free ceramics via a high entropy strategy. *ACS Appl Mater Interfaces* 2025, **17:** 1485-1498.

[350] Yang K, Luo G, Ma L, et al. Excellent energy storage performance in Bi0.5Na0.5TiO3-based lead-free high-entropy relaxor ferroelectrics via B-site modification. *J Adv Ceram* 2024, **13:** 345-353.

[351] Wang X, Zhang J, Ma X, et al. Machine learning assisted composition design of high-entropy Pb-free relaxors with giant energy-storage. *Nat Commun* 2025, **16:** 1254.

[352] Long C, Su Z, Song H, et al. Excellent energy storage properties with ultrahigh Wrec in lead-free relaxor ferroelectrics of ternary $Bi_{0.5}Na_{0.5}TiO_3$-$SrTiO_3$-$Bi_{0.5}Li_{0.5}TiO_3$ via multiple synergistic optimization. *Energy Storage Mater* 2024, **65:** 103055.

[353] Pang S, Fan X, Nie W, et al. Energy storage properties of superparaelectric phase in $0.6(0.8Bi_{0.5}Na_{0.5}TiO_3$-$0.2NaNbO_3)$-$0.4SrTiO_3$. *Chem Eng J* 2025, 169632.

[354] Long C, Su Z, Xu A, et al. $Bi_{0.5}Na_{0.5}TiO_3$-based energy storage ceramics with excellent comprehensive performance by constructing dynamic nanoscale domains and high intrinsic breakdown strength. *Nano Energ* 2024, **124:** 109493.

[355] Guo J, Yu H, Ren Y, et al. Multi-symmetry high-entropy relaxor ferroelectric with giant capacitive energy storage. *Nano Energ* 2023, **112:** 108458.

[356] Huang Y, Shang K, Yang Y, et al. Ultrahigh energy storage capacities in high-entropy relaxor ferroelectrics. *J Mater Chem A* 2024, **12:** 18224-18233.

[357] Cao M, Zhang X, Zhao S, et al. Achieving high energy storage performance in $(Bi_{0.5}Na_{0.5})_{0.7}Sr_{0.3}TiO_3$-based ceramics via synergistic optimization strategy. *J. Energy Storage* 2025, **135:** 118299.

[358] Zeng X, Lin J, Shen J, et al. Giant capacitive energy storage in high-entropy lead-free ceramics with temperature self-check. *Adv Mater* 2024, **36:** 2409059.

[359] Cao W, Wu Y, Yang X, et al. Breaking polarization-breakdown strength paradox for ultrahigh energy storage density in NBT-based ceramics. *Nat Commun* 2025, **16:** 6228.

[360] Huang J, Deng L, Zhang Y, et al. Realizing ultrahigh energy storage density in $(Bi_{0.5}Na_{0.5})_{0.94}Ba_{0.06}TiO_3$-based ceramics via manipulating the domain configuration and grain boundary density. *ACS Appl Mater Interfaces* 2024, **16:** 57334-57345.

[361] Huang Y, Zhang L, Jing R, et al. Dynamic Dipole Engineering Enables Ultrahigh Energy Storage with Minimal Losses. *Adv Mater* 2026, **38:** e22905.

[362] Wang S, Qian J, Ge G, et al. Embedding Plate-Like Pyrochlore in Perovskite Phase to Enhance Energy Storage Performance of BNT-Based Ceramic Capacitors. *Adv Energy Mater* 2025, **15:** 2403926.